YARBROUGH, RYAN, Ph.D. Metal Oxide Nanostructures for Thermoelectric Materials: Experimental and Computational Materials Performance Evaluation (2020) Directed by Dr. Hemali Rathnayake. 151 pp.

Waste recovery technologies, which convert heat into usable energy can meet the global demand for energy. One solution to this issue is thermoelectric generators (TEGs), which converts heat into electricity. However, several aspects of current TEGs need radical improvement before they can compete with incumbent technologies. The commercially available TEGs operate at a low efficiency, are made from expensive, toxic, and rare materials, and very are very expensive with a low Return on Investment. Metal oxides are an emerging set of materials that could perhaps overcome these drawbacks. The properties of metal oxides can further be tailored and fine-tuned by nanostructuring them, resulting in freezing phonon modes and reducing the materials thermal conductivity.

This dissertation research aims at investigating the thermoelectric properties (TE) of metal oxides nanostructures and compared their TE properties with TE properties of their bulk form powder materials, which define as having sizes above 100 nm in all dimensions. To do this, a new rapid designing and testing approach is developed by coupling a computational framework, which screens metal oxides with promising TE properties, with an experimental approach, which synthesize and evaluate TE properties of metal oxides nanostructuresand compared their thermoelectric properties with their counterparts of powder materials. Utilizing Density Functional Theory, (DFT) a computational approach is developed and can be used to rapidly predict the thermoelectric properties of most crystalline materials, enabling rapid screening of

potential metal oxides candidates. A sol-gel method is developed to make nanomaterials of metal oxides. The effects of the solvent type and base concentration on nanomaterials' morphologies and crystallinity are investigated by making five different metal oxides; Manganese Oxide, Magnesium Hydroxide, Copper Oxide, Chromium Oxide, and Strontium Oxide. Combining experimental and computational methods, a comprehensive analysis of the thermoelectric properties for Manganese Oxide (Mn_3O_4) nanoparticles and MnO_2 bulk powder is performed and compared with TE properties of its derivatives, Mn_3O_4, and MnO_2.

At the initial stages of evaluating the thermoelectric properties of manganese oxide, the pressed pellets of both Mn_3O_4 powder and its nanoparticle form were electrically insulating but showed a significantly high Seebeck coefficient in the range of 0.2 to 2 mV/K for the nanoparticles and 0.4 and 1.4 mV/K for the powder form, which is close to accepted values in literature. The TE properties of MnO_2 predicted using the computational framework developed in this work further confirmed its validity and shows potential of applying the method to TE materials screening for other inorganic oxides and dichalcogenide.

METAL OXIDE NANOSTRUCTURES FOR THERMOELECTRIC MATERIALS: EXPERIMENTAL AND COMPUTATIONAL MATERIALS PERFORMANCE EVALUATION

by

Ryan Yarbrough

A Dissertation Submitted to
the Faculty of The Graduate School at
The University of North Carolina at Greensboro
in Partial Fulfillment
of the Requirements for the Degree
Doctor of Philosophy

Greensboro
2020

Approved by

Hemali Rathnayake
Committee Chair

APPROVAL PAGE

This dissertation written by Ryan Yarbrough has been approved by the following committee of the Faculty of The Graduate School at The University of North Carolina at Greensboro.

Committee Chair Hemali Rathnayake

Committee Members Daniel Herr

Joseph Starobin

Kristen L Rhinehardt

_____3/25/2020_____
Date of Acceptance by Committee

_____3/11/2020_____
Date of Final Oral Examination

ACKNOWLEDGMENTS

I would like to thank my adviser Dr. Hemali Rathnayake for her guidance and unwavering support and my committee members: Drs. Daniel Herr, Joseph Starobin and Kristen Rhinehardt, for their guidance, support, and valuable input. I would like to thank The Joint School of Nanoscience and Nanoengineering (JSNN) and The Office of Research, University of North Carolina at Greensboro for financial support for this research. I would like to also thank current Dean Sherine Obare, and former Dean James Ryan for their guidance, providing the necessary facilities, as well as their continued support and funding. The support from the staff of the JSNN has been critical to accomplishing this work through advice, training and troubleshooting equipment; those I would like to thank are Drs. Kristen Dellinger, Kyle Nowlin, Kristen Rhinehardt, and Steven Crawford. I would like to also thank my fellow peers for all their assistance in all areas including experimental design, computational and data analysis; The entire Dr. Rathnayake group and Alex Sheardy.

TABLE OF CONTENTS

Page

LIST OF TABLES vii

LIST OF FIGURES viii

CHAPTER

I. INTRODUCTION 1

I.1 Introduction to Thermoelectrics and Thermoelectric Performance 1
I.2 General Goal of the Research 6

II. LITERATURE AND BACKGROUND 16

II.1 Metrics of Material and Device Characterization 16
II.2 State-of-the-Art for Materials 19
II.3 Improving Material Performance using Nanostructures 22

III. AIMS AND OBJECTIVES 25

III.1 Aim 1: Developing a Computational Method to Predict Thermoelectric Properties of Inorganic Materials 25
III.2 Aim 2: Developing a Sol-Gel Synthesis Method to make Metal Oxide Nanostructures and Investigating their Thermoelectric Properties 26
III.3 Aim 3: Understanding and Correlating the Computationally Predicted and Experimentally Evaluated Thermoelectric Properties of a Selected Metal Oxide 27

IV. APPROACH TO COMPUTATION 28

IV.1 Identification of Elements for Ideal Thermoelectric Materials 28
IV.2 Building a Computational Engine to Predict Thermoelectric Properties 30
IV.2.1 Computational Design Approach 35
IV.3 Theoretical Background for the Computational Engine 43
IV.3.1 Approach to Predict Electronic Properties 43
IV.4 Validation of Computational Prediction using Literature 48
IV.4.1 Method for Testing the Computational Engine Design 48

V. EXPERIMENTAL METHODS....52

V.1 Materials....52
V.2 Characterization....52
V.3 Procedures for Metal Oxides Nanomaterials Synthesis....53
V.3.1 Synthesis Procedure for Manganese Oxide Nanostructures....53
V.3.2 Synthesis Procedure for Magnesium Hydroxide Nanostructures....54
V.3.3 Synthesis Procedure for Copper Oxide Nanostructures....55
V.3.4 Synthesis Procedure for Chromium Oxide Nanostructures....56
V.3.5 Synthesis Procedure for Strontium Oxide Nanostructures....57
V.4 General Method for Sample Preparation for Characterization....58
V.5 Temperature Dependent Electrical and Thermoelectric Properties Characterization Method....59
V.5.1 Background of Strategy Development....59
V.5.2 Measurement Method Development and Mathematics....61
V.5.3 Electrical Conductivity....63
V.5.4 Seebeck Coefficient....66
V.5.5 Standard Material Measurement and Method Validation....73

VI. SOL-GEL SYNTHESIS OF METAL OXIDE NANOSTRUCTURES....78

VI.1 Metal Oxide Nanostructures and their Synthesis Methods....78
VI.2 Manganese Oxide....81
VI.3 Copper Oxide....91
VI.4 Magnesium Hydroxide....97
VI.5 Chromium Oxide....103
VI.6 Strontium Oxide....107

VII. COMPUTATIONAL AND EXPERIMENTAL ANALYSIS OF THERMOELECTRIC PROPERTIES OF MANGANESE OXIDE....113

VII.1 Background of Manganese Oxide as a Thermoelectric Material....113
VII.2 Full Manganese Oxide Nanoparticle Analysis for Thermoelectric Characterization....114
VII.3 Characterization of Manganese (II,III) Oxide Bulk Powder....121
VII.4 Computational Thermoelectric Properties for Mn_3O_4 Powder....124

VIII. CONCLUSION 130

REFERENCES 134

APPENDIX A. COMPUTATIONAL INPUT SCRIPTS FOR MANGANESE OXIDE 143

LIST OF TABLES

Page

Table 2.1. Cost and ZT of Current Thermoelectric Materials 20

Table 2.2. Power Production and Thermoelectric Power Generation Comparison.....21

Table 4.1. Elements with their Known Reserves and Production Rates.....29

Table 5.1. Precursor and Base Amounts used for the Preparation of Manganese Oxide Nanoparticles 54

Table 5.2. Precursor and Base Amounts used for the Preparation of Magnesium Hydroxide Nanoparticles 55

Table 5.3. Precursor and Base Amounts used for the Preparation of Copper Oxide Nanoparticles.....56

Table 5.4. Precursor and Base Amounts used for the Preparation of Chromium Oxide Nanoparticles 57

Table 5.5. Precursor and Base Amounts used for the Preparation of Strontium Oxide Nanoparticles.....58

Table 5.6. Thermoelectric Property Measurement Temperatures 63

Table 6.1. Manganese Oxide Nanoparticle Experimental Conditions and Morphologies.....83

Table 6.2. Copper Oxide Nanoparticle Experimental Conditions and Morphologies.....93

Table 6.3. Magnesium Hydroxide Nanoparticle Experimental Conditions and Morphologies 98

Table 6.4. Chromium Oxide Nanoparticle Experimental Conditions and Morphologies 103

Table 6.5. Strontium Oxide Nanostructures Experimental Conditions and Morphologies 108

LIST OF FIGURES

Page

Figure 1.1. The Reduction of Thermal Conductivity in Silicon using Nanowires and how the Arrangement of Atoms in that Matrix Changes the Conductivity 12

Figure 1.2. Tandem System of Nanowires for Thermoelectric Applications 13

Figure 2.1. A Schematic Diagram of a Typical TED Design 16

Figure 2.2. Cumulative Thermal Conductivity of Silicon 24

Figure 4.1. (Left) Face Center Cubic Unit Cell that uses Periodic Boundary Conditions for DFT Computations 31

Figure 4.2. Thermoelectric Property Prediction Computational Scheme 36

Figure 4.3. MnO_2 Band Structure in K-Space 40

Figure 4.4. Power Factor of MnO_2 with Respect to Chemical Potential and Temperature 42

Figure 4.5. PbTe Crystal Structure Rendered using VESTA 49

Figure 4.6. PbTe Figure of Merit with Respect to Chemical Potential and Temperature 50

Figure 4.7. PbTe Figure of Merit with Respect to Temperature 51

Figure 4.8. Literature PbTe Bulk Figure of Merit from the 1960s 51

Figure 5.1. A Schematic Diagram for the Temperature Dependent Thermoelectric Property Measurement System 61

Figure 5.2. An Image of the Thermoelectric Property Measurement Assembly 62

Figure 5.3. I-V Curve of Sample with Forward and Backward Bias Sweep 64

Figure 5.4. Voxel Rendering of Thermoelectric Measurement System for Thermal Diffusion Equation Simulation 68

Figure 5.5. Cross Section of Thermal Diffusion Simulation Running 69

Figure 5.6. Cross Section of Thermal Diffusion Simulation at Equilibrium 70

Figure 5.7. Linear Equilibrium Temperature Gradient across the Material and Steel Between the Heating Elements of the Testing Apparatus.....70

Figure 5.8. Simple Kirchhoff Loop Illustration 72

Figure 5.9. Thermal Potential Source from Thermoelectric Source in a Kirchhoff loop.....73

Figure 5.10. 9999 Pure Metal Mounted in Measurement System to Test Standard Materials 74

Figure 5.11. Electrical Conductivity of Molybdenum with Respect to Temperature.....75

Figure 5.12. Electrical Conductivity of Nickel with Respect to Temperature.....76

Figure 5.13. Seebeck Coefficient of Molybdenum with Respect to Temperature.....76

Figure 5.14. Seebeck Coefficient of Nickel with Respect to Temperature 77

Figure 6.1. Sol-Gel Metal Oxide Reaction Scheme.....81

Figure 6.2. SEM and TEM Micrographs of Manganese Oxide.....84

Figure 6.3. Manganese Oxide Micrographs of Particles with a 1:10 Base Ratio 84

Figure 6.4. Manganese Oxide Micrographs of Particles with a 1:15 Base Ratio 85

Figure 6.5. Mn_3O_4XRD with Computational XRD Overlays and Crystal Unit Cell Rending Generated using VESTA 86

Figure 6.6. Mn_3O_4 XRD with Computational XRD Overlays and Crystal Unit Cell Rending Generated using VESTA 87

Figure 6.7. Mn_3O_4 XRD with Computational XRD Overlays and Crystal Unit Cell Rending Generated using VESTA 87

Figure 6.8. a) XRD of Mn_3O_4 Nanoplates at Room Temperature, b) XRD of Mn_3O_4 Nanoplates Annealed at 300 °C for 1 Hour, c) XRD of Mn_3O_4 Nanoplates Annealed at 550 °C for 1 Hour 89

Figure 6.9. TGA of Mn_3O_4 Nanoplates under Nitrogen Atmosphere using a Platinum Pan 90

Figure 6.10. FITR on Pre-Annealed Mn_3O_4 Nanoplates 91

Figure 6.11. SEM and TEM Micrographs of Copper Oxide with a 1:5 Molar Ratio 93

Figure 6.12. SEM and TEM Micrographs of Copper Oxide with a 1:10 Molar Ratio 94

Figure 6.13. SEM and TEM Micrographs of Copper Oxide with a 1:15 Molar Ratio 94

Figure 6.14. CuO XRD at a 1:5 Molar Ratio with Computational XRD Overlays and Crystal Unit Cell Rending Generated using VESTA 95

Figure 6.15. CuO XRD at a 1:10 Molar Ratio with Computational XRD Overlays and Crystal Unit Cell Rending Generated using VESTA 96

Figure 6.16. CuO XRD at a 1:15 Molar Ratio with Computational XRD Overlays and Crystal Unit Cell Rending Generated using VESTA 96

Figure 6.17. SEM and TEM Micrographs of Magnesium Hydroxide with a 1:5 Molar Ratio 99

Figure 6.18. SEM and TEM Micrographs of Magnesium Hydroxide with a 1:10 molar ratio 99

Figure 6.19. SEM and TEM Micrographs of Magnesium Hydroxide with a 1:15 Molar Ratio 100

Figure 6.20. $Mg(OH)_2$ XRD at a 1:5 Molar Ratio with Computational XRD Overlays and Crystal Unit Cell Rending Generated using VESTA 101

Figure 6.21. $Mg(OH)_2$ XRD at a 1:10 Molar Ratio with Computational XRD Overlays and Crystal Unit Cell Rending Generated using VESTA 102

Figure 6.22. $Mg(OH)_2$ XRD at a 1:15 Molar Ratio with Computational XRD Overlays and Crystal Unit Cell Rending Generated using VESTA 102

Figure 6.23. SEM and TEM Micrographs of Chromium Oxide with a 1:5 Molar Ratio 104

Figure 6.24. SEM and TEM Micrographs of Chromium Oxide with a 1:10 Molar Ratio 104

Figure 6.25. SEM and TEM Micrographs of Chromium Oxide with a 1:15 Molar Ratio 105

Figure 6.26. Chromium Oxide XRD of Particles with a 1:5 Molar Ratio 106

Figure 6.27. Chromium Oxide XRD of Particles with a 1:10 Molar Ratio 106

Figure 6.28. Chromium Oxide XRD of Particles with a 1:15 Molar Ratio 107

Figure 6.29. SEM and TEM Micrographs of Strontium Oxide with a 1:5 Molar Ratio 109

Figure 6.30. SEM and TEM Micrographs of Strontium Oxide with a 1:10 Base Ratio 109

Figure 6.31. SEM and TEM Micrographs of Strontium Oxide with a 1:15 Base Ratio 110

Figure 6.32. Strontium Oxide XRD of Particles with a 1:5 Molar Ratio 111

Figure 6.33. Strontium Oxide XRD of Particles with a 1:10 Molar Ratio 112

Figure 6.34. Strontium Oxide XRD of Particles with a 1:15 Molar Ratio 112

Figure 7.1. Electrical Conductivity of Mn_3O_4 Nanoplates Pressed as a Pellet 115

Figure 7.2. Seebeck Coefficient of Mn_3O_4 Nanoplates Pressed as a Pellet 116

Figure 7.3. Power Factor of Mn_3O_4 Nanoplates Pressed as a Pellet 117

Figure 7.4. SEM of Surface of Pellet after Thermal Cycling and Pressing Particles 118

Figure 7.5. TEM of Nanoplates Scraped from the Surface of the Pellet after Thermoelectric Property Evaluation 119

Figure 7.6. SEAD of Nanoplates Scraped from Surface of Pellet 119

Figure 7.7. XRD of Pellet after Thermal Cycling and Pressing Particles 120

Figure 7.8. XRD of Manganese (II,III) Bulk Powder Overlaid with the Computational XRD Pattern for Mn_3O_4, COD ID: 1011262 121

Figure 7.9. Electrical Conductivity of Manganese (II,III) Oxide Bulk Powder 122

Figure 7.10. Seebeck Coefficient of Manganese (II,III) Oxide Bulk Powder 122

Figure 7.11. Mn_3O_4 Crystal Structure, COD ID: 1011262 124

Figure 7.12. Band Structure of Mn_3O_4 Computed using Quantum ESPRESSO 125

Figure 7.13. MnO_2 Crystal Structure, COD ID: 1514101 126

Figure 7.14. MnO_2 Computed Electrical Conductivity with Respect to Temperature and Chemical Potential 127

Figure 7.15. MnO_2 Computed Seebeck Coefficient with Respect to Temperature and Chemical Potential 127

Figure 7.16. MnO_2 Computed Power Factor with Respect to Temperature and Chemical Potential 128

Figure 7.17. MnO_2 Computed Band Structure using Quantum ESPRESSO 129

CHAPTER I

INTRODUCTION

I.1 Introduction to Thermoelectrics and Thermoelectric Performance

Modern civilization and all its derivative activities are powered by an immense amount of energy, most of which is wasted by rejecting heat into the environment[4]. These inefficiencies not only misdirect large amounts of capital but also produce enormous amounts of greenhouse gases. The implementation of energy recovery technology has the potential to address both these issues; Thermoelectric generators (TEG) would be the ideal solution. TEGs use a temperature difference to convert heat into electricity with no moving parts. They operate silently, are scalable, and reliable requiring very little to no maintenance[2].

To illustrate the magnitude of how much energy is wasted globally, data from the International Energy Agency (IEA) shows that total global energy consumption was 474×10^{15} J as of 2016. Due to low efficiencies only approximately 133×10^{15} J of that energy was directly used in all sectors including: transportation, industrial, residential, and commercial. This implies that 340×10^{15} J of energy is rejected as exhaust heat for the most part. When all energy flows are accounted for, 72% of all energy is lost during energy conversion (e.g. burning coal to produce electricity using a steam turbine)[1]. According to the Department of Energy (DOE) report, utilizing current TEGs with a maximum efficiency of 5%, the potential energy recovery from US manufacturing alone

would amount to 6.5-16.4 TWh for 2010 amounting to 1.5-3.7% of all estimated waste heat energy[3]. Using thermoelectric generators to recover just a fraction of this waste heat and convert it to electricity appears at first glance to offer an obvious and simple solution. This conclusion is null through due to several inherent issues with the current class of thermometric materials. Thermoelectric generators were used in a verity of applications in the 20th century where efficiency was not prioritized, and energy was readily available[4]. TEGs have been used in a range of applications ranging from powering seismometers in Alaska[5] to powering space craft that operate in the outer Solar System such as Cassini around Saturn, New Horizons that passed by Pluto and Curiosity, the rover on Mars[6]. These applications clearly indicate the utility of TEGs, but their inherent flaws prevent them from being used as a solution to the problem of waste heat. If the performance of TEGs can be improved and the cost to produce the devices can drop, the implementation of this technology in new sectors becomes economically viable[7]. Efforts are currently underway to drastically increase the efficiency of automobiles by turning the exhaust heat into electricity thereby assisting the alternator[6]. The same improvements to thermoelectric (TE) materials that could make them viable for the auto industry also could allow Peltier coolers to replace compression-based refrigeration[7]. Thus, the goal of TE research in the 21st century is to design new materials that operate at high efficiencies and have a low cost of manufacturing.

The modern rush to develop new TE materials stared in the early 1990s. Hicks and Dresselhaus proposed that quantum wells could be used to improve the efficiency of Bismuth Telluride, which had shown very little improvement in efficiency since the

1960s[8,9]. They proposed using a superlattice to act as a quantum well restricting phonon modes in the materials thereby reducing the thermal conductivity[10]. The performance of a thermoelectric material is inversely proportional to the thermal conductivity; therefore reducing it will increase the conversion efficiency. Additionally, superlattices introduced the field of nanoscience and nanotechnology to thermoelectric. Nanostructuring a material can drastically alter the properties of that material; a common example is making gold nanoparticles. When gold approaches the size of 10 nm the color of the metal changes to a red, the melting point drops and it can act as an excellent catalyst[11]. Changing the structure changes the materials properties. The introduction of boundaries in a material, as illustrated by Hicks and Dresselhaus in theory, does in fact reduce the thermal conductivity. The thermal conductivity of silicon can be reduced more than two orders of magnitude if it is made into polycrystalline nanowire[10]. The thermal conductivity of silicon can also be reduced by introducing holes into a nanostructure that block phonon modes leading to a similar drop in how thermally conductive the material is[12]. Superlattices and nanostructures are the key to reducing the thermal conductivity of a material; this is a predictable result of nanostructuring a material[13,14]. Other methods that have been used to reduce thermal conductivity include: disordering of unit cells, resonant scattering and interface scattering and natural superlattices[15].

While over the past two decades significant research advancements have been made to enhance the performance of TE materials, the limits of lowering thermal conductivity has been explored. The path forward to enhance performance is to increase the electrical conductivity and Seebeck coefficient of the materials while simultaneously

reducing the thermal conductivity. To enhance these properties, it is necessary to understand how to design and control the charge-transport mechanics of a material[15]. Methods have been proposed to design these parameters using potential barriers and band-structure design[4,16], but better models are needed to properly predict and therefore design how electrons flow through a material.

The capability to predict and design materials with specific properties is one of the largest issues facing material science, physics and nanoscience. If a solution was found to this problem, then new materials could be rapidly developed and deployed to the market. Currently, the development of new materials could be described as an intelligent random walk where a new synthesis is done based on past experience and literature and then characterized and iterated upon. While this method works, it is laborious and time consuming. Currently, development takes between 10-20 years[17]. Ideally a set of laws should be created that can be used to engineer materials, i.e. 'materials by design'. In the interim, accelerating the progress of iterating and screening materials can be done computationally. The Materials Project[18] is an attempt at doing this by using computational methods and supercomputers to predict the properties of materials based on their atomic configuration. The ability to rapidly predict the properties of materials allows for many different materials to be 'tested' and then screened for the best. While this is still a brute force method, it does accelerate the process of finding new materials[18].

If these two laborious methods are to be bypassed and a true 'materials by design' approach is to be adopted, complex modeling is required. All methods currently used to build these complex models include machine-learning, big data, and artificial

intelligence. These methods require large amounts of data, which is being generated in large sets with the current iterative methods used both in the lab and computationally. Currently researchers are using machine-learning on large data sets to predict new materials; this goes beyond predicting and screening, it allows for specifying desired properties and designing the materials that will give those properties[19]. An initial step has been taken toward using machine-learning for predicting thermoelectric properties with the online tool: ThermoEl[15]. This method uses real data to make models where new materials are then entered to predict the Seebeck coefficient of that material. While it does a good job, Seebeck coefficient cannot be used alone to predict the performance of a thermoelectric material[15]. While this was a very promising first step for predicting new materials, much more needs to be done.

Regardless of any future methods used to create materials, either via laborious processes or designed, it needs to be rapid. This narrows it to either computational screening or complex modeling. This will require high quality predictive algorithms, especially for nanomaterials. At the moment though, only the initial stages of making a predictive machine learning algorithm have been worked on as reflected in literature. Massive databases will be needed to make these algorithms work. The creation of these databases will require a rapid method of either measuring or predicting those properties of thermoelectric materials. It is clear that improving the performance of thermoelectric material is doable using nanostructures; the impact of nanostructuring materials is clear on the thermal conductivity. What is not clear is the impact on the electrical properties. For any predicting algorithm to be created large datasets on nanomaterials would need to

be assembled for data mining.Building these databases could in theory be done computationallyby further addingthe amassed experimental data in literature, but that will require verification that the current models work well enough to generate the data by comparing their experimental results to literature data.

I.2 General Goal of the Research

The goal of this research is todevelop a rapid property prediction method combining computational and experimental approaches that enable the creation of new thermoelectric materials. To achieve this goal, this dissertation project will first design a computational search engine to identify new materials by predicting their thermoelectric properties, which include: electrical conductivity, thermal conductivity, and the Seebeck coefficient. Then the project will choose the materials with good predicted thermoelectric properties, fabricate them on the nanoscale, evaluate their thermoelectric properties and compare with computationally predicted TE properties of respective materials to the measured properties. Through this approach, this dissertation will test the hypothesis of nanostructuring a material that may have a higher thermoelectric performance could show if this method offers a promising path forward for the development of thermoelectric materials.

According to Semantic Scholar in 2017, 748 papers on “Thermoelectrics” were published. In 2016 the number was 750. The trend line from the 1950s is upward, but these numbers are still low. Semantic Scholar also shows in 2017, 1871 papers were published on “photovoltaic solar panel”. In 2016, the number was 2451. Thermoelectrics, compared to photovoltaics, is a much smaller field.This also means that far fewer

potential materials have been explored. To find new materials, a rapid assessment is needed on unknown compounds. The traditional way of testing a material would be to synthesize it and proceed to measure its properties. This method is limited due to the near infinite number of materials that could be made; therefore, a different method is needed to search for materials. The proposed approach focuses on computationally predicting the thermoelectric properties of a given material. If a material's properties can be predicted, even with error, a large set of compounds could be examined and then the best can be chosen to experimentally synthesize and test. For example, if there are 1000 unknown materials that might be promising, then there properties can be computed. If say only 20 of them are predicted to have good properties, then only those 20 needs to be synthesized and tested. The other 980 can be used as raw data for machine learning and big data studies if that path is pursued. The aggregation of large raw datasets from current computational methods would enable the creation of these new computational models that could not necessarily be done using more traditional experimental methods. These models could be used to engineer future material no longer requiring the need for large computer system to compute the chosen materials properties. A Newton's laws equivalent for thermoelectric materials might be possible, but large amounts of data is needed to develop those empirical equations.

After new materials have been identified by computational search engine, they can be fabricated and tested. While in theory a material might be good, in reality the likelihood of achieving the ideal theoretical thermoelectric properties are very remote. The universally accepted measurement of a thermoelectric performance is called the

Figure of Merit and as an example, if a material is predicted to have a Figure of Merit of 2, then in reality it might only approach a value of 1 in the lab. To search for the best materials right now, computational methods are, at least in theory, far quicker than laborious experimental methods in the lab. As discussed, a nanostructured material has enhanced properties that are desirable for thermoelectric applications. However, the challenge with nanostructures is computing their properties using conventional methods. The quickest method of predicting the properties of a materials is computing its properties in the bulk form, considering its crystal lattice instead of a nanomaterial. Predicting properties of a material using its single crystal lattice structure eliminates the need of high-end computational requirements as well as computational time. With current technology it is only realistic to compute the thermoelectric properties of a respective material's crystal lattice, but we want the advantages of a nanostructured material, the problem is how TE properties of a material's crystal lattice prediction can inform the properties of a nanomaterial.This issue might be addressed by showing that a crystalline structure of a nanomaterial governs the same crystal unit cell as the respective crystal lattice structure of the bulk form of the material. This comparison may give an idea on the TE behavior of the respective nanomaterial's counterpart. On the other hand, this might be extended to the fact that the exact properties do not need to be known; as an example if the crystal lattice structure of a material exhibit a promising Figure of merit, which is predicted and experimentally measured, it's nanostructure form may exhibit a considerable increase in the in ZT as previously shown in the literature[3] However it is not clear yet how linear of a relation it is between finding a material that is good and

nanostructuring it to make it better. In some cases it might be that a good material might be horrible on thenanoscale and vice versa.This relationship has not been explored yet and need to be studied in depth combining computation predictions and experimental data.

Recent research findings have evidenced that nanomaterials exhibit the most promising path to create novel thermoelectric materials. The same material with the same atomic unit cell and same collection of atoms can display vastly different properties at macro- and nanoscale. At the nanoscale, these materials bring quasi quantum properties to its respective material's crystal lattice structure. Thermoelectrics until now have been made from macro-scale (bulk) materials, typically from powder that is pressed into blocks and sintered at high temperatures[20]. These bulk materials, such as Lead Telluride, have shown massive improvements in ZT when grains are introduced into the pressed materials structure, which is effectively similar tointroducing self-assembled nanocrystals into the nanomaterials[20]. The method of pressing pure powders or growing single crystal materials, while it works to produce TEG'shave been far too inefficient to use in any real application at large scale. This indicated that the traditional macro-scale materials processing methods of making thermoelectric materials needs rethinking and possibly, nanostructures may be an approach to overcome the challenge of scale up.

If the new materials are going to be nanostructured, large scale manufacturing costs of these theoretical TEGs needs to be addressed. One example of manufacturing very small devices is the semiconductor industry CPUor GPU chips are small enoughthey are approaching the quantum realm, making them very expensive to manufacture owing

to traditional top down approach. Nanomaterials are offering a new direction for device properties as well as device manufacturing. Materials like nanowires, with diameter around 50 nm and several microns in length, offer unique properties such as quantized electrical conduction and rapid drops in thermal conductivity. These property changes can contribute in a very positive way to the figure of merit (ZT) as discussed above. Nanowires can be made using very simple methods such as sol-gel approaches in solution instead of using expensive equipment in a clean room environment. If thermoelectric materials were to be made this way it would drastically reduce the cost of manufacturing increasing the Return on Investment (ROI) of TEGs.

Therefore, in this dissertation, a combination of both the computational search and bringing the macro-scale materials (bulk form) into nanoscale materials via nanomaterials synthesis to create high efficiency thermoelectric generators has been proposed as a possible solution when searching for new materials. To make new materials, it will be necessary also to make them from abundant elements. Current thermoelectric materials are made from earth-rare materials, like Lead, Bismuth and Tellurium, and all of they are also heavy metals. If new materials are going to be created using lighter elements, which is almost a given seeing that there are very few elements that are heavier, those elements will be more abundant leading to a lowering of material cost.Making TEGs from more abundant elements, for example, magnesium, strontium, chromium, will necessarily make those elements lighter than Bismuth and Tellurium.These lighter elements could in theory produce the same power output as a traditional thermoelectric material, but its energy conversion efficiency will be drastically

impaired by it thermal conductivity being higher. For lighter elements, there are more vibrational phonon modes than for heavier elements[12]; corresponding with a higher thermal conductivity and therefore lower conversion efficacy. This is another reason that nanostructured materials are such a powerful tool to make new materials; the power conversion efficiency might not change if a new material is invented, but by changing what it is made,the overall cost of material can decrease to make it more applicable for industries in the world. The reduction of the thermal conductivity of a material by nanostructuring is best illustrated by a Silicon nanowire, in which a crystalline nanowire has approximately an order of magnitude drop in its thermal conductivity compared to its bulk value[10]. This change can be pushed further by making an amorphous silicon nanowire dropping the thermal conductivity to the theoretical minimum, or Casimir limit, with a drop of two orders of magnitude compared to the respective bulk form. It has also been reported that a polycrystalline nanowire made from silicon can drop the thermal conductivity below the Casimir limit[10] as shown in Figure 1.1. This work from Zhou et.al., demonstrated that small nanocrystals of Si integrated into the polycrystalline matrix causes the thermal conductivity to continue to drop.

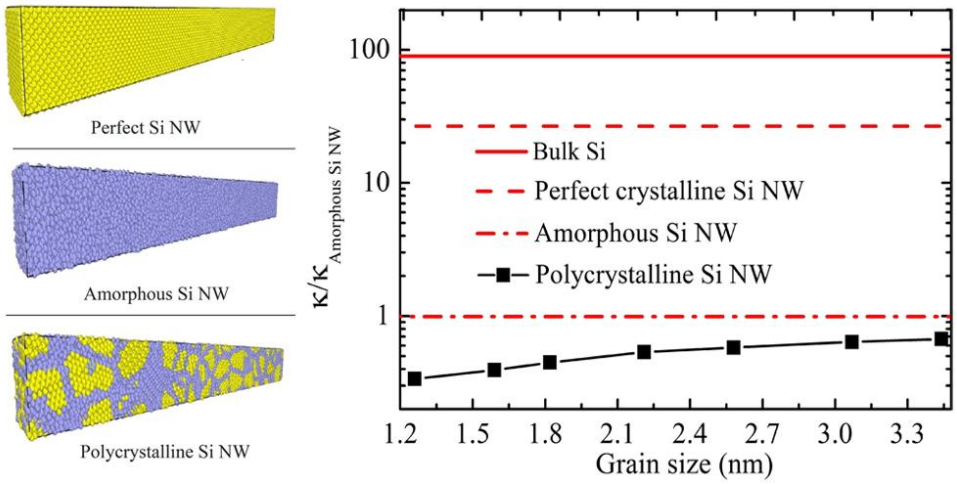

Figure 1.1. The Reduction of Thermal Conductivity in Silicon using Nanowires and how the Arrangement of Atoms in that Matrix Changes the Conductivity[10].

If new materials are found using computational methods, they can be structured on the nanoscale and tested if they are better for TEGs than the current State-of-the-Art. The initial attempt inthis dissertation was focused on making nanowires and have them aligned perpendicular to a substrate making tandem structure of p- and n- junctions. An illustration of this is shown in Figure 1.2. These nanowires could be layered further reducing the thermal conductivity and introducing unique electrical properties into the system.

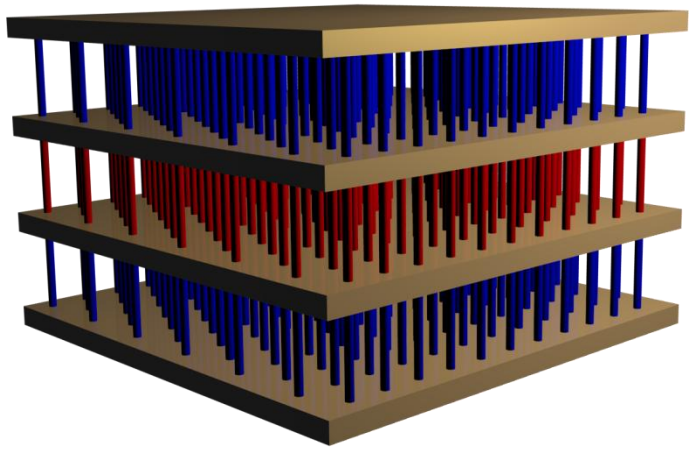

Figure 1.2. Tandem System of Nanowires for Thermoelectric Applications.

This tandem architecture could act as electrical conductors while minimizing thermal conductivity. Making nanowires with a wet synthesis process is relativity simple. In the past, our group has showed a simple sol-gel method to make aligned ZnO nanowires via solvothermal method[21]. In our initial attempts, we augmented synthesizingother D-band element-based wires including copper, chromium, or iron. If the nanowires could be made in solution then they could also be grown from a nucleation point on a substrate. However, prior to this step, we wanted to augment the sol-gel synthesis method to make other nanostructures other than ZnO and evaluate their thermoelectric properties in the form of pressed pellets. If the selected materials show promising thermoelectric properties, the future work will move with investigating the tandem structure to improve the thermoelectric performance. Thus, this dissertation aims at developing a rapid materials development method using computational predictions and make nanoparticles of few selected metal oxides and evaluate their thermoelectric

properties experimentally and compared with predicted properties of their respective metal oxides in the bulk form.

Aiming for the above target, this dissertation develops an aqueous-based sol-gel synthesis method to make nanomaterials in powder form with different morphologies at larger scale.We explore the possibility of performing these reactions at low temperatures, in different solvents, and in some cases only water to produce nanoparticles in a large scale. Then, these nanoparticles will be pressed into a pellet for evaluating the thermoelectric parameters. These pellets will be sintered, while maintaining the nanoparticles crystallinity and morphology and then cut into the needed shapes for TEGs. This process is very similar to those used in current pellet production in for TEG fabrication[22], but nanometer scale particles are used instead macro-scale powder. Typically power to be pressed is made in a high temperature furnace where raw materials are mixed together and heated in an ampoule to form a crystal. The pellet is then crushed into a powder and molded into the needed shapes for TEGs. This method has limitations due to the size of the particles that can be produced.

Nanoparticles offer much more potential than macro- and micro-meter sized particles produced by a ball milling process. The past literature has shown that the transition from the bulk realm to the quantized realm could provide void spaces with grain boundaries that enable to freeze phonon modes[10] and radically reduce the thermal conductivity. This cannot happen with traditional pellet production with macro- and micron-sized particles where the phonon modes are simply not frozen out.

Another advantage of nanoparticle approachis it provides an effective path to meta doping with meta-doping with other metal ion centers. Doping materials on the atomic level is needed for fine tuning thermoelectric materials. Thermopiles optimally work when there are *p*- and *n*-doped materials. Meta-doping provides “artificial atoms”, or nanoparticles. The performance of these materials can be changed by mixing different types of metal precursors during the nanoparticle synthesis in different concentrations, effectivelydoping the material.

The faster turn-around time for experimentation, an established method for particle production, the established method for TEG material production, and the possibility of meta-doping makes this path forward appear very promising. All this combined with computational property prediction enables a framework to be put in place that allows for many new materials to be made and tested. Therefore, the overall goal of this dissertation is to build the infrastructure that enables the rapid discovery of new materials.

CHAPTER II

LITERATURE AND BACKGROUND

II.1 Metrics of Material and Device Characterization

Thermoelectric devices (TED) are made by alternating *p*-*n* junctions, known as a thermopile, where a temperature difference across the TED induces a voltage that drives a current, producing power. The TED materials must be doped differently depending on how current should flow in the circuit. The temperature gradient will drive electrons of the *n*-type materials from the heat source to the sink. In the *p*-type material, holes flow from the heat sink to the heat source. The flow of the holes and electrons induces a current in one direction. Figure 2.1 depicts a schematic design for a typical TED.

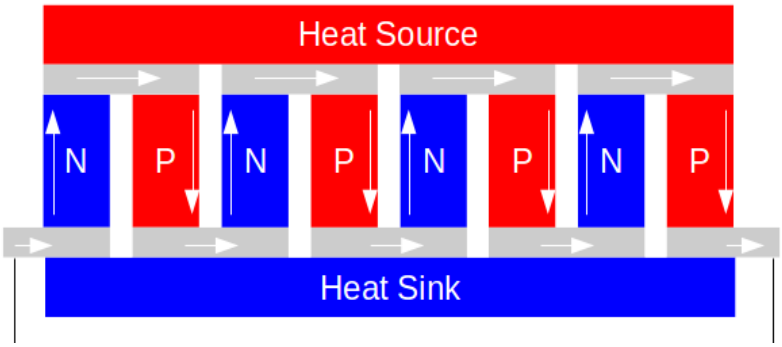

Figure 2.1. A Schematic Diagram of a Typical TED Design.

The goal of thermoelectric research in the 21st century is to make TEGs operate at high efficiency while having a low cost of production and distribution. The figure of

merit, ZT, is the typical method used in academic research and industry to measure the performance of thermoelectric materials. To improve the ZT of a material, the thermal conductivity, electrical conductivity, and Seebeck coefficient must all be improved independently[4]. ZT is defined in Eq. 2.1. S is the Seebeck coefficient, σ is the electrical conductivity and both κ_e and κ_l is the electron and lattice thermal conductivity respectively.

$$ZT = \frac{\sigma S^2}{\kappa_e + \kappa_l} T; Eq. 2.1$$

Reducing the TE materials thermal conductivity, κ_l has been the main path forward to increasing ZT; improving the materials electrical conductivity and Seebeck coefficient is the next frontier for improving the ZT[13]. Current methods to improve the electron properties include: modulation doping, band convergence, classical and quantum size effects, spin Seebeck effect and topological states[4]. Modifying the electrical properties of a TE material changes the power output from the materials. A way of quantifying the power output of a material is the Power Factor. Power Factor (PF) is defined in Eq. 2.2.

$$PF = \sigma S^2 = ZT(\kappa_e + \kappa_p);\ Eq. 2.2$$

PF has units of $Wm^{-1}K^{-1}$ and is in contrast to the dimensionless ZT. PF can be used to calculate the amount of power from a thermoelectric material that output at a specific temperature, but provides no relevant information on the thermodynamic

efficiency of the material. The efficiency of a TEG using ZT is defined in Eq 2.3, which has a similar form to Carnot efficiency from thermodynamics.

$$\eta \equiv \frac{W_{out}}{Q_{input}} \rightarrow \eta_{max} = \frac{T_H - T_C}{T_H} \frac{\sqrt{(1 + Z\bar{T})} - 1}{\sqrt{(1 + Z\bar{T})} + T_C/T_H}; Eq. 2.3$$

The efficiency of a TEG depends on the ZT of two thermoelectric materials in a P-N junction as depicted in Figure 2.1. ZT for two materials is similar to that of one material, which is defined in Eq. 2.1. Thus, ZT for a P-N junction is defined in Eq. 2.4.

$$Z\bar{T} = \frac{\left(S_p - S_n\right)^2 \bar{T}}{\left[\sqrt{(\rho_n \kappa_n)} + \sqrt{(\rho_p \kappa_p)}\right]^2}; \; Eq. 2.4$$

Just like the Carnot efficiency, if the temperature difference increases the efficiency increases, but for TEGs a non linear scalar is a factor in the efficiency, which depends on ZT. Therefore, to improve efficiency, ZT needs to be increase. All variables in ZT are interconnected. For example, changing the atomic structure changes how phonons propagate and the material's band-structure. The variables most interconnected are the electrical conductivity and the electron contribution to thermal conductivity.The electrical conductivity of a material relates to the electron thermal conductivity, κ_e, with the Wiedemann-Franz law, defined in Eq. 2.5.

$$\frac{\kappa_e}{\sigma} = LT, L = 2.44x10^{-8} W\Omega K^{-2}; Eq. 2.5$$

This implies that if a material had a high enough electrical conductivity a high electron thermal conductivity becomes the main contributor to overall thermal conductivity. To minimize this effect and maximize ZT, the most important variables to optimize are the Seebeck coefficient and the lattice thermal conductivity. This relationship should be a guiding principle, but not necessarily always heeded as there are some exceptions to the Wiedemann-Franz law. A notable example is vanadium dioxide, which was recently shown that the law breaks down leading to a material that is a very good electrical conductor but has a very low thermal conductivity. The electron thermal conductivity was an order of magnitude lower than expected according to the Wiedemann-Franz law. The reasoning presented on the topic was a quantum state where electrons were not propagating heat[23].

II.2 State-of-the-Art for Materials

The parameters that need to be changed to improve ZT are known, but it is just not clear how to design materials that have those parameters. Thus, a rapid screening process using computations is a critical need and therefore the models need conformation. If TEDs are used at scale, new materials must be designed to have a high ZT at a low cost. These criteria is not met by materials, which are on the market today and are listed in Table 2.1[24]. These materials exist in the market at the moment but are evident that there is much room for improvement. A figure of merit in the range of these materials translates to ~4-5% efficiency with a temperature difference of 350 °C. According to the Department of Energy, a TEG with the heat sink at 50 °C and the heat source at 250 °C, and ZT of 1 shows 11% power conversion efficiency. Increasingthe ZT

to 3 could increase the efficiency to 19%. Current generators in the lab settings have achieved a ZT of 2.27 with the assistance of nanotechnology, but far more work is needed to make these gains marketable[7].

Table 2.1. Cost and ZT of Current Thermoelectric Materials

Material	Price per kg	Figure of Merit
Bismuth Telluride	$110/kg	ZT = 0.4
Half Heuslers	$146/kg	ZT = 0.45
Lead Telluride	$84/kg	ZT = 0.49
Skutterudites	$24/kg	ZT = 0.58
Tetrahedrite and Silicide	$4/kg	ZT = 0.65

These materials are the most common on the market or in the lab. Other materials do exist, but with alow Figure of Merit. These devices are not economically comparable with the price of producing power with more traditional methods, such as boiling water and driving a turbine. The prices per watt for each energy production source is listed in Table 2.2[7,25,26]. This indicates that if TEGs are going to be used in an industrial setting and no other heat recovery technologies available, the materials need to become cheaper. To further illustrate the need to change materials, in the DOE thermoelectric report, it is clear that ZT can be drastically improved utilizing nanotechnology, assuming that nanostructuringmay improve ZT by a factor of 2-5. According to Table 2.1, for example, Bismuth Telluride would have a ZT of 0.8-2.5.This is in the right range for a high efficiency TEG, but the price is still $110/kg. In fact, the price would most likely be higher due to the processing of the material into nanostructures.

The raw minerals that are refined into different elements are the underlying cost indicator for how expensive a material to be produced (e.g. Bismuth Telluride and Lead Telluride)[27]. According to a report issued by the European Union, minerals or materialswith following elements, have a supply side risk. Such elements are: *Antimony, Beryllium, Borates, Chromium, Cobalt, Fluorspar, Gallium, Germanium, Indium, Magnesite, Magnesium, Natural Graphite, Niobium, Phosphate Rock, Silicon Metal and Tungsten*[28]. These elements were determined by analyzing the supply chain and other factors such as depletion of the elements/minerals. Chromium appears to be on the list due to where it is mined, not due to the supply depletion. According to the United States Geological Survey (USGS), the majority of Chromium is mined in South Africa and Kazakhstan, but there is an estimated 12 billion metric tons of Chromium in the Earth's crust. It is also well established by the American Chemical Society that there are "*endangered elements*"[29].

Table 2.2. Power Production and Thermoelectric Power Generation Comparison.

Application Temperature	**Power Generation Technology**	**System Cost ($/W)**	**Efficiency**
Low (T_h ~ 100 ºC)	Geothermal	$4.14	N/R
	Half-Heusler Thermoelectric *Bulk Elements*: Zr, Hf, Ti, Ni, Sn, Sb	$125.05	1.3%
	Silicon Nanowire Thermoelectric	$104.18	N/R
	Chalcogenide Thermoelectric *Nanobulk Elements*: Bi, Sb, Te	$62.44	< 1%
Medium (T_h ~ 250 ºC)	Organic Rankine Cycle	$4.00	N/R
	Concentrating Solar Power	$3.60	N/R
	PV Target	$1.00	N/R

	Skutterudite Thermoelectric *Bulk Elements:*Yb, In, Co, Sb	$19.02	2.8%
	Half-Heusler Thermoelectric *Bulk Elements*: Zr, Hf, Ti, Ni, Sn, Sb	$14.45	3.5%
	Chalcogenide Thermoelectric *Nanobulk Elements*: Bi, Sb, Te	$11.92	2.8%
High (T_h ~ 500 ºC)	Nuclear	$5.34	N/R
	Coal	$2.84	N/R
	Natural Gas	$0.98	N/R
	Silicide Thermoelectric *Bulk Elements*: Mg, Si, Sn	$5.56	6.0%
	Chalcogenide Thermoelectric *Bulk Elements*: Ag, Pb, Sb, Te	$5.06	N/R
	Half-Heusler Thermoelectric *Bulk Elements*: Zr, Hf, Ti, Ni, Sn, Sb	$4.48	7.5%

Using the *Mineral Commodity Summaries* from 2017 published by The USGS, different elements were identified that have a longer time span than 20 years before demand over takes supply. This was calculated by looking at supply-to-production ratio. For the sake of near term TEGs, 20-year time span is a decent period of time to adjust as minerals become scarcer in the future. According to the data, the following elements have been chosen in this thesis work to produce a better thermoelectric generator: *Magnesium, Calcium, Strontium, Chromium, Molybdenum, Iron, Nickel, Copper, Zinc, Sulfur and Selenium.*

II.3 Improving Material Performance using Nanostructures

A material that fits the requirements of the allowed elements would be transition-metal-dichalcogenides, which includes elements from Group (VI) and (XVI)[30]. Only a

few papers have been published relevant to these elements for thermoelectric applications, but the results appear promising. In a recent computational study, it has been shown that nanoribbon made from alternating Molybdenum (Mo), Tungsten (W), Sulfur (S) and Selenium (Se) can yield figure of merit to 7.4 at the high end according to the computations[30]. Another paper reported sintered pellets of $CrCuS_2$has yielded a ZT of 2.0[31] owing to its nanostructuring like morphology. It is evidenced that the introduction of nanostructures into the materials would create periodic boundary conditions in the crystal lattice and therefore lower the thermal conductivity.

Both literature and theory show that the introduction of boundaries into a material will reduce the thermal conductivity. For any given lattice of atoms, there is a set of possible modes of vibrations that the atoms can oscillate at. These modes provide the transport mechanism of thermal energy. The wave packets are called phonons, which exist in two forms: acoustic and optical[9]. Other forms of waves that can exist in non-crystalline material include Diffusons, Locons and Propagons[32]. Possible modes of phonons in crystalline materials can be 'frozen' by shrinking the material to the nano scale. This can be done using theory and computational methods. Using the software *Alamode*, the thermal conductivity of Silicon was computed. The thermal conductivity of a particle of Silicon is the summation of all modes that can exist in that particle.

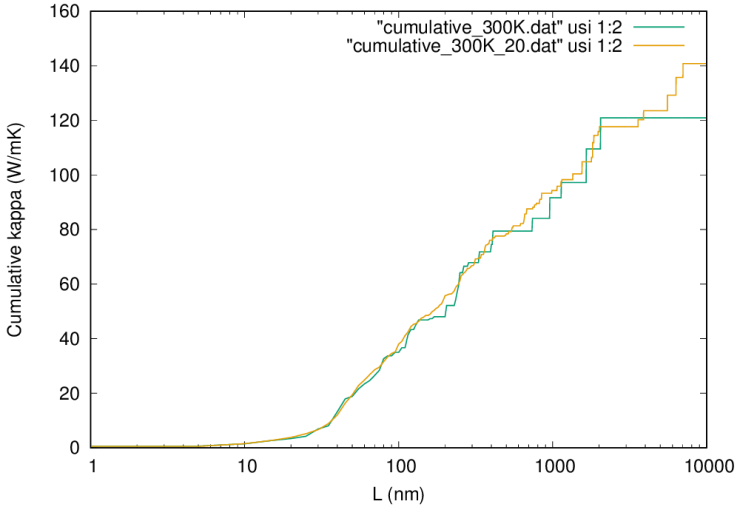

Figure 2.2. Cumulative Thermal Conductivity of Silicon.

As shown in Figure 2.2, as silicon shrinks, different phonon modes are frozen, leading to a drop in the cumulative thermal conductivity[33]. This supports the nanostructuring phenomena, which can increase ZT for thermoelectric materials phonon modes are frozen out the thermal conductivity drops. Figure of merit is inversely proportional to thermal conductivity. So as long as the electron contribution stays low, nanostructures increase thermoelectric performance of materials. This indicates that any potential new material can be improved further by introducing nanostructures form, resulting in reducing phonon modes.

CHAPTER III

AIMS AND OBJECTIVES

The overarching research hypothesis of this work is: At nanoscale, metal oxides will improve the thermoelectric figure of merit by lower the lattice thermal conductivity through the introduction of nanocrystals. Bringing down the materials from macro-scale to nano scale will also scale the electrical conductivity and Seebeck coefficient, contributing to overall thermoelectric performance. When moving from top-down to bottom-up approach, predicting how the material's properties changes using existing computational methods are necessary. To reach this goal, a computational engine will be developed to predict the properties of metal oxides and compared the predicted properties with experimental property of their respective nanostructure forms, focusing following three aims.

III.1 Aim 1: Developing a Computational Method to Predict Thermoelectric Properties of Inorganic Materials

Hypothesis: Utilizing existing computational methods, a computational engine can be developed to predict the thermoelectric properties of inorganic crystalline materials, having periodic crystal lattice structure.

Rational: The crystal unit cell and lattice structure of most inorganic materials can be found in the crystallographic open database. Thus, utilizing the crystallographic

information, the method developed can be used to predict the properties of the crystal lattice structure for different elemental compositions of crystalline materials. Under this aim, the following three objectives will be met. (1) Identifying the most abundant elements and minerals using data from published literature and The United States Geological Survey (USGS). (2) Identifying existing software and identifying its weaknesses and strengths, and (3) Assembling the identified software packages into a method that can predict the thermoelectric properties of a periodic single crystal lattice of a selected inorganic material.

Expected Outcomes: All steps will be automated, creating the ability to rapidly predict the thermoelectric properties of crystalline inorganic materials. The materials that will be predicted will be based on the approved elements that were selected from the first objective. The validity of the model will be verified using known materials and applied to new materials to predict the thermoelectric properties of periodic single crystal material.

III.2 Aim 2: Developing a Sol-Gel Synthesis Method to make Metal Oxide Nanostructures and Investigating their Thermoelectric Properties

Hypothesis: A sol-gel method followed by a self-assembly process in the presence of different organic solvent may yield metal oxide nanomaterials with different morphologies.

Rational: A sol-gel approach provides a unique and versatile path to tailor size and shape-controlled nanomaterials with high crystallinity.

To meet this aim, three objectives will be targeted, and include: (1) Develop a sol-gel synthesis method to fabricate nanomaterials using a simple and versatile aqueous

based synthesis method. (2) Study the effect of solvent type and base concentration on the nanocrystal self-assembly and crystal growth to produced size and shape-controlled metal oxide nanomaterials, and (3) Develop a method to evaluate the temperature depended electrical conductivity and Seebeck coefficient of metal oxides.

III.3 Aim 3: Understanding and Correlating the Computationally Predicted and Experimentally Evaluated Thermoelectric Properties of a Selected Metal Oxide

Hypothesis: The computationally predicted TE properties of a metal oxide will be comparable to the experimentally measured TE properties of the respective metal oxide.

The core of this aim is to bring our computational approach and experimental approach together and compare the validity of the computational engine, developed under Aim 1, with the experimental properties measured using methods which developed under Aim 2.

This aim has three objectives. (1) Predict the thermoelectric properties of manganese oxide derivatives (MnO_2 and Mn_3O_4) using the computational engine developed in Aim 1, (2) Test the experimental approach developed in Aim 2 to evaluate the TE properties of Mn_3O_4 macro-scale powder and nanostructures, and (3) correlate the predicted and experimental TE properties.

Expected Outcome: With further development, the computational engine developed in this research will provide a rapid screening tool to search inorganic materials with better TE properties.

CHAPTER IV

APPROACH TO COMPUTATION

IV.1 Identification of Elements for Ideal Thermoelectric Materials

New thermoelectric materials will require new elements to be used not only to expand the scope of known materials, but to also make them practical in the real world. The cost of specific materials can be very high due to the scarcity of the raw materials and elements that go into producing them. Changing the type of elements can also change the toxicity of these new materials; for example, replacing Lead with Copper would change the overall toxicity of lead-based thermoelectric materials. The elements that might serve as a replacement to the current set of elements can be found using current supply, production and reserve data published by national governments. The key metrics, then need to be optimized is; how plentiful these elements are and how susceptible they are to supply shocks and make sure that they will not face any non-linear scarcity in the near future. All data used to determine if specific elements can be used with low risk to supply shock or escalating scarcity was obtained from the United States Geological Survey, or the USGS. Every year the agency publishes the *Mineral Commodity Summaries*; the data used in current as of 2017. A useful measure when forecasting scarcity in the mineral and fuel industry is the supply-to-production ratio. If this ratio is raising than the known accessible reserves in increasing relative to the production.In effect this means the substance is becoming more abundant. If the ratio is falling then the

resource has already reached its peak production. A time series of the supply-to-production data can be used to forecast when peak production is most likely[34]. Using this metric a time period of approximily 20 years was chosen where production will stay the same or rise and therefore offering the potential for abundant and cheap materials. According to the USGS data, the following elements have been chosen for experimentation to produce a better thermoelectric generator: Magnesium, Manganese, Strontium, Chromium, Copper, Molybdenum, Iron, Nickel, Zinc, Aluminum, Sulfur and Selenium. The reserves of these elements are shown in Table 4.1.

Table 4.1. Elements with their Known Reserves and Production Rates[27].

Element	Reserves (Mton)	Resources (Projected) (Mton)	Production (Mton/Year)	R/P Ratio (Years)	R/P Ratio (Projected) (Years)
Magnesium	8.50E+06	1.20E+10	2.77E+04	306.86	9.00
Manganese	6.90E+05	Undefined	1.60E+04	43.13	Undefined
Strontium	6.80E+06	1.00E+09	3.50E+05	19.43	2857.14
Chromium	5.00E+05	1.20E+13	3.04E+04	16.45	394736842.11
Copper	7.20E+05	2.10E+09	1.94E+04	37.11	108247.42
Molybdenum	1.50E+07	1.94E+07	2.27E+04	660.79	854.63
Iron	8.20E+10	1.10E+11	1.36E+08	602.94	808.82
Nickel	7.80E+07	1.30E+08	2.25E+06	34.67	57.78
Zinc	2.20E+08	1.90E+09	1.19E+07	18.49	159.66
Aluminum	Undefined	7.50E+10	5.76E+07	Undefined	1302.08
Sulfur	Undefined	5.00E+09	6.93E+07	Undefined	72.15
Selenium	1.00E+05	Undefined	2.20E+03	45.45	Undefined

How this table is read is buy looking at the R/P ratio. Knowing current reserves, or how much we know can be mined from known deposits in the earth's crust, the rate of extraction can use used to compute how many years of production is left. While some are

quite low, around 15 years minimum, the projected resources from other deposits show that that time window can be drastically expanded.

IV.2 Building a Computational Engine to Predict Thermoelectric Properties

The past research has demonstrated that computational methods such as Density Functional Theory (DFT) can be utilized to predict the thermoelectric properties of a material[35].These papers all point to different software packages that can be used and how they can be integrated together to compute different properties, but no in-depth, high throughput method that is well documented has been generated in literature that can be used to predict thermoelectric properties of a material and provide the ability to screen materials with promising TE properties. The goal of this chapter is to explore the necessary foundation that need to be taken to build a computational engine that can predict the thermoelectric properties of inorganic materials from their known crystal lattice structures. In order to develop the computational method, which also utilizes DFT calculations, a crystalline material (macro-scale powder, i.e., generally called bulk material) is being defined as a single crystal lattice structure that is computed using periodic boundary conditions. In crystallography, a single crystal lattice structure is a periodic array of crystal unit cells, which is the smallest unit of a material. If any computational method were to be applied to just a single crystal lattice structure, the results of those calculations would be comparable to a single nanocrystal, which exhibits the same crystal unit cell structure as the respective macro-material's unit cell structure. Here, all computations are developed for macro-scale materials, utilizing their crystal lattice structure. A unit cell is defined and then periodic boundary conditions are applied

to that unit cell when all calculations are run. The thermoelectric properties that this method predicts are all determined by the variables in the Figure of Merit, which includes: Seebeck coefficient (S), electrical conductivity (σ), and thermal conductivity (κ). In the implementation of DFT for thermoelectric property prediction only TE properties of macro-scale materials, having crystal lattice structure are computed. This is because these properties become exponentially harder to compute for a nanomaterial instead of a material with single crystal lattice structure, as in most cases, nanomaterials are polycrystalline in nature and difficult to define the boundary conditions. Figure 4.1 shows an illustration of the difference between the setup of the unit cell for a material with a single crystal lattice structure and Nanomaterials unit cell.

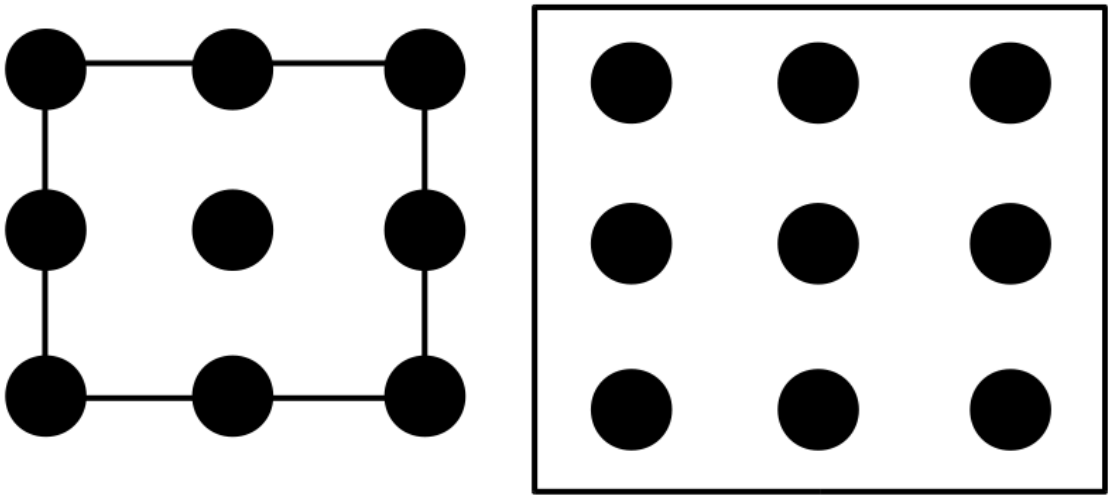

Figure 4.1. (Left) Face Center Cubic Unit Cell that uses Periodic Boundary Conditions for DFT Computations. (Right) Face Center Cubic Unit Cell that Represents a Nanocrystals.

The periodic boundary condition shown in Figure 4.1 illustrates a face center cubic unit cell that has periodic boundary conditions. The box is overlapping the outer atoms indicating that the atoms are 'leaking' into the next unit cell in all directions. This periodic setup is what enables the rapid calculations of a bulk material where the unit cells are periodic in all directions. The nanocrystal illustrated in Figure 4.1 is the same face center cubic structure as the periodic lattice structure of a macro-scale material, but the boundary conditions not periodic. Only the atoms are in the same position. What is introduced here is what is called a vacuum. This box (in the actual system it is a cube) represents the boundaries of the computations. The computations are bound to the box instead of being computed using periodic boundary conditions. This is why a vacuum is used when the properties of a nanocrystal are to be computed. For a nanomaterial all atoms in the system must be specified. The hardware that is available such as workstations today limit work that can be done using DFT for nanomaterials. In this work, vacuum was tried for a short period of time while learning the software packages. The computational time needed to run these on standard workstations stretches into time frames that are not practical. In some cases it could take years to compute the properties of a martial without periodic boundary conditions. Because of these limitations only crystal lattice with periodic structure of material's properties are computed utilizing periodic boundary conditions. These limitations make it impossible at the moment to say where the boundary between a nano and a macro-scale material is using the definitions that are defined here for nano and macro-scale materials or bulk. A typical unit cell is on the order of angstroms in size. Perhaps when a nanomaterial reaches 10 nm the vacuum

no longer has any impact on the computed properties. It could be 10 nm or it could be 100 nm. To use that many atoms though it would require a supercomputer to run those simulations and find those parameters. To illustrate this problem, the band structure of silicon can be computed using DFT and only utilize one to two gigabytes of ram. That is run using a simple face center cubic structure with periodic boundary conditions. In contrast the band structure of a metal organic framework (MOF) known as IRMOF-8 was attempted to be computed using periodic boundary conditions using 568 atoms. It required 1.5 terabytes of ram to run making our hardware useless. If either of these had not used periodic boundary conditions the memory required as well as CPU time would have gone up exponentially relative to the periodic boundary conditions as well. These kind of non linear hardware requirements mean that only the thermoelectric properties of a single crystal with periodic boundary conditions can be computed on a typical workstation. Anything beyond that at the moment would require a super computer.

The physics of why shrinking a material to the nanoscale reduces its thermal conductivity is well understood. What does not appear to be in literature however, is what happens to the electrical conductivity and the Seebeck coefficient when the material is shrunk. It should change, but it is not clear if there is always a direct trend. This area should be explored and computationalmethods seem ideal especially because all methods are based on quantum mechanics. But as illustrated, there are practical computational limits to what can be explored. At the moment the computational resources only really exist at national labs. This means that current methods can only be applied to bulk materials, not nanomaterials. Herein, our intension is only to compare the computed

properties of crystalline macro-scale materials with their respective nanoscale forms of thermoelectric properties. This focus is not aiming at designing a computational method to predict electrical conductivity and Seebeck coefficient of nanomaterials. This does not mean though that the future has not been thought of, the software chosen for this computational framework can be used for nanomaterials in the future when the computing hardware has gotten to a point where it can be used for predicting the properties of nanomaterials.

It has been shown that non-linear responses occur when shrinking materials to the nanoscale. For an example, zero-dimension quantum dots change the band structure of the materials as well as change the plasmons, due to quantum confinement[36,37]. It is not clear that a simple approximation can be made for electrical properties for a material like thermal conductivity. Thus, the electrical properties are being studied in this dissertation research, requiring a computational method to rapidly assess the materials electrical properties. It should be stated that a method of computing the thermal conductivity of a material using first principle methods was found, but it was not pursued in any meaningful manner to focus on the most important variables, such as Seebeck coefficient, electrical conductivity, and band structure. The electrical properties are then used to compute the Power Factor, using Eq. 2.2., ZT can be computed for some materials using literature values for thermal conductivity. Thus, in this study, we will develop a computational approach to compute these parameters for metal oxides and our design approach is discussed below – Section IV.2.1.

IV.2.1 Computational Design Approach

The electron properties are computed using Density Functional Theory (DFT) using Quantum ESPRESSO[38] (QE) and Wannier functions using Wannier90[39]. These two software packages were chosen for several reasons. Other software exists that can compute the DFT solutions for periodic systems such as VASP or Abinit. QE was chosen though because it is developed as an open source project, is easy to run in parallel and is being scaled to run on GPUs instead of just CPUs. With a large development team the software project is scaling past more traditional software packages in ways that mean that the software will be around for a long time and there is a strong support community to assist when the software does not work. Wannier90 was chosen for the same reason, the source code was robust and the community was growing. On top of this, the two software packages seamlessly worked together meaning that the output from QE could be fed into Wannie90 and vice versa. The versatility of open source code, functionality, good future growth potential and strong community support were what made these software packages so attractive. The code also with every version was becoming faster and the fact they were open source means that any future code releases can be used without paying for a licenses. These packages were assembled into a method all developed by pouring over the user manuals, published papers from the development teams and the help forums. It was very rare to see anyone wanting to compute the thermoelectric properties of a material meaning this is relatively unique implementation of these software packages. Perhaps, this may be the first demonstration of using combination of these software packages to predict thermoelectric properties of materials.

A generalized method has been developed to compute the thermoelectric (TE) Power Factor (PF) and in some cases the Figure of Merit (ZT). The method created is a computational scheme that uses a material's crystal structure as a starting point and computes all the necessary properties of that material.A schematic diagram for the general method of the computations work that used to compute the band structure, PF and ZT is illustrated in Figure 4.2.

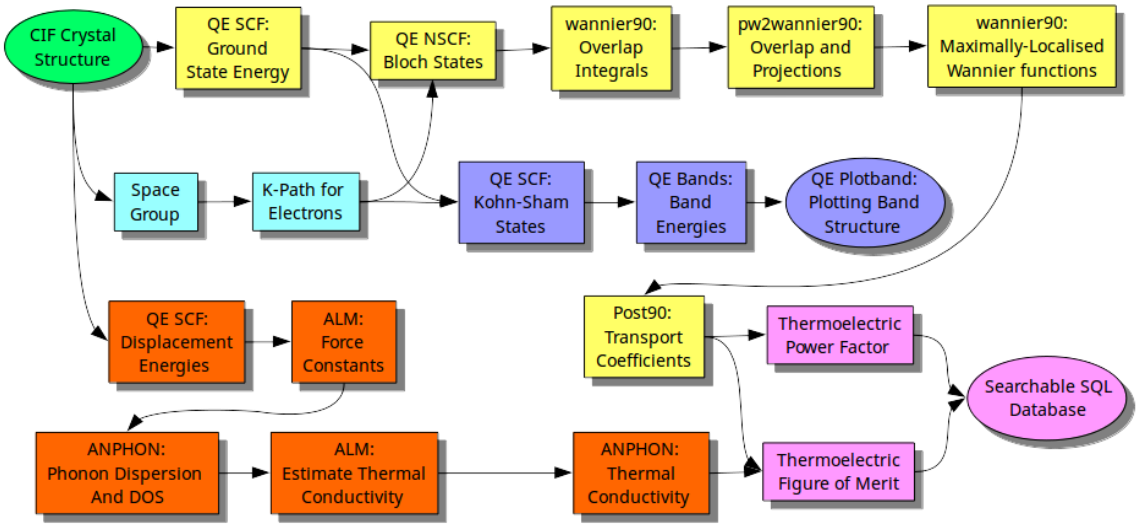

Figure 4.2. Thermoelectric Property Prediction Computational Scheme.

This flow chart shows what was done at each step and what needs to be happen before each step along the desired path toward the results desired. All these steps require that a known crystal structure with a defined unit cell and arrangement of electronics for each atom are known. These steps are well defined computationally as they are all using software that has been developed by teams of software developers for production environments. Each step in this flow diagram uses a user defined input script that defined

the structure of the material at the atomic scale and specifying what the user wants to be computed. The novelty that is being introduced in this dissertation is that the input files can be automatically generated using custom software instead of a user needed to spend hours of time writing them they are generated in seconds. This automation allows for computations to run around the clock requiting very little human involvement in the calculations. The best way of describing the software that has been written for this is what is called a meta-script; a script that generates other scripts to run software. The beginning of this automated procedure to predict thermoelectric properties is knowing the atomic structure of the material. The structure of each material that is to be computed is gathered from literature and can be found in a CIF format from online databases. Examples of such databases include and are not limited to: The Crystallography Open Database and The American Mineralogist Crystal Structure Database. The selected materials that the thermoelectric properties are to be prediction for are chosen based on their constituent elements and those elements that were selected from The USGA survey.

The starting point for all these computations is the materials crystal structure. For a crystalline material, say MnO_2, a well defined unit cell is known from literature. This unit cell can be described using the lengths of the unit cell vectors, the angles between the vectors, the space group, positions of the atoms, the volume and the types of atoms. These unit cell specifics are described in each CIF file for each material from the databases. The computational scheme in Figure 4.1shows that the input to these computations is a CIF file and the thermoelectric properties and band structure can be computed from that structure. A common CIF file reports the location of atoms in the unit

cell using Hermann–Mauguin notation. Quantum ESPRESSO or Wannier90 requires that the atom locations are specified in Cartesian space, to make this conversation open source software called OpenBabel is used. When a CIF file is passed to OpenBabel and the output is specified to XYZ, the format it returns is the Cartesian coordinates for the atoms in that unit cell. Knowing these coordinates enables the input for these computations to be written.

An issue that can occur with a conversion from CIF to Cartesian coordinatesis the introduction of partial occupancy. Crystals, when reported, can have some atoms in different locations, but near each other causing what appears to be an 'overlap' of the atoms. This overlap comes from what is called partial occupancy; there is a probability in nature that atoms are in one place near a mean location. To fix this issue when converting the CIF files to Cartesian coordinates code was written that finds clumped atoms and averages their positions to find a mean position. While separate computations can be done for all the occupancies, this is computationally inefficient; therefore an average atomic position is found and the computations are done on the idealized structure.

From all this so far, the Cartesian coordinates of the atoms are known, the unit cell information is known and the potential partial occupancy of the atoms have been addressed. The last item that is needed to run all the computations is the Brillouin Zone (BZ). The BZ of a unit cell can be found by only knowing its geometry, the specifics of calculating it has been reported by a research group from Duke University in literature[40]. One of their papers has been automated as a script where the unit cell information is

passed to the code and the Brillouin Zone is returned with what are called K-paths.These are necessary to run any of these computations.

With the crystal structure in an idealized form and the unit cell's BZ is known, the computations can commence. As illustrates in Figure 4.2, the CIF structure is the starting point and the end points are the band structure and the SQL database with the PF and ZT of the material. The initial step for all these results is to compute a self consistent solution to find the Hamiltonian of the crystal structure. This is done using Quantum ESPRESSO (QE), a Density Function Theory (DFT) package. The input for QE is based on the crystal structure, types of atoms and there corresponding pseudopotentials, which describe a function that acts as an approximation to the potential function of the electrons around that specific atom[38]. These pseudopotentials are used to calculate the exchange potentials of electrons between atoms in the unit cell and therefore the crystals Hamiltonian. An example input script for QE to compute the Hamiltonian of MnO_2 using what is called an SCF calculation is shown in Appendix A, section A.1.

As shown in Figure 4.2, the band structure can be computed after the SCF calculation, also known as a self-consistent calculation. An input for QE is written that uses the ground state energy computed in the previous step. The input uses the k-paths from the BZ and using QE computes the Kohn-Sham states in the crystal. An example of this input file for MnO_2 is shown in Appendix A, section A.5.This QE is used to compute the band energies and a script for that input is shown in Appendix A, section A.6. The completion of these calculations yields files that can be used to plot the band structure of

the material in K-space. For an example, the band structure computed using the above approach is shown in Figure 4.3 for manganese (II) oxide.

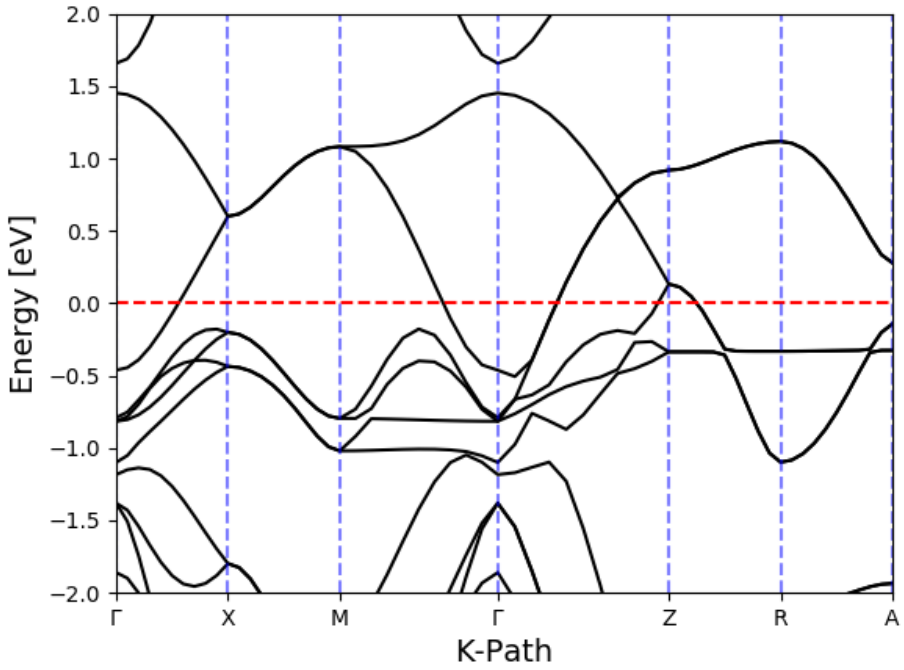

Figure 4.3. MnO_2 Band Structure in K-Space. The Red Line Represents the Fermi Level.

Since the band structure is computed with the Fermi level it can be used to determine if the material is an insulator, semiconductor or conductor. If the Fermi level is in the valance band then it is an insulator. If it is in the band gap, then it is a semiconductor whereif it is in the conduction band then it is a conductor. This is very useful in choosing a thermoelectric material, where semiconductors are the most useful in terms of their properties. Figure 4.3 indicates that the material is most likely an insulator at the Gamma point in the middle. This is because the conduction band is so much higher than the Fermi level, by about 1.5 eV.

In some cases, the band structure of a material predicted using DFT is very different from experimentally measured band. For example GaAs's computed band gap energy is ~1 eV. This is off by ~ 50% from the accepted real value of 1.39 eV. In some cases it might compute that a material is a conductor when in fact it is a semiconductor or vice versa[41]. Another example for this discrepancy is ZnO, which requires a change in method of computations from DFT to DFT+U. The DFT+U is a modified form of DFT where Hubbard potentials are used. The band gap for ZnO computed with DFT is E_g^{DFT} = 0.78 eV and with DFT+U is E_g^{DFT+U} = 3.3 eV. Computing the band structure of the material is only one path in the scheme depicted in Figure 4.2. The properties that are most important to compute is the individual parts of the Power Factor, the electrical conductivity, and Seebeck coefficient. The initial step in computing the Power Factor is the same as the band structure. A self-consistent calculation is done using the crystal structure. When this is done a non-self-consistent calculation (NSCF)can be done using the k-paths generated from the BZ. This computation is done using QE again to compute the Bloch states in the crystal. An example of an NSCF input script for MnO_2 is shown in Appendix A, section A.2.

When the Bloch states and the Hamiltonian are known, the Wannier functions can be computed. This is done by computing the overlap integrals and election state projections using QE and Wannier90 (W90). From those overlap integrals the Wannier functions (WF) can be computed. The electron transport properties can be computed from the WF and can be done with a package called Post90, which computes those properties and outputs the materials Seebeck coefficient, electrical conductivity and electron

thermal conductivity. Most of the steps for computing these properties are redundant, but the input scripts for QE and W90 can be seen in Appendix A, sections A.3 and A.4.

Using Eq. 2.2 for the Power Factor and the output from Post90, the PF can be calculated. The resulting PF is shown computed in three space in which the PF is the response variable, while the two variables it changes are Temperature and Chemical Potential. An example of this plot can be seen in Figure 4.4, the Power Factor of MnO_2.

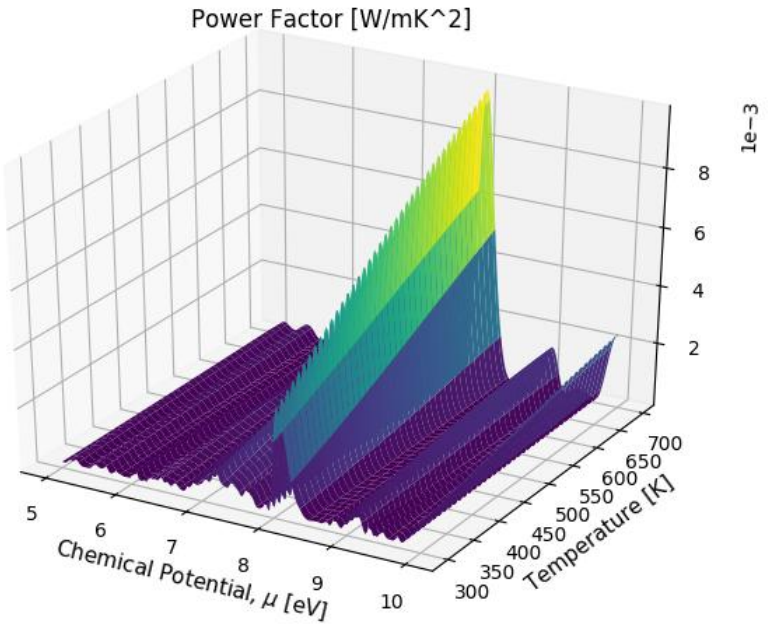

Figure 4.4. Power Factor of MnO_2 with Respect to Chemical Potential and Temperature

These kinds of plots are very informative, as an example they can beused to make material experimentally. If it is predicted that a material will be a good thermoelectric converter, but the results of the experiment are null then it implies that the material needs to be changed in a way that will correspond to a better PF. For example, a poor TE

material can be predicted as a good TE materials from computation with respect to the material's chemical potential. It is shown in literature how this can be done with doping[42]. This simple procedure can turn a bad material into a good one if the desired properties are known to exist in this material according to the computations.

To compute the figure of merit, one more step is needed after the PF calculation. As shown from Eq. 2.1 and Eq. 2.2, the ZT of a thermoelectric material is just PF divided by the thermal conductivity. Thermal conductivity of a material can be computed from the path shown in the Figure 4.1 Using a combination of QE and other software called Alm and Anphon part of the Alamode package. Also, sometimes, it can be found from literature the value for thermal conductivity and divide the PF by that constant value.

IV.3 Theoretical Background for the Computational Engine

Although the computational engine or automation script works, a good understanding of the math behind the computational packages is needed in order to make sure that the solutions that are given make sense to the user. With the support of software developed in the pasta complete theoretical picture is mapped by understanding the physics and math implemented behind the software developed in a collection of literature. The step-wise approach of the computational engine design is described below.

IV.3.1 Approach to Predict Electronic Properties

The initial step in calculating the electron properties is by computing the Hamiltonian of the atomic system built in the unit cell. In a typical method, the Hamiltonian for a crystal lattice with Bloch boundary conditions can be computedusing the Kohn-Sham equation, which calculates a self-consistent solution. This solution is

computed using a non-linear vector space where the solution contains *N* Fourier components and the charge density of the atoms as well as the sum of the Hartree and exchange-correlation potentials. With an initial guess, the Kohn-Sham equation, Eq. 4.1 and Eq. 4.2, is used to compute the energy state of the system.

$$\left(\frac{-\hbar^2}{2m}\nabla^2 + V_{ext}(r) + V^{\text{in}}(r)\right)\psi_i(r) = \varepsilon_i\psi_i(r); Eq.4.1$$

$$V^{(\text{in})}(r) = V_{Hxc}\left[\rho^{(\text{in})}(r)\right];\ Eq.4.2$$

Computing Eq. 4.1 over the unit cell gives a solution to the wave equation. Using that wave equation the charge density can be computed using Eq 4.3.

$$\rho^{\text{out}}(r) = \sum_i |\psi_i(r)|^2\ ; Eq.4.3$$

From Eq. 4.2 and Eq. 4.3, the energy state is computed as well as the Hartree and exchange-correlation energy, Eq. 4.4 and Eq. 4.5 respectfully. The exchange-correlation energy can be calculated because it does not rely on the computed density function.

$$E = \sum_i \int \psi_i^*(r)\left(\frac{-\hbar^2}{2m}\nabla^2 + V_{ext}(r)\right)\psi_i(r)dr + E_{Hxc}\left[\rho^{(\text{out})}\right];\ Eq.4.4$$

$$E' = \sum_i \int \psi_i^*(r)\left(\frac{-\hbar^2}{2m}\nabla^2 + V_{ext}(r) + V^{(\text{in})}\right)\psi_i(r)dr + \int \rho^{(\text{in})}\,V^{(\text{in})}(r) + E_{Hxc} + \left[\rho^{(\text{in})}\right]; Eq.4.5$$

Both energies are used to determine if the calculated energies have converged to a self-constant solution. If the right and left side of Eq. 4.6 are the same (or within a defined error) then the solution is said to be self-consistent.

$$E - E' \simeq \frac{1}{2}\int \frac{\Delta\rho(r)\Delta\rho(r')}{|r - r'|} dr dr' = \frac{1}{2}\int \Delta\rho(r)\Delta V_H(r')\, dr; Eq. 4.6$$

When the self-consistent solution is being solved a generalized eigenvalue problem for all occupied states can be solved as well. These are both described by the Hamiltonian (H) and the overlap matrix (S) in Eq. 4.7.

$$H\psi_i = \varepsilon_i S\psi_i, i = 1, \ldots, N; Eq. 4.7$$

The basis set of eigenvectors must be iterated in a way similar to finding the self-consistent solution. The correction terms added to the basis vector's to compute the solution to this problem is known as correction vectors, defined in Eq. 4.8.

$$\delta\psi_i^{(1)} = Dg_i^{(1)}; Eq. 4.8$$

When the correction vectors are known the Bloch vector's can be computed using Eq. 4.9. These Bloch states are used to compute all other electron properties.

$$\langle k + G|D|k + G'\rangle = \frac{\delta_{GG'}}{\langle k + G|H - \varepsilon S|k + G'\rangle};\ Eq. 4.9$$

These Bloch states describe the wave function of the electrons in a periodic lattice. The Hamiltonian describes the energy states of those waves and the overlap matrix describes how those wave functions overlap[38].

When the Hamiltonian of the crystal lattice, Bloch states, and the wave function overlaps are known, then Maximally Localised Wannier Functions (MLWF) can be computed. Wannier functions are spatially localized functions that describe the electronic structure of periodic materials; in contrast to other methods, Wannier functions relay on band indexes and crystal momentum. These density functions are very useful for nanomaterials as they can be used for different dimensional materials.Their solutions do not depend on the periodicity of the material unlike traditional crystal momentum solutions from Solid State Physics[9]. A typical Wannier function centered on lattice site R can be written as Eq. 4.10.

$$\omega_{nR}(r) = \frac{V}{(2\pi)^2}\int_{\mathrm{BZ}}\left[\sum_m U_{mn}^{(\kappa)}\,\psi_{m\kappa}(r)\right]e^{-i\kappa\cdot R}d\kappa;\ Eq.4.10$$

How the individual Wannier functions are spread spatially can be defined inEq. 4.11.

$$\Omega = \sum_n [\langle\omega_{n0}(r)|r^2|\omega_{n0}(r)\rangle - |\langle\omega_{n0}(r)|r|\omega_{n0}(r)\rangle|^2]\,;Eq.4.11$$

This term can be broken down further into diagonal and off-diagonal Wannier functions, but this form is accurate for a definition. In order to compute Wannier functions from the output of the Density Function Theory, the overlap of the Bloch states,

which is already computed, is needed as well asa starting guess of the Bloch state projections and are defined according in Eq. 4.12 and Eq. 4.13[43].

$$M_{mn}^{(\kappa,b)} = \langle u_{m\kappa} | u_{n\kappa+b} \rangle; Eq. 4.12$$

$$A_{mn}^{(\kappa)} = \langle \psi_{m\kappa} | g_n \rangle; Eq. 4.13$$

When the Wannier functions are known the band velocities are computed from those solutions. This is done using relaxation time approximations. When the velocities are known they can be integrated over the Brillouin zone to find the thermoelectric transport properties of the crystal lattice[43]. When the energies and the velocities of the elections in the crystal lattice are known, a Transport Distribution Function (TDF) can be computed. This takes the form of a tensor and is defined as Eq. 4.14.

$$\sum(\varepsilon) = \frac{1}{V}\sum_{n,\kappa} v_i(n,\kappa) v_j(n,\kappa) \tau(n,\kappa) \delta\left(\varepsilon - E_{n,\kappa}\right); Eq. 4.14$$

The TDF tensor in conjunction with the typical form of the Fermi-Dirac distribution shown in Eq. 4.15 can be used to compute the thermoelectric electron properties. The electrical conductivity, defined in Eq. 4.16, can be used to compute the Seebeck coefficient when Eq. 4.16 is combined with Eq. 4.17. The electron thermal conductivity can be computed using Eq. 4.18. These properties are needed to compute the thermoelectric figure of merit.

$$f(\varepsilon, \mu, T) = \frac{1}{e^{(\varepsilon-\mu)/K_B T} + 1}; \; Eq. 4.15$$

$$[\sigma]_{ij}(\mu,T) = e^2 \int_{-\infty}^{\infty} \left(\frac{-\partial f(\varepsilon,\mu,T)}{\partial \varepsilon}\right) \sum(\varepsilon)\, d\varepsilon; Eq.4.16$$

$$[\sigma S]_{ij}(\mu,T) = \frac{e}{T} \int_{-\infty}^{\infty} \left(\frac{-\partial f(\varepsilon,\mu,T)}{\partial \varepsilon}\right) (\varepsilon-\mu) \sum(\varepsilon)\, d\varepsilon; Eq, 4.17$$

$$[K]_{ij}(\mu,T) = \frac{1}{T} \int_{-\infty}^{\infty} \left(\frac{-\partial f(\varepsilon,\mu,T)}{\partial \varepsilon}\right) (\varepsilon-\mu)^2 \sum(\varepsilon)\, d\varepsilon; Eq.4.18$$

IV.4 Validation of Computational Prediction using Literature

To test the validity of the computations, the computational engine is applied to predict the thermoelectric parameters of a known material and is beingcompared with its experimental values which are already published in the past literature. In this case, the Figure of Merit for PbTe is computed and compared to literature values for bulk crystal of PbTe made from the 1960s. The stepwise approach for testing the computational engine design is described below.

IV.4.1 Method for Testing the Computational Engine Design

Starting with the materials crystal structure, which can be retrieved from the original crystallographic data file, which is in a CIF file format, the procedure described in Section 4.2.1 is used to compute the materials thermoelectric properties. A CIF file from the Open Crystallography Database for PbTe is used for the test computations. The CIF file for PbTe is visualized in Figure 4.5, this crystal structure was rendered using the software package VESTA.

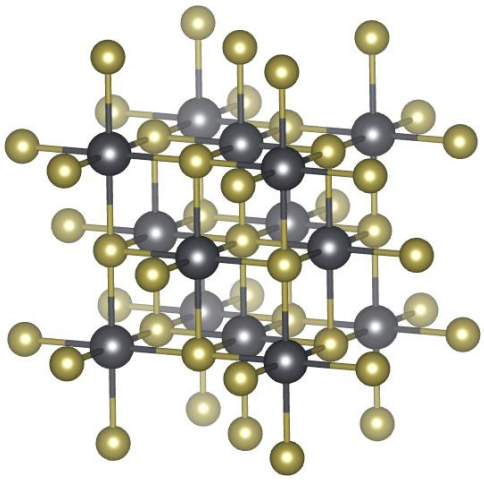

Figure 4.5. PbTe Crystal Structure Rendered using VESTA.

The final output from the computational schema is the electrical conductivity and Seebeck coefficient of PbTe. From this the PF is computed. Using eq. 2, the ZT of the materials is then computed using a literature value of thermal conductivity. As shown from eq. 1 and eq. 2, the ZT of a thermoelectric material is just PF divided by the thermal conductivity. The resulting ZT from the calculations in relation to chemical potential and temperature is shown in Figure 4.6.The ZT of the highest peak in relation to the temperature is shown in Figure 4.7. The maximum ZT for PbTe is ~ 0.7 at 700 K. This is compared to literature where in 1960 similar values for ZT were reported for PbTe. Since then ZT has improved drastically, but the computations match those of the base line. The plots from literature are shown in Figure 4.8[42]. The ZT is plotted in 3 space where the x axis is the chemical potential, the y axis is the temperature and the z axis is the power factor. The ZT of a material depends on its chemical potential; changing it will change

the materials performance from almost useless to very useful. It is shown in literature that changing the chemical potential can be done with doping[44].

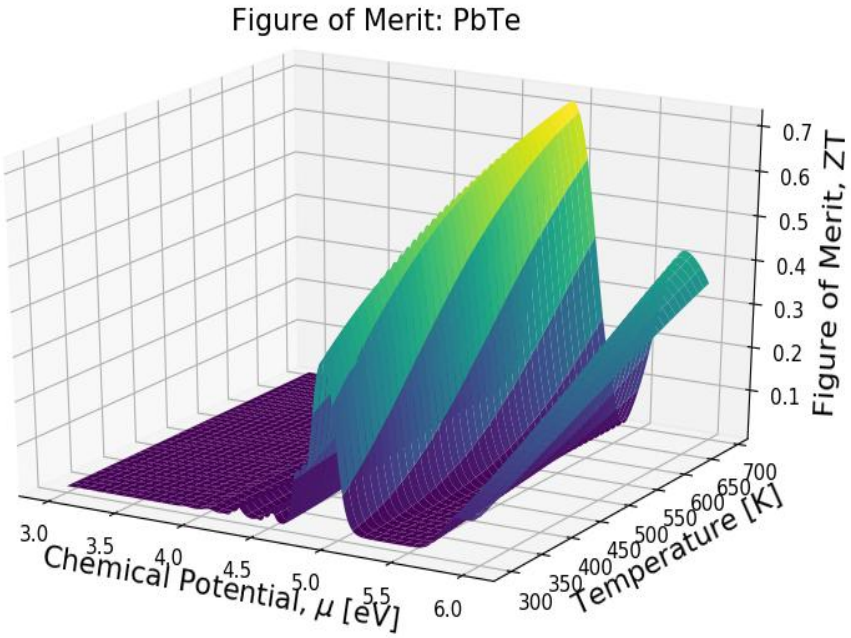

Figure 4.6. PbTe Figure of Merit with Respect to Chemical Potential and Temperature.

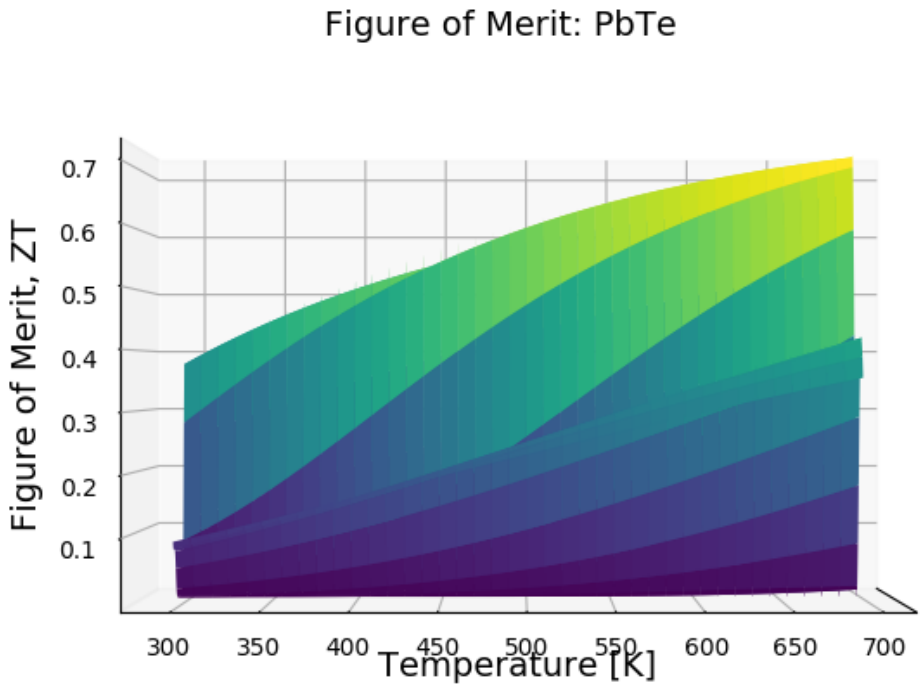

Figure 4.7. PbTe Figure of Merit with Respect to Temperature.

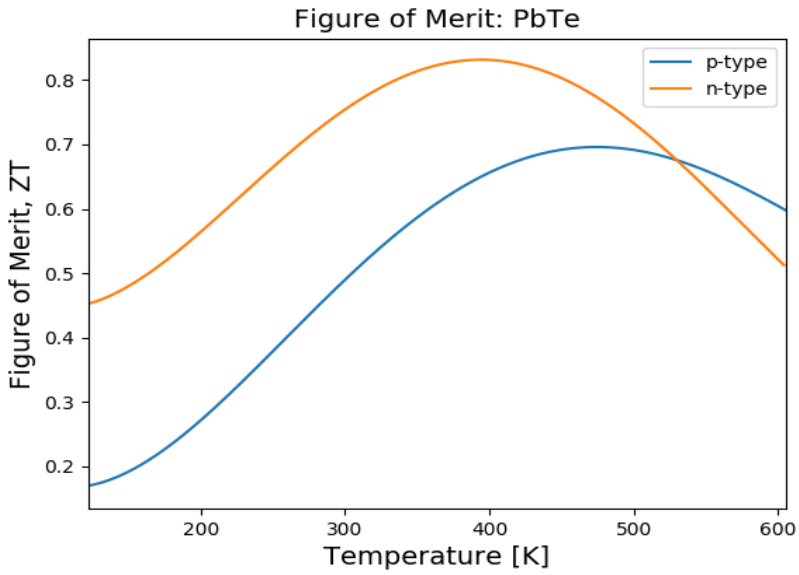

Figure 4.8. Literature PbTe Bulk Figure of Merit from the 1960s.

CHAPTER V

EXPERIMENTAL METHODS

V.1 Materials

The materials used in all the reactions were used as received. N,N-Dimethylformamide (anhydrous, 99.8%), Chromium (III) Chloride Hexahydrate, Strontium Acetateand Manganese (II,III) Oxide was obtained from Sigma-Aldrich chemicals. Ethanol (Reagent Alcohol, 140 Proof), Toluene, Magnesium(II)chloride hexahydrate, Manganese(II) acetate (anhydrous), and Sodium hydroxide pellets were obtained from Fisher Scientific. Copper(II) acetate monohydrate was obtained from Alfa Aesar.

V.2 Characterization

Scanning Electron Microscopy (SEM) was performed using a Zeiss Auriga FIBFESEM and a Hitachi S-4800 FESEM. The typical imaging accelerating voltage was 3 kV with a working distance of 4 mm and 5 kV and a working distance of 5 mm respectively unless otherwise specified. Transmission Electron Microscopy (TEM) was performed using Zeiss Libra 120 TEM. Powder X-Ray Diffraction (XRD) was performed using the Agilent Gemini XRD; a Mo Kα X-ray source was used operating with a voltage and current of 40 kV and 40 mA respectively. FTIR was preformed using a Varian 670-IR. TGA was done using a TA Q500 under a nitrogen atmosphere.

V.3 Procedures for Metal Oxides Nanomaterials Synthesis

V.3.1 Synthesis Procedure for Manganese Oxide Nanostructures

Manganese Oxide nanomaterials were made in a 250 mL round bottom flasks in an oil bath under ambient atmosphere. A total of 12 versions were made with varying solvents and metal precursor to base molar ratios. The solvents used were de-ionized H_2O, 70% EtOH, DMF and Toluene. For each reaction 160 mL of the respective solvent was added to the flask. Manganese acetate (1.20 g) was dissolved in de-ionized water (10.0 mL) and added to the reaction flask. Sodium hydroxide (NaOH) pellets with the respective weight were dissolved in de-ionized water (10 mL) and was added dropwise at a rate of 10 mL/min to the reaction flask and stirred for another 5 min. The molar ratio of the precursor to NaOH was maintained at 1:5, 1:10 and 1:15. The weights used for each reaction with each solvent and base molar ratio are shown in Table 5.1. After stirring 5 min at room temperature, the stir-bar was removed, and the flask was put in a non-heated oil bath at room temperature. Before heating the bath boiling stones were added to the flask to prevent bumping. The flask was then gradually heated to 80 °C and left for 24 hours at 80 °C. Then the reaction flask was allowed to cool down to room temperature over a period of several hours. The colloidal solution was transferred into centrifuge tubes and centrifuged at a rate of 10,000 rpm for 10 minutes, decanted the liquid, and washed the product with de-ionized water. The washing step was repeated several times and the final product collected in this manner was freeze dried at 0.140 mBar at -50 °C for 24 hours resulting in a dry brown-black powder.

Table 5.1. Precursor and Base Amounts used for the Preparation of Manganese Oxide Nanoparticles.

Molar Ratio M^{+n}: Base	Solvent type/water	Manganese Acetate mass (g)	Sodium Hydroxide mass (g)
1:5	Water	1.20	0.98
	70% Ethanol	1.20	0.98
	DMF	1.20	0.98
	Toluene	1.20	0.98
1:10	Water	1.20	1.96
	70% Ethanol	1.20	1.96
	DMF	1.20	1.96
	Toluene	1.20	1.96
1:15	Water	1.20	2.94
	70% Ethanol	1.20	2.94
	DMF	1.20	2.94
	Toluene	1.20	2.94

V.3.2 Synthesis Procedure for Magnesium Hydroxide Nanostructures

The synthesis procedure and reaction conditionswere very similar to the preparation of manganese oxide nanoparticles. In a typical procedure, magnesium hydroxide nanomaterials were made frommagnesium chloride. The amounts of precursor and the base used for each reaction with respect to each solvent type and base molar ratio are shown in Table 5.2. The final product collected afterfreeze dried at 0.140 mBar at -50 °C for 24 hours resulted a dry white powder.

Table 5.2. Precursor and Base Amounts used for the Preparation of Magnesium Hydroxide Nanoparticles.

Molar Ratio M^{+n}: Base	Solvent type/water	Magnesium Chloride (g)	Sodium Hydroxide mass (g)
1:5	Water	1.20	2.52
	70% Ethanol	1.20	2.52
	DMF	1.20	2.52
	Toluene	1.20	2.52
1:10	Water	1.20	5.04
	70% Ethanol	1.20	5.04
	DMF	1.20	5.04
	Toluene	1.20	5.04
1:15	Water	1.20	7.56
	70% Ethanol	1.20	7.56
	DMF	1.20	7.56
	Toluene	1.20	7.56

V.3.3 Synthesis Procedure for Copper Oxide Nanostructures

Following the similar procedure as in the preparation of manganese oxide nanostructures, copper oxide nanostructures were made from copper acetate.The final product collected was freeze dried at 0.140 mBar at -50 °C for 24 hours to obtain copper oxide nanostructures in black powder form. The amounts of precursor and the base used for each reaction with respect to each solvent type and base molar ratio are shown in Table 5.3.

Table 5.3. Precursor and Base Amounts used for the Preparation of Copper Oxide Nanoparticles.

Molar Ratio M^{+n}: Base	Solvent type/water	Copper Acetate mass (g)	Sodium Hydroxide mass (g)
1:5	Water	1.20	1.11
	70% Ethanol	1.20	1.11
	DMF	1.20	1.11
	Toluene	1.20	1.11
1:10	Water	1.20	2.22
	70% Ethanol	1.20	2.22
	DMF	1.20	2.22
	Toluene	1.20	2.22
1:15	Water	1.20	3.33
	70% Ethanol	1.20	3.33
	DMF	1.20	3.33
	Toluene	1.20	3.33

V.3.4 Synthesis Procedure for Chromium Oxide Nanostructures

Following the similar procedure as in the preparation of manganese oxide nanostructures, chromium oxide nanostructures were made from chromium chloride. The final product collected was freeze dried at 0.140 mBar at -50 °C for 24 hours to obtain chromium oxide nanostructures in green powder. The amounts of precursor and the base used for each reaction with respect to each solvent type and base molar ratio are shown in Table 5.4.

Table 5.4. Precursor and Base Amounts used for the Preparation of Chromium Oxide Nanoparticles.

Molar Ratio M^{+n}: Base	Solvent type/water	Chromium Chloride (g)	Sodium Hydroxide mass (g)
1:5	Water	1.20	0.90
	70% Ethanol	1.20	0.90
	DMF	1.20	0.90
	Toluene	1.20	0.90
1:10	Water	1.20	1.80
	70% Ethanol	1.20	1.80
	DMF	1.20	1.80
	Toluene	1.20	1.80
1:15	Water	1.20	2.70
	70% Ethanol	1.20	2.70
	DMF	1.20	2.70
	Toluene	1.20	2.70

V.3.5 Synthesis Procedure for Strontium Oxide Nanostructures

Following the similar procedure as in the preparation of manganese oxide nanostructures, strontium oxide nanostructures were made from strontium acetate. The final product collected was freeze dried at 0.140 mBar at -50 °C for 24 hours to obtain strontium oxide nanostructures in white and very light flaky powder. The amounts of precursor and the base used for each reaction with respect to each solvent type and base molar ratio are shown in Table 5.5.

Table 5.5. Precursor and Base Amounts used for the Preparation of Strontium Oxide Nanoparticles.

Molar Ratio M^{+n}: Base	Solvent type/water	Strontium Acetate (g)	Sodium Hydroxide mass (g)
1:5	Water	1.20	1.17
	70% Ethanol	1.20	1.17
	DMF	1.20	1.17
	Toluene	1.20	1.17
1:10	Water	1.20	2.34
	70% Ethanol	1.20	2.34
	DMF	1.20	2.34
	Toluene	1.20	2.34
1:15	Water	1.20	3.50
	70% Ethanol	1.20	3.50
	DMF	1.20	3.50
	Toluene	1.20	3.50

V.4 General Method for Sample Preparation for Characterization

All SEM samples were prepared by sonicating the nanomaterial powder in de-ionized water and then drop casting the solution onto a silicon wafer with the exception of Strontium Oxide which was drop cast onto copper tape. All SEM samples were sputtered coated using 5 nm Gold/Palladium to ground the sample. The TEM samples were prepared by dropping the solution of the sample onto a TEM grid coated with Formvar and left to air dry before imaging. The powder XRD was performed by suspending the powder on a glass fiber using vacuum grease. All TGA and FTIR was done on dry powder with no other sample preparation.

V.5 Temperature Dependent Electrical and Thermoelectric Properties Characterization Method

V.5.1 Background of Strategy Development

Thermoelectric materials produce an electrical potential when a thermal gradient is applied to it. The performance of that material as an energy converter is measured by the Figure of Merit, notated as ZT, shown in Eq. 5.1. To compute this metric three material properties are required: the electrical conductivity (σ), Seebeck coefficient (S) and the thermal conductivity (κ).

$$ZT = \frac{\sigma S^2}{\kappa} T; \text{Eq. } 5.1$$

Another measure of thermoelectric performance is the Power Factor (PF), shown in Eq. 5.2, while simulator to ZT, it only measures the power output of the material as a metric of area and temperature.

$$PF = \sigma S^2; \text{Eq. } 5.2$$

The fundamental difference between ZT and PF is the exclusion of thermal conductivity from PF. Because of this, a material can have a high PF and a low ZT of vice versa; no definitive statement can be made that a material with a high PF is a good thermoelectric material. The typical method that thermoelectric materials are made is taking a power and pressing into in to a bulk block and measuring its properties[22]. These blocks are also used when building the final devices as well which is why a bulk block is measured.It is known from literature that as the average powder diameter drops the

thermal conductivity drops. This happens due to phonon modes in the bulk crystal being frozen out forcing more thermal energy to be redistributed through the electron gas. Because our bulk blocks are made from a nano powder instead of a powder with a diameter in the micrometer range we know the thermal conductivity has dropped, but it is not clear what happens to the electrical properties. This means the denominator of ZT is 'known' as in it is known what happens as the dimensionally of the material drops. What needs exploring is if both the Seebeck coefficient and electrical conductivity increases or decreases; therefore only the PF needs examination.

All thermoelectric material properties have a temperature dependent aspect to them; as the materials temperatures change the properties change as well. This means that a proper evaluation of these materials requires that the properties need to be evaluated at different temperatures. This constraint would force a rewrite of both Eq. 5.1 and Eq. 5.2; Eq. 5.3 and Eq. 5.4 respectively.

$$\mathrm{ZT} = \frac{\sigma(\mathrm{T})\mathrm{S}(\mathrm{T})^2}{\kappa(\mathrm{T})}\mathrm{T};\ \mathrm{Eq.}\ 5.3$$

$$\mathrm{PF} = \sigma(\mathrm{T})\mathrm{S}(\mathrm{T})^2;\ \mathrm{Eq.}\ 5.4$$

To measure the temperature dependent PF, a custom apparatus was constructed and used to measure the properties of a bulk block made from nanopowder. All mathematics, computations and methods to compute the properties are show in the following sup-chapters.

V.5.2 Measurement Method Development and Mathematics

Fundamentally two electrical properties are being measured: electrical conductivity and the Seebeck coefficient. Both of these properties need to be measured at different temperatures. To do this a custom system has been built using a mixture of 3D printing hardware, a Keithley 2400 source meter and a modified hand press. A schematic of the apparatus is displayed in Figure 5.1.

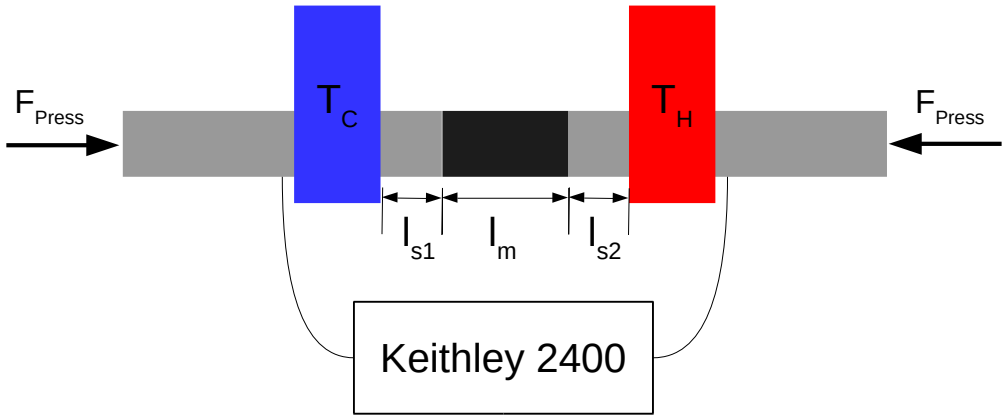

Figure 5.1. A Schematic Diagram for the Temperature Dependent Thermoelectric Property Measurement System.

The blue and red blocks are heating elements that are interdependently contorted using modified 3D printing hardware and control software. A thermocouple is embedded in each heating block and the operating temperature is set using a software interface. The software is used to maintain the temperature of the block dynamically. The dark part with a length of l_m is the material that the temperature dependent properties are being measured. The other beams are made from steel and were chosen because steel is both a good electrical and thermal conductor. The system of three parts is held together using a

hand press that exerts 650 pounds of force from both ends. Electrical leads are hooked up to steel and fed to a Keithley 2400 source meter to accuracy measure the electrical properties. A photo of the assembly is shown in Figure 5.2.

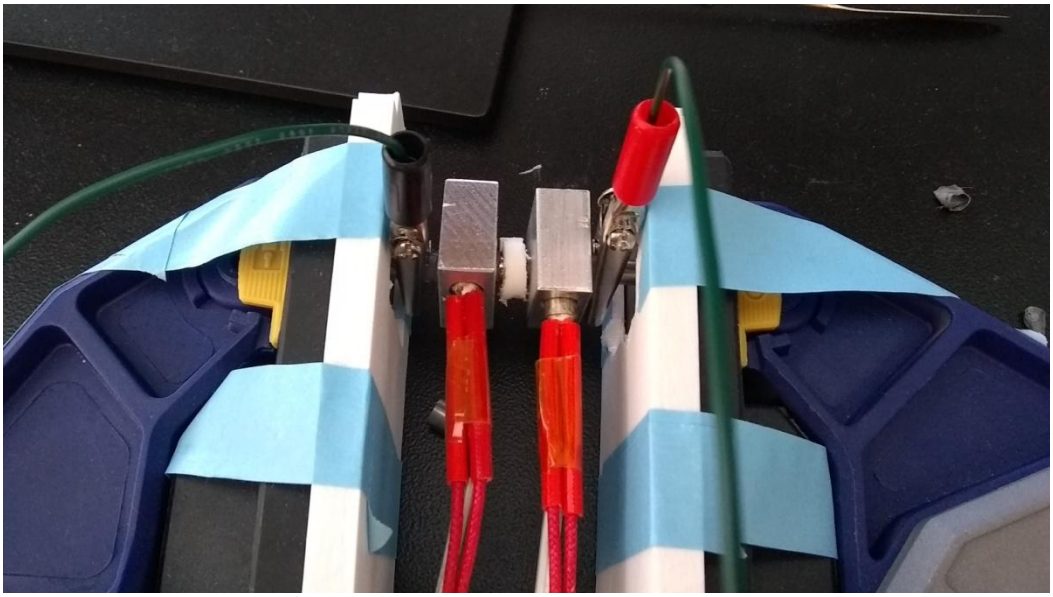

Figure 5.2. An Image of the Thermoelectric Property Measurement Assembly. The White Disk is the Pellet Inside a 3D Printed PLA Container, the Metal Blocks are the Heating Elements and the Wires Run to the Keithley 2400.

This apparatus is also used for making pellets from nanoparticles. A 3D printed cylinder made from PLA has a steel rod inserted into one end and back filled with a nano powder. The other side of the cylinder has another steel rod inserted and it is then pressed with ~ 500 MPa of pressure. This is held for 10 minutes while both heating elements are tuned to 100 C to make a solid pellet, but still maintaining the integrity of the nanoparticles. After heating the pellet, it is cooled and the measurement temperature ramp begins. The first property measured is electrical resistance from which the

conductivity can be computed. The sample is then cooled again and the temperature is ramped again to measure the Seebeck coefficient. The temperatures used for each measurement are displayed in Table 5.6.

Table 5.6 Thermoelectric Property Measurement Temperatures.

Measurement Temperatures		
Cold [C]	Mean [C]	Hot [C]
20	30	40
30	40	50
40	50	60
50	60	70
60	70	80
70	80	90
80	90	100
90	100	110

The mean temperature is the temperature that the properties are being measured at. To measure electrical conductivity both sides of the pellet are heated to the mean temperature ensuring that no thermal gradient is created and a uniform measurement temperature is used. The hot and cold values are the values set for the Seebeck coefficient; this is to induce a temperature gradient of 20 C to induce a electrical potential in the material for measurement. How each set of properties are measured and computed are broken down in each of the following sections.

V.5.3 Electrical Conductivity

To measure the temperature dependent electrical conductivity both heating elements are set to the mean temperature, as an example both sides are set to 30 C and the conductivity is measured and then the temperature is changed to 40 C so on and so forth. The conductivity is computed by measuring an I-V curve. This is done using a Keithley

2400 is a source meter where it applies a sweeping voltage and measures the resulting current in the circuit. The I-V curve for a typical sample is show in Figure 5.3.

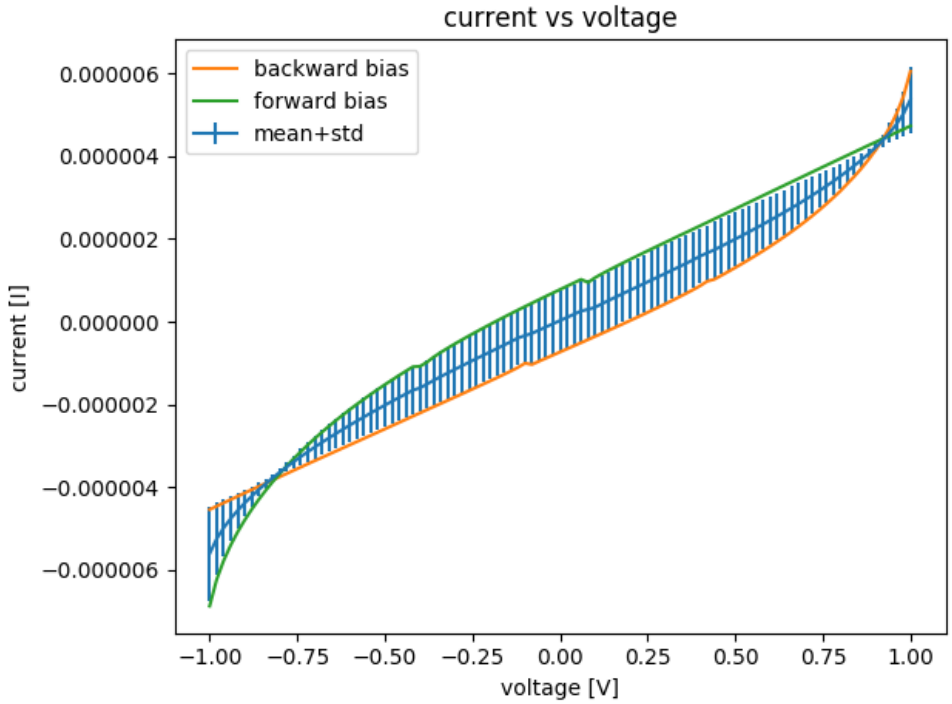

Figure 5.3. I-V Curve of Sample with Forward and Backward Bias Sweep.

In the figure, the green line is a forward bias measurement of current. This means the voltage started at -1 V and sweeped to +1 V. As can be seen the trigger in the system over biased the measurement in the current meaning the measurement was shifted. To compensate for this a backwards bias sweep is done from +1 V to -1 V shown as the orange line. The two curves are averaged, shown as the blue line with the computed standard deviation. Several forward and backward sweeps are done so there are enough measurements to do proper statistics on the data. This is done at every temperature where both sides of the pellet are at the mean temperature. A best fit line is then fit to the

average line to find the inverse of resistance. To compute the error in the slope of the best fit line the standard deviation is added and subtracted to the mean line and best fit lines are computed for that. From these fits the resistance of the pellet can be computed as well as its error.

To calculate the resistance of the material, the slope of the I-V curve is needed. This is computed as well as with its error using Eq. 5.5, Eq. 5.6 and Eq. 5.7. Using Eq. 5.6, the error in the best fit line can be computed knowing Eq. 5.7.

$$I = mV + b, b \equiv 0, m = \frac{\Delta I}{\Delta V}; \text{Eq. } 5.5$$

$$m_{min} = \frac{\Delta I - \delta I}{\Delta V}, m_{max} = \frac{\Delta I + \delta I}{\Delta V}; \text{Eq. } 5.6$$

$$\delta m = \frac{m_{max} - m_{min}}{2}; \text{Eq. } 5.7$$

Ohm's Law dictates that the inverse of the slope is the resistance of the material, shown in Eq. 5.8.

$$R \pm \delta R = \frac{1}{m \pm \delta m}, \delta R = \frac{\delta m}{m}|m|; \text{Eq. } 5.8$$

Knowing the resistance and the dimensions of the pellet, the electrical resistivity of the pellet with error can be calculated as shown in Eq. 5.9 and Eq. 5.10. To calculate the resistance the area of the pellet and length need to be calculated as well with each term explicitly calculated using Eq. 5.11 and Eq. 5.12.

$$\rho + \delta\rho = \frac{(R \pm \delta R)(A \pm \delta A)}{(l + \delta l)}; \text{Eq. } 5.9$$

$$\delta\rho = \sqrt{\left(\frac{\delta R}{R}\right)^2 + \left(\frac{\delta A}{A}\right)^2 + \left(\frac{\sqrt{\delta l_{tot}^2 + \delta l_{s1}^2 + \delta l_{s2}^2}|l|}{l}\right)^2}\ |\rho|; \text{Eq. } 5.10$$

$$A \pm \delta A = \pi(r \pm \delta r)^2, \delta A = 2\frac{\delta r}{r}|A|; \text{Eq. } 5.11$$

$$l \pm \delta l = (l_{tot} \pm \delta l_{tot}) - (l_{s1} \pm \delta l_{s1}) - (l_{s2} \pm \delta l_{s2}), \delta l = \sqrt{\delta l_{tot}^2 + \delta l_{s1}^2 + \delta l_{s2}^2}|l|; \text{Eq. } 5.12$$

Using the resistivity from Eq. 5.9, the electrical conductivity of the pellet can be calculated using Eq. 5.13.

$$\sigma \pm \delta\sigma = \frac{1}{\rho \pm \delta\rho}, \delta\sigma = \frac{\delta\rho}{\rho}|\sigma|; \text{ Eq. } 5.13$$

These equations are applied to every average I-V curve for each temperature. The result is a set of values for resistance; resistivity and conductivity as well as their associated error computed using proper differential error propagation.

V.5.4 Seebeck Coefficient

The Seebeck coefficient of a material is defined as the induced electrical potential per unit temperature difference across the material as shown in Eq. 5.14.

$$S = -\frac{\Delta V}{\Delta T}; \text{Eq. } 5.14$$

This means that to measure the Seebeck coefficient of a material a temperature difference needs to be applied across the material and the induced potential need to be

measured. To do this the same setup is used as shown in Figure 5.1 and the heaters are set at different temperatures. The average temperature needs to be the same as the resistance plot so the mean points are chosen and the temperature difference is expanded around the mean temperature. A temperature difference of 20 °C is chosen because of environmental constrains, therefore 10 °C is added and subtracted from the mean temperature. The hot and cold side temperature values of the material are listed in Table 5.6.

The choice of a $\Delta T = 20$ °C does not mean that the temperature difference across the material is 20 °C; this means that the difference between the two heating elements is 20 °C. The temperature gradient not only acts across the material but also over the steel rods between the heating elements. To compute the actual temperature difference across the material a set of thermal diffusion equations is used. A 3D model was built that resembles the setup of the temperature dependent electrical tester. It takes the same form of the system in Figure 5.1. The thermal diffusion equations were computed across a tensor for the 3D system, a voxel rendering of that tensor and the device is shown in Figure 5.4. As can be seem in the figure, the red and blue slabs represent the heating elements, one acting as the heat sink (the blue) and the other acting as the heat source (the red). The teal section represents the pellet of material that is being investigated and the salmon pink are the metal rods. The open area is treated as air. To run these computations the simplest form of the thermal diffusion equation is used in three dimensions shown in Eq. 5.15.

$$\frac{\partial T}{\partial t} = \alpha\left(\frac{\partial^2 T}{\partial x^2} + \frac{\partial^2 T}{\partial y^2} + \frac{\partial^2 T}{\partial z^2}\right); Eq.\ 5.15$$

The alpha term is the thermal diffusivity which is specific to different materials and changes how heat propagates in that material. A tensor of all those diffusion constants was created for fast matrix multiplication in to run the simulation. The air was also used in the calculation as well to see how the heat dispersed from the rod of material. Neumann boundary conditions were used on the edges of the tensor to update those boundary values.

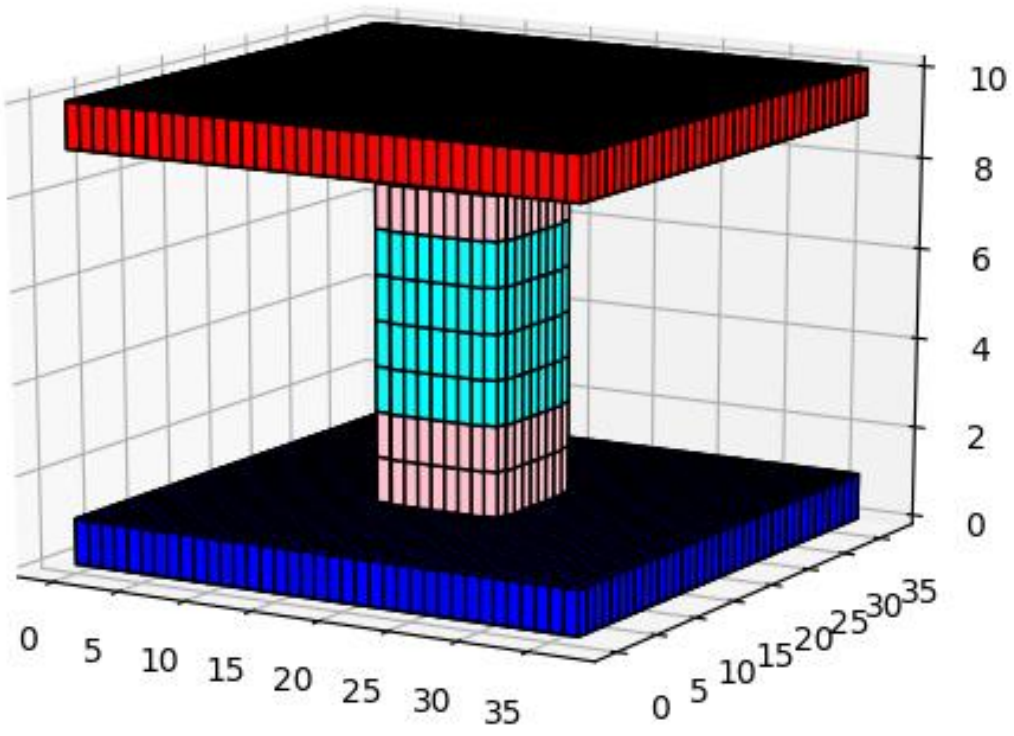

Figure 5.4. Voxel Rendering of Thermoelectric Measurement System for Thermal Diffusion Equation Simulation.

The thermal diffusion simulation would run and a contour plot was used to determine when that system of equations came into equilibrium. A cross section of that simulation running and the overlapped contour plot can be seen in Figure 5.5, and the final equilibrium state in Figure 5.6.

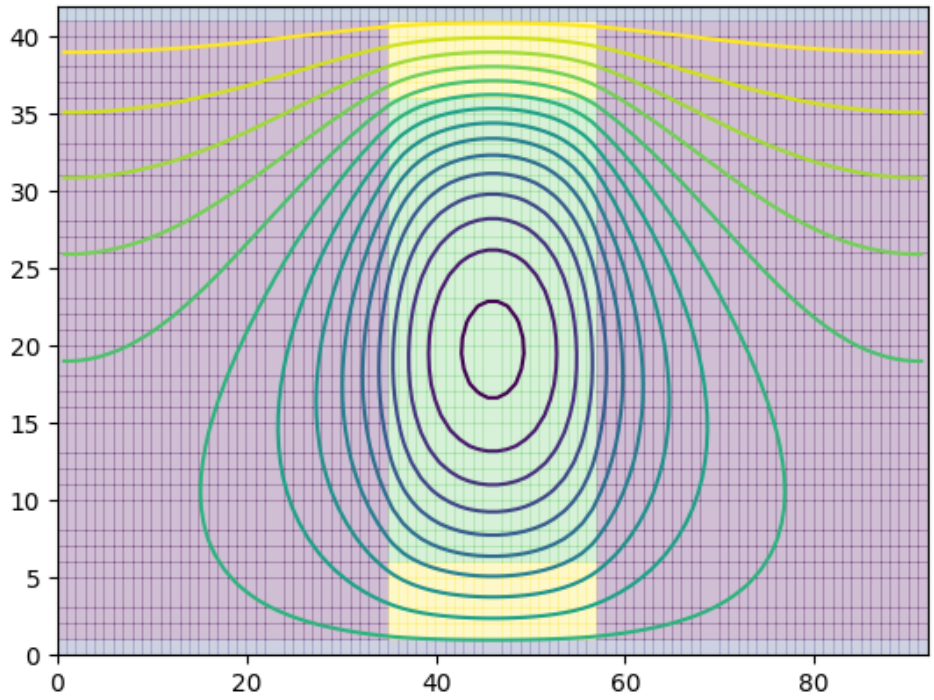

Figure 5.5. Cross Section of Thermal Diffusion Simulation Running.

The final solution is a linear temperature gradient through the material. This model can be extrapolated into a simple linear model using a linear slope; from this model the temperature difference across the material can be calculated knowing the dimensionality of the materials and the temperature of the boundary conditions. The linear model can is shown in Figure 5.7.

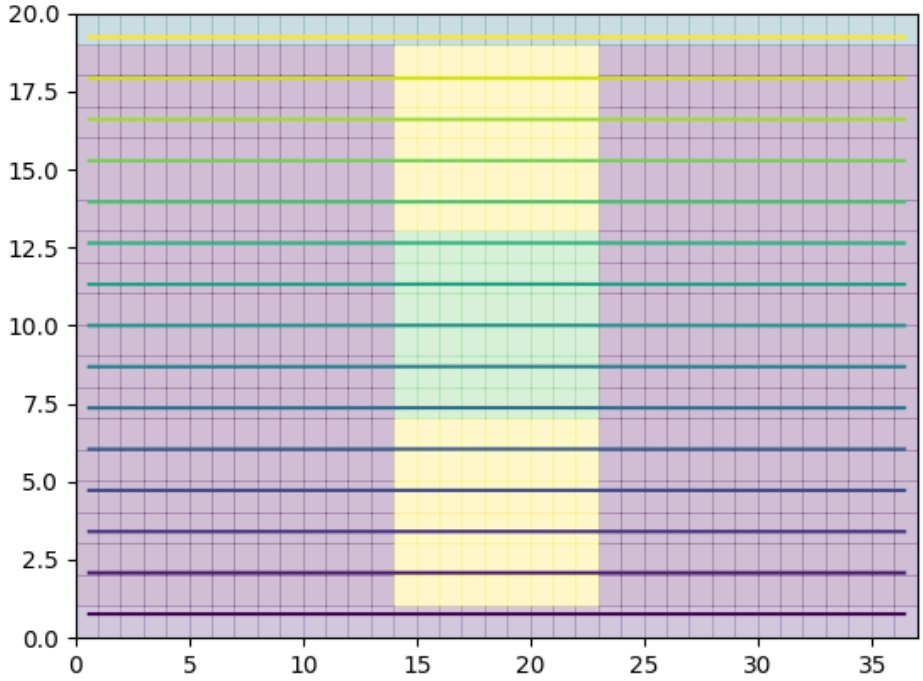

Figure 5.6. Cross Section of Thermal Diffusion Simulation at Equilibrium.

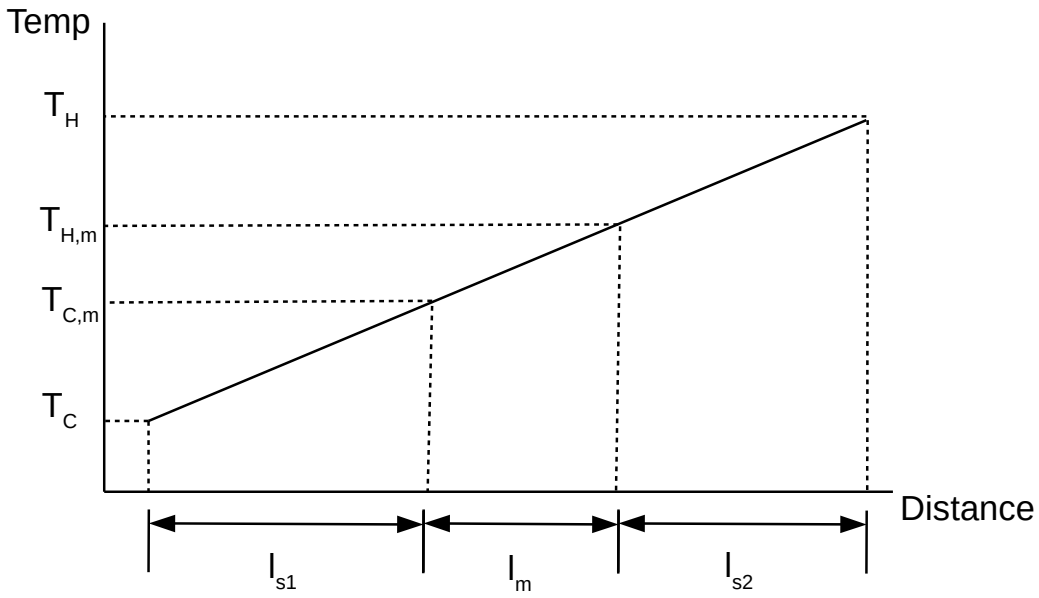

Figure 5.7. Linear Equilibrium Temperature Gradient across the Material and Steel Between the Heating Elements of the Testing Apparatus.

The boundaries of the model are such that the sum of the length l_{s1}, l_{s2} and l_m is the length between the two heating elements shown in Figure 5.1.The way the length of the material is measured is by having the pellet of nanoparticles held in between the steel rods and the total length measured; knowing the length of each steel rod allows for the thickness of the nanoparticle pellet to me calculated. With this information the temperature difference across the material can be computed. The temperature difference is required to compute the Seebeck coefficient of the material. As shown in Eq. 5.16, the temperature term is now well defined from this model using the linear model that is mathematically shown in Eq. 5.17. This equation was derived knowing the slope of the line from the model shown in Figure 6.6 and finding the linear equation based on known measurements.

$$S = -\frac{\Delta V}{\Delta T}, \Delta T = T_{H,m} - T_{C,m}; \text{Eq. } 5.16$$

$$T = \frac{T_H - T_C}{l_m + l_{s1} + l_{s2}} D + T_C \rightarrow \Delta T = \frac{T_H - T_C}{l_m + l_{s1} + l_{s2}} l_m; \text{Eq. } 5.17$$

With the capacity of computing the temperature difference established, the next step is measuring the induced voltage from the temperature difference. There are at least two ways this can be done, first the electrical probes as illustrated in Figure 5.1 can be hooked up to a voltage meter and the voltage recorded. This method presents an issue though as the induced voltage of a material from the Seebeck coefficient is typically in the micro volt range. Measuring such a voltage is very hard; it requires a set of very expensive and accurate instruments that lock in to the electrical signal and make sure the

signal is above the measurement noise. One method attempted to get around this was passing the input feeds to a differential amplifier and checking for a shift in the DC offset of the signal out of the amplifier. This method resulted in a wide variety of measurements that were not repeatable; this was a result of the amplifier introducing too much noise into the signal as well as measurement issues associated with the Keithley 2400 involving current limits from the input signal that was output from the amplifier.

The solution to this issue is measuring the induced current instead of measuring the voltage. When the material is connected to the source meter and a temperature difference is applied to the material, the material acts as a potential and current source in a Kirchhoff loop. The resistor in the circuit is the inertial resistor of the meter. The current source has an internal resistance as well as all current sources do; fortunately the internal resistance of the current source is known, it was computed when the conductivity of the pellet was measured. The most simple circuit diagram of this Kirchhoff loop is shown in Figure 5.8 and a more comprehensive one is shown with a thermal potential source in Figure 5.9.

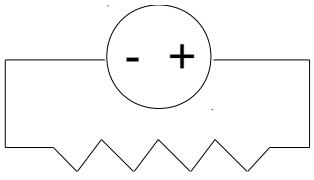

Figure 5.8. Simple Kirchhoff Loop Illustration

These figures show a potential source, but potential sources are effectively current sources with an internal resistance. It is much easier to measure micro amp instead of

micro volts and the internal resistance has already been measured. Knowing both of these allows for the induced voltage to be computed using Ohm's law.

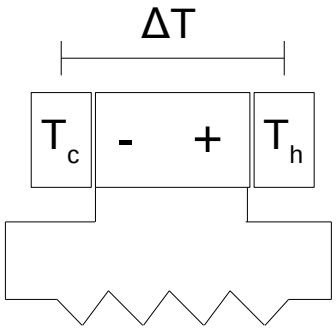

Figure 5.9. Thermal Potential Source from Thermoelectric Source in a Kirchhoff Loop.

Measuring the induced current in this manner and combining it with the already known resistance of the pellet the electrical potential can be computed. Knowing the dimensions of the setup and the temperature difference and having a linear temperature model enables the calculation of the temperature difference across the material. With these two values and using Eq. 5.16, the Seebeck coefficient of the material can be calculated for each mean temperature that the temperature difference is expanded around.

V.5.5 Standard Material Measurement and Method Validation

This method was developed and validated in a recursive manner. Two know materials were tested to make sure that the proper Seebeck coefficient could be measured. A 9999 pure block of Molybdenum and Nickel were used as two unique materials for testing. Literature values for these materials are known and a 9999 purity sample will be the best for testing. These samples used are used for PVD e-beam sputtering sources, the only issue that would be faced is the fact the surface would oxidize in atmosphere. Other

then oxidation these samples are pure. Figure 5.10 shows the metal pellet mounded in the device measurement system.

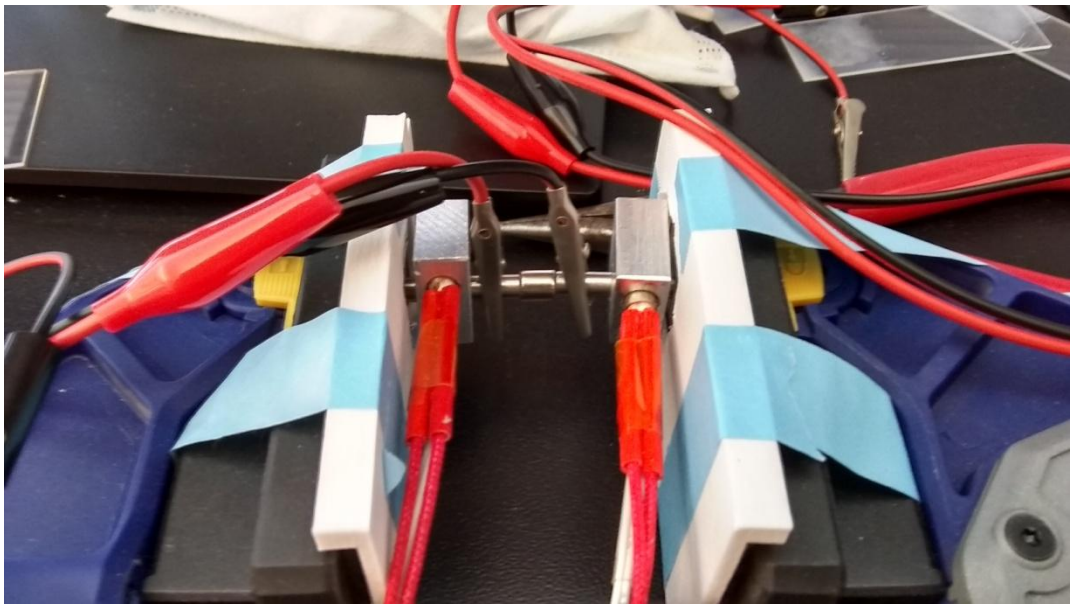

Figure 5.10. 9999 Pure Metal Mounted in Measurement System to Test Standard Material.

Using the temperature dependent method described in the last section, the electrical conductivity and Seebeck coefficient of Mo and Ni were measured. The electrical conductivity of Mo and Ni in units of S/mm are shown in Figure 5.11 and Figure 5.12 respectively.

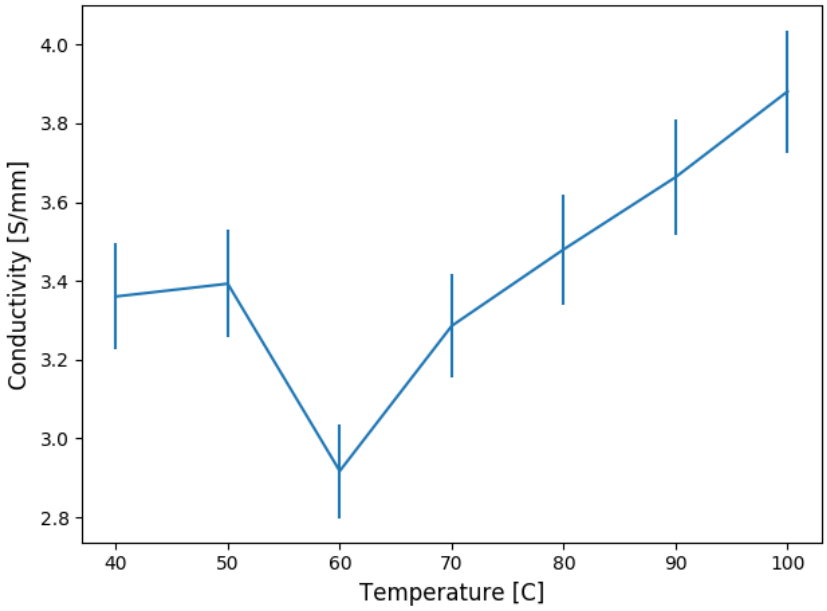

Figure 5.11. Electrical Conductivity of Molybdenum with Respect to Temperature.

The value for both Mo and Ni at 40 C are low for the conductivity, most metals are much more conductive. While this was an early concern it is believed that it is purely the oxide on the surface of the metal that caused this drop in the conductivity as well as interface binding between the metal pellet and the steel rods in the measurement apparatus; there was no binding agent, only pressure holding the system together.

The Seebeck coefficient on the other hand was clearly in the correct range compared to literature unlike the conductivity. The reported value for the Seebeck coefficient of Mo = 5.6 µV/K and Ni = -19.5 µV/K[45]. The measured Seebeck coefficients for Mo and Ni are shown in Figure 5.13 and Figure 5.14 respectively.

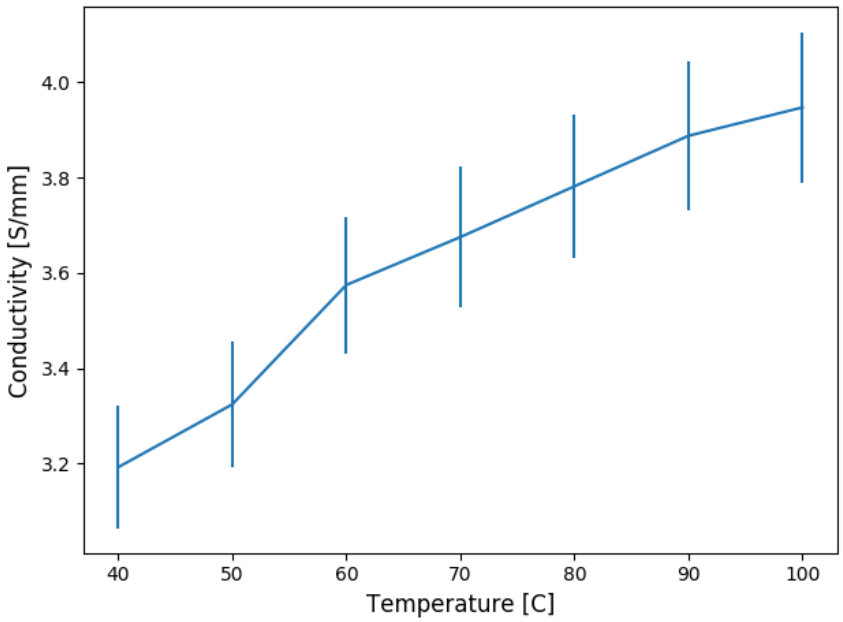

Figure 5.12. Electrical Conductivity of Nickel with Respect to Temperature.

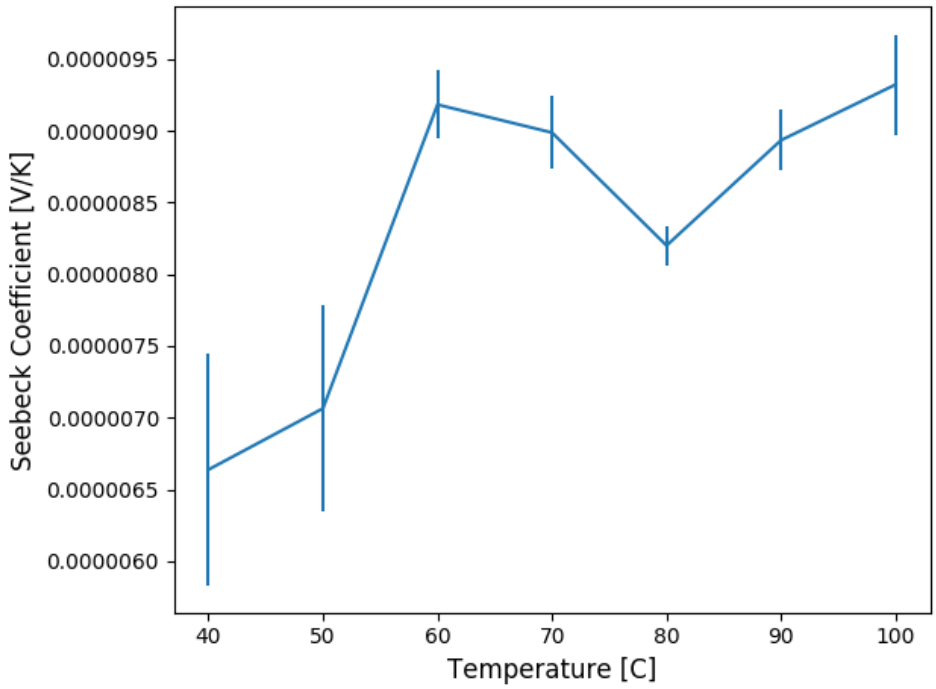

Figure 5.13. Seebeck Coefficient of Molybdenum with Respect to Temperature.

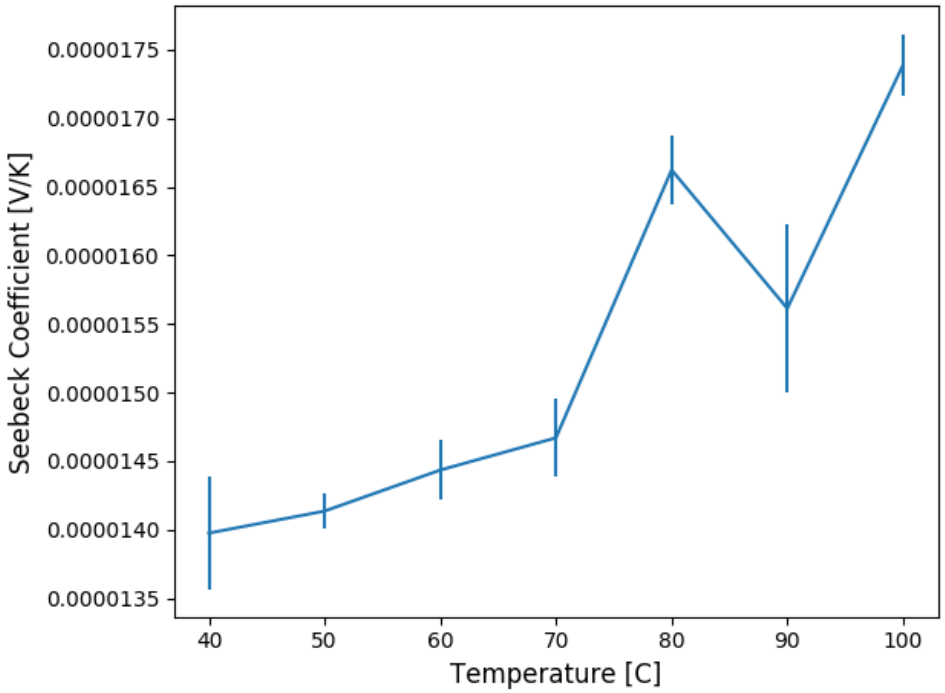

Figure 5.14. Seebeck Coefficient of Nickel with Respect to Temperature.

The literature values for the Seebeck coefficients are very close to what was measured for both materials with one important distinction. The measured value for Nickel was positive and not negative. This appears to be the result of the wiring polarity of the source meter. While the sign is not correct it is in the correct magnitude range. Based on these results the method appears to work at measuring the correct Seebeck coefficient. When the nanomaterials are analyzed literature will be used to assign the proper sign to the Seebeck coefficient.

CHAPTER VI

SOL-GEL SYNTHESIS OF METAL OXIDE NANOSTRUCTURES

VI.1 Metal Oxide Nanostructures and their Synthesis Methods

Metal oxides play a decisive role in both research and industrial applications in the areas of chemistry, material science and physics[46]. Owing to their thermal stability and optical properties, metal oxides have been widely used as heterogeneous catalysts in industry and in other sectors because of their thermal stability and optical properties[47,48]. Regardless of these existing applications, interest in metal oxides has been growing recently due to future potential uses including better catalysts, sensors, electronics applications, and energy conversion devices, including fuel cells and thermoelectric generators[49–51]. Over the past decades a wide range of oxides have been researched and used; those include MgO, Al_2O_3, PbO, TiO_2, MoO_2, and V_2O_5 among others[49].

Their properties can be drastically changed or enhanced by nanostructuring them.This has been the main target of research for years. Nanostructuring a material, not just metal oxides, into different morphologies and sizes impacts that materials plasmon, band structure, band gap, electrical conductivity, thermal conductivity and thermal stability[10,36,52]. Nanomaterials with such tunable properties make them attractive as these propertiesenhance their usefulness in potentials applications[49]. For an example, nanostructured Vanadium Dioxide has been shown to lead to a break down in the

Wiedemann-Franz law where the electrical conductivity is related linearly to the electron contribution to thermal conductivity[23].

A variety of synthesis methods that have been investigated to make nano-scale metal oxides, including chemical vapor deposition (CVD), electrochemical, electrospinning, hydrothermal and sol-gel synthesis[49]. For nanostructured metal oxides to be used at an industrial scale, the synthesis methods need to be highly scalable. However, among current preparation methods, there are very few methods have shown the scalability needed for industrial production. The reasons vary from high capital investment to operational costs. In the case of CVD, the high temperatures required make it cost prohibitive for large scale synthesis. The wet-chemical synthesis methods have been promising as alternatives for low-cost and large-scale preparations. Among the wet-chemical synthesis methods, sol-gel synthesis processes areoptimized for the variables of cost and yield. Sol-gel synthesis was used as far back as the mid 20th century to make silicon oxide particles[53]. During the 1980s sol-gel was used in the fabrication of ceramics and since then it has moved into the realm of making metal oxide structures[49,54]. This synthesis method to produce ceramics is far eco-friendlier than traditional methods. Sol-gel reactions happen at atmospheric pressure, and low temperature, resulting high yield and low production costs. Lots of work has been done over the past two decades to make these reactions more robust by addressing common sustainability issues[49,55]. Metal oxides have been made using several different methods, but non-aqueous methods have shown to be highly desirable because it offers the control over the morphology. The reactions

usually can take place in water with variety of metal precursors with a variety of different counter anions[56].

A typical sol-gel synthesis method involved a two step process with two phases: sol and gel phase. The sol part of this reaction is a colloidal suspension of nanocrystals in a solution medium and the gel is an interconnected network of solid particles that form from a liquid phase. The combination of these two processes enables the formation of nanocrystals followed by self-assemble into a microstructure as a gel[53,57,58]. The application of these reactions enables the preparation of powders, fibbers, thin films, xerogens, and aerogels[54]. There are two distinct ways in literature that sol-gel reaction has performed;aqueous and non-hydrolytic methods. Aqueous methods involve hydrolysis and condensation of metal alkoxides in water. This process is limited though due to its reaction kinetics when using different metals to make mixed metal oxide nanomaterials. Non-hydrolytic methods have issues with applicability to a large set of metals[59–63]. These issues are addressed with a new sol-gel synthesis path that recently developed by our group[21].

In this dissertation work, five unique metal oxides/hydroxides were made using a novel sol-gel method. The metal oxide nanostructures are derivatives of manganese oxide, copper oxide, magnesium hydroxide, chromium oxide, and strontium oxide. These five materials with different morphologies have been explored extensively in literature, and prepared using different synthesis paths.The sol-gel synthesis method augmented to make the above five metal oxide derivatives isan aqueous-based hydrolysis followed by

self-assembly using organic-based solvents, yielding a high degree of control in size and shape.

The chemistry of the sol-gel method used to make metal oxide nanostructures is depicted in Figure 6.1.

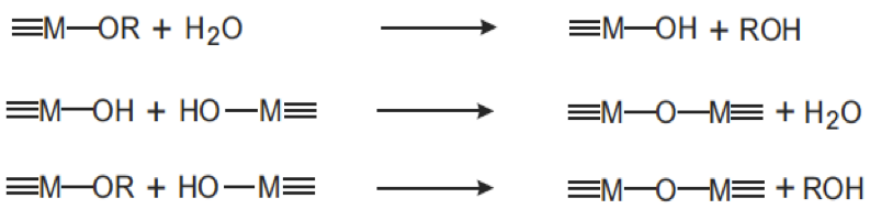

Figure 6.1. Sol-gel Metal Oxide Reaction Scheme[21].

A solvent and base catalyst study is preformed to see the impact on self assembly of nanocrystals formed during the sol phase of the reaction into a larger structure with a unique morphology. The morphology and crystal structure of these materials are investigated for all solvents and base concentrations.

VI.2 Manganese Oxide

The Manganese Oxide nanoparticle synthesized using our sol-gel method has the stoichiometry Mn_3O_4 with a hexagonal morphology. Considerable work has been reported in literature showing different methods of making this type of Manganese Oxide as nanoparticles for various applications. Mn_3O_4 has been shown to be useful in reducing carbon monoxide and methane as well as the combustion of organic compounds[64,65]. It has also been used as an electrode in lithium-ion batteries[66,67]. One of the biggest issues facing Manganese Oxide is a good method of producing the material for these

applications beyond traditional methods. The reported forms of Mn_3O_4 morphologies and synthesis methods reported in literature include, but are not limited to: 42 nm nanoparticles square like particles synthesized using thermal evaporation methods, 15-20 nm particles made suing ultrasonic-assisted synthesis, 20 nm rice shaped particles make using vigorous stirring and left to age, 14 nm particles made using a similar sol-gel procedure and rods 100 nm in diameter and several micros in length made using a hydrothermal method[68–72]. Tie-Zhen showed that hexagonal plates can be formed using a hydrothermal method with an average diameter of 5 nm [14]. While this morphological shape matches those created using the sol-gel method presented, their reported stoichiometry was a mixture of Mn_3O_5 and α-Mn_2O_3, not Mn_3O_4[73].

The Manganese Oxide nanoparticles synthesized using out sol-gel method stand in contrast to the rest of literature. To the best of the author's knowledge, this is the first time a hexagonal Mn_3O_4 nanoparticle can be synthesized using a sol-gel method, especially at this size repeatedly. The general synthesis procedure, described in Chapter 5, was used to make Manganese Oxide nanoparticles. The resulting sizes and shapes of each particle from each synthesis pathway are detailed in Table 6.1.

Table 6.1. Manganese Oxide Nanoparticles Experimental Conditions and Morphologies.

Molar Ratio M^{+n}: Base	Solvent type/water	Morphology (dimension/nm)
1:5	Water	Hexagonal nanoparticles (130 ± 40)
	70% Ethanol	Hexagonal nanoparticles (135 ± 32)
	DMF	Nanoribbons and nanoparticles (N/A)
	Toluene	Hexagonal nanoparticles (130 ± 40)
1:10	Water	Hexagonal nanoparticles (118 ± 50)
	70% Ethanol	Hexagonal nanoparticles (135 ± 32)
	DMF	Nanoparticles (51± 21)
	Toluene	Hexagonal nanoparticles (117 ± 34)
1:15	Water	Hexagonal nanoparticles (73 ± 36)
	70% Ethanol	Hexagonal nanoparticles (152 ± 50)
	DMF	Aggregated particles in gel form
	Toluene	Hexagonal nanoparticles (165 ± 53)

Using the synthesis procedure from chapter 5, two distinct morphologies were created: hexagonal and particle like. All solvents with the exception of DMF created hexagonal plates; the DMF produced the particles. Measurements of the particles were made for their diameter from one tip to another; on average the hexagonal particles have a diameter around 130 nm and the particles having an average diameter around 40 nm. All particles were imaged using SEM and TEM. The micrographs for all solvents with a 1:5, 1:10 and 1:15 molar ratio are shown in Figure 6.2, 6.3 and 6.4 respectively. It is clear from both the SEM and TEM that Water, Ethanol and Toluene made distinct hexagonal plates and the DMF made particles that aggregated during the sample

preparation process. It is clear from the TEM that while there is a general form of the plates being formed, the nanocrystals faces do not align perfectly during gelatin during the sol-get synthesis; the transparency of the particles make is clear that while there is an order, it is not in an since, single crystal.

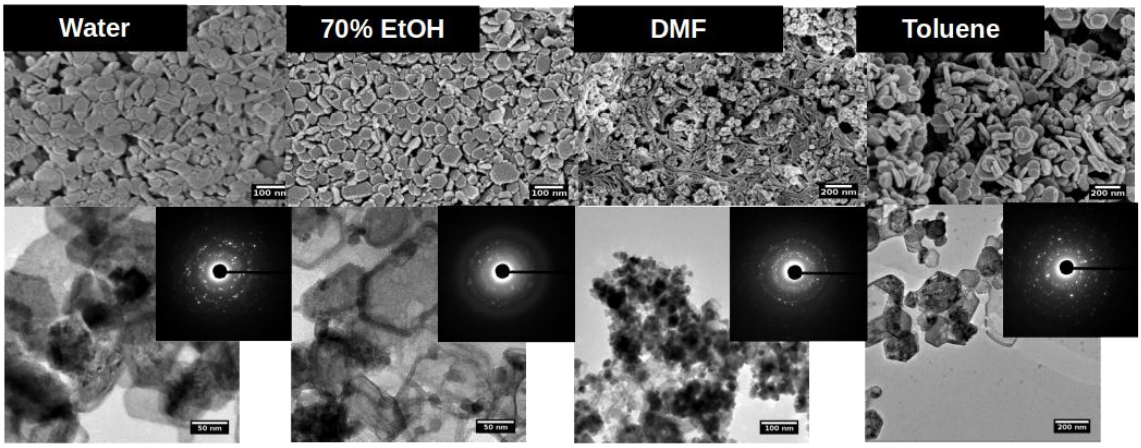

Figure 6.2. SEM and TEM Micrographs of Manganese Oxide.

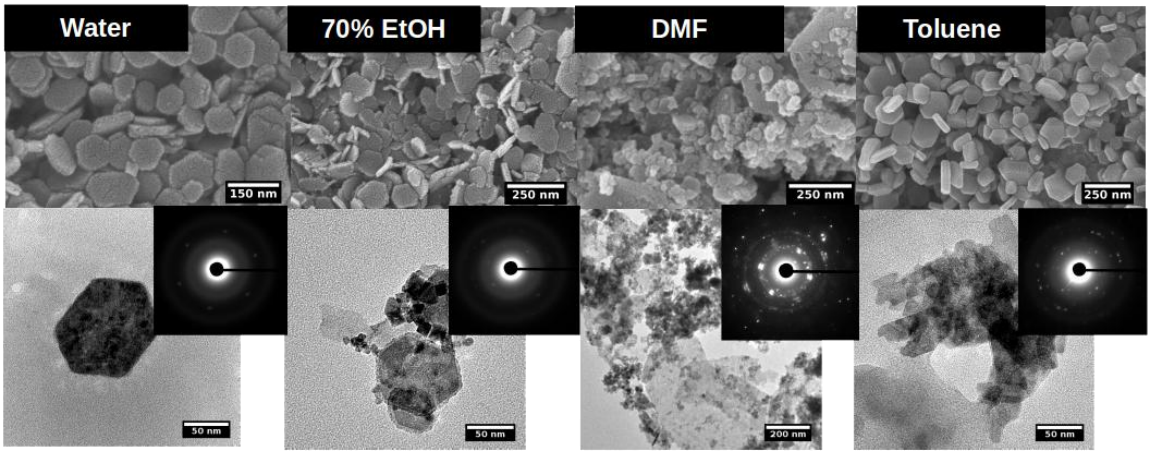

Figure 6.3. Manganese Oxide Micrographs of Particles with a 1:10 Base Ratio.

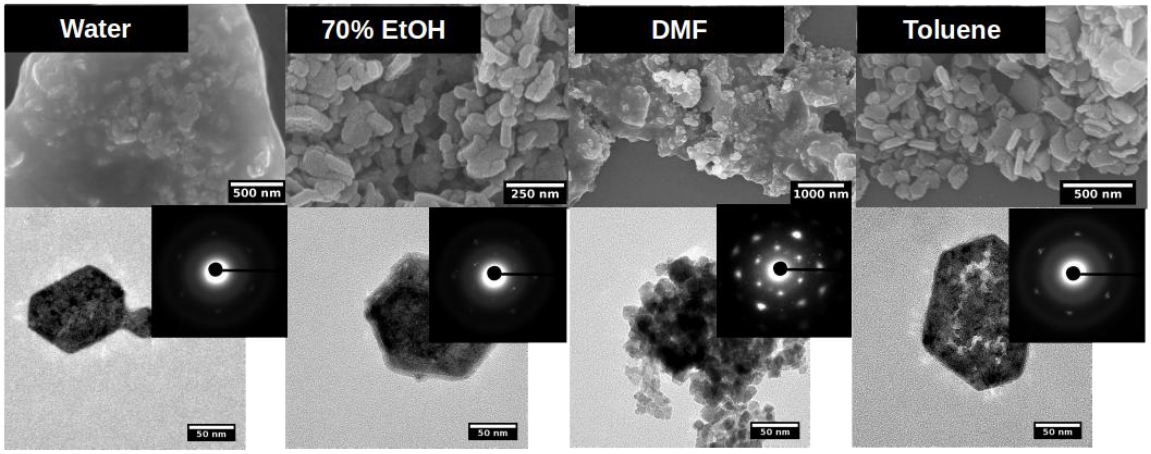

6.4. Manganese Oxide Micrographs of Particles with a 1:15 Base Ratio.

TEM diffraction was performed on the particles while imaging using TEM. From the SEAD patterns, there does appear to be more of a diffraction pattern for both the 1:5 and 1:15 molar ratio particles compared to the 1:10. This indicates that a more polycrystalline material, if desired, can be synthesized using a 1:10 molar ratio. To further investigate the crystal structure of the nanoparticles, XRD was done on all particles. The diffraction patterns for the 1:5, 1:10 and 1:15 molar ratio can be seen in Figure 6.5, 6.6 and 6.7 respectively. The particle formation seen in the SEM and TEM become clearer when these diffraction patterns are examined; the patterns for Water, Ethanol and Toluene are all virtually identical. The DMF on the other hand sticks out as an exception showing that the [112], [013] and [211] faces are more prone for nanocrystals alignment when forming the particles. While the faces of the nanocrystals grow along might change, the crystal structure of the material does not change depending on the solvent or the base concentration. Using the Crystallography Open Database (COD), a known crystal structure of Manganese Oxide was found and its theoretical

XRD pattern was computed using VESTA. It can be seen in the XRD figures the overlay of that computational pattern. The identified crystal structure using this pattern overlay is Mn_3O_4 which is has a triclinic space group. This structure can be accessed from COD using the ID number: 1011262.

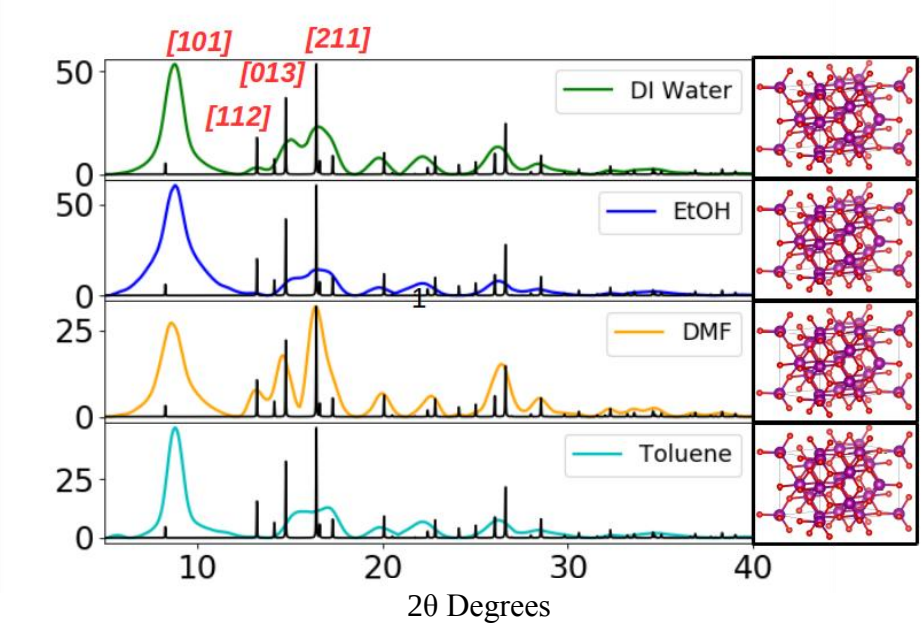

Figure 6.5. Mn_3O_4 XRD with Computational XRD Overlays and Crystal Unit Cell Rending Generated using VESTA. Crystal Structure COD ID: 1011262.

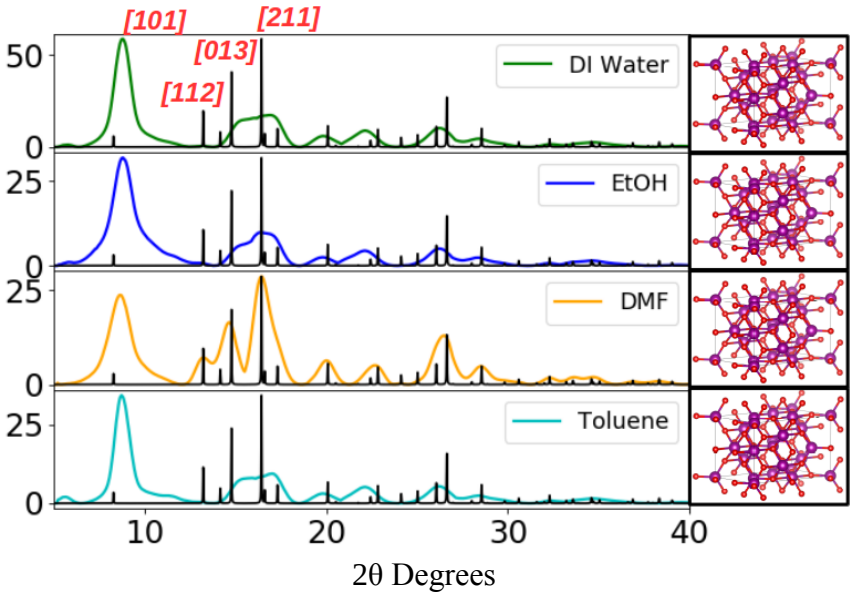

Figure 6.6. Mn_3O_4 XRD with Computational XRD Overlays and Crystal Unit Cell Rending Generated using VESTA. Crystal Structure COD ID: 1011262.

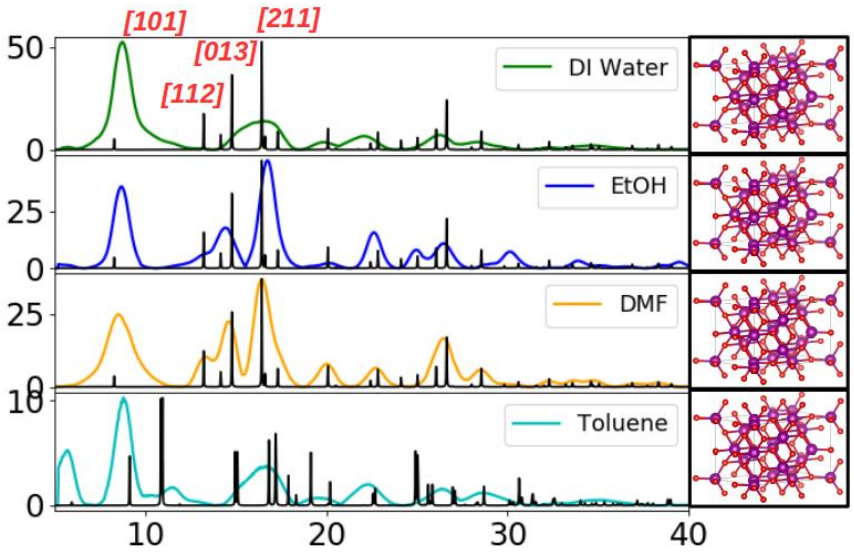

Figure 6.7. Mn_3O_4 XRD with Computational XRD Overlays and Crystal Unit Cell Rending Generated using VESTA. Crystal Structure COD ID: 1011262.

Manganese Oxide was chosen as the material to run a full characterization of its thermoelectric properties on. Using the procedure outlines in chapter 5, a pellet of these particles needs to be made requiring further analysis of the particles thermally and how temperature impacts the crystal structure. Because the crystal structure of the particles were all the same, the most green and simple synthesis was used to make the Manganese Oxide using water as the solvent with a 1:5 base molar ratio. All nanoparticles used for the thermoelectric analysis used particles made using these parameters.

Looking at the XRD, it is clear that the intensity of some of the peaks are not lining up as expected using the computational XRD. This is due to the crystal growth faces during the sol-gel synthesis. It was also shown using TEM that the material is somewhat polycrystalline. To make sure that the best possible crystal structure exists for the thermoelectric measurements the particles were annealed in atmosphere to see if the crystal packing would improve. Two batches of Nanoplates were heated to 300 °C and 550 °C respectively for 1 hour each. XRD was then done on the samples to see if the crystal packing improved. Those XRD patterns are shown in Figure 6.8.

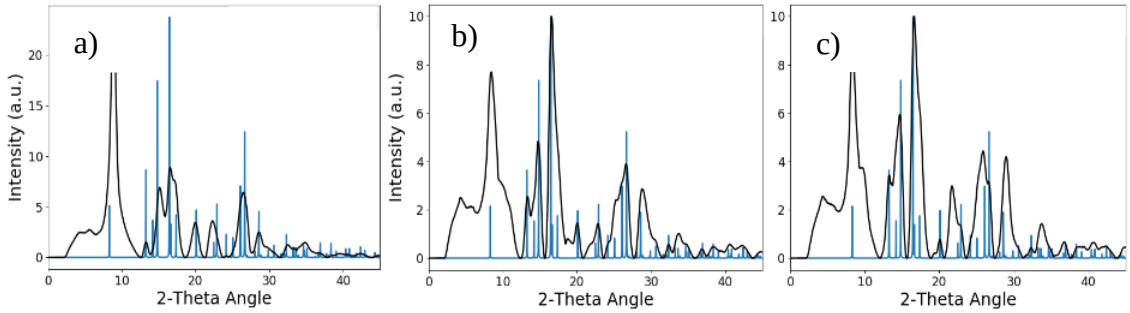

Figure 6.8. a) XRD of Mn_3O_4 Nanoplates at Room Temperature, b) XRD of Mn_3O_4 Nanoplates Annealed at 300 °C for 1 Hour, c) XRD of Mn_3O_4 Nanoplates Annealed at 550 °C for 1 Hour.

Post processing the Nanoplates using annealing clearly increasesthe particles crystallinity. As the temperature increases the respective peaks show a stronger correlation to the single crystal computational structure. It is clear from the data that a more crystalline material can be produced from the sol-gel process with a simple post processing procedure. To make sure that the material is thermally stable Thermal Gravimetric Analysis (TGA) is run to show where the plates are stable up to and if the temperature dependent thermoelectric electron properties can be measured with confidence. The TGA is run using a platinum pan in a nitrogen atmosphere. The TGA of the sample is shown in Figure 6.9.

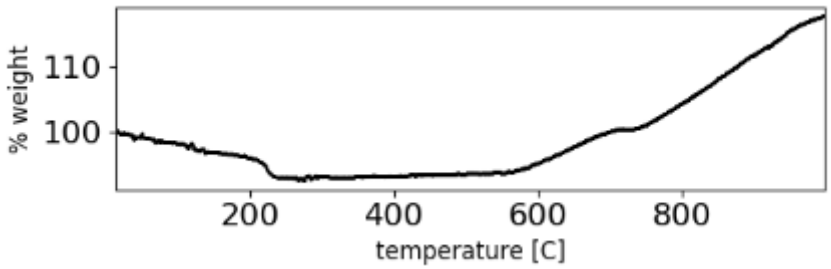

Figure 6.9. TGA of Mn_3O_4 Nanoplates under Nitrogen Atmosphere using a Platinum Pan.

The TGA clearly indicates a fall off in mass up to about 220 ºC. This is most likely left over acetate groups that integrated into the Nanoplates during the gelatin phase using the sol-gel synthesis as well as OH groups as well that can form on the surface. The rise in the mass after approximately 550 ºC is credited to the Manganese Oxide catalyzing a break down in the nitrogen atmosphere and forming a Manganese Nitride[74]. As a confirmation that the initial mass fall off is due to the proposed groups, FTIR is used on the pre-annealed Nanoplates which shows clear peaks that correspond to OH groups, CO group and Manganese CO group. The existence of these groups confirms the hypothesis that there are some organic components that can be burned away during annealing either with a furnace or a TGA. The FTIR is shown in Figure 6.10.

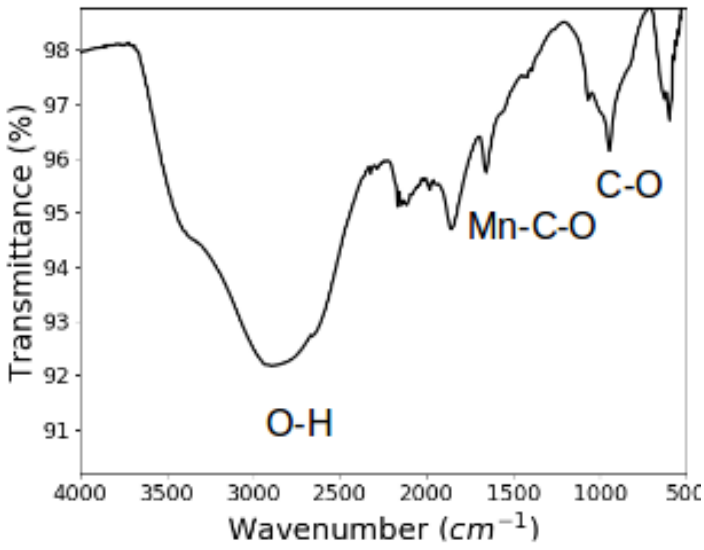

Figure 6.10. FITR on Pre-Annealed Mn_3O_4 Nanoplates.

VI.3 Copper Oxide

The Copper Oxide nanomaterials made using the developed sol-gel method all had the stoichiometry of CuO, but have a varied morphology based on the solvent used. These reactions used Copper Acetate as a precursor. One of the biggest reasons Copper Oxide is used for application is its inherent p-type semiconducting nature. Synthesis's such as electrocatalytic methods have been used to produce Copper Oxide nanomaterials with morphologies including microspheres, nanosheets and nanowires[75]. Methods in literature show that a wide variety of morphologies can be produced with varying sol-gel techniques including: nanowires[76,77], nanoflowers[78–80], nanorods[81–83], nanobelts[76] and nanoparticles[81,83] to name a few.

While there are varied methods to produce Copper Oxide, the primary one found in literature was sol-gel. Topnani showed that both Cu_2O and CuO nanoparticles with a

diameter of 31 nm and 32 nm respectively can be made using sol-gel[84]. Similar results areshown by Kayani[85]. Other nanoparticles were produced using a wet syntheses method under nitrogen and high temperature producing nanoparticles with a diameter ranging from 3.6 nm to 10.7 nm[86]. Jisen reported nanorods with a length of about 200 nm[81]. Other morphologies were reported by Ananth using both wet and hydrothermal methods include rice grain-like structures, needles and plate like structures[87].

Using the synthesis method described in chapter 5, it is shown that in general two different morphologies can be created that vary in size. The shape and morphology are shown in Table 6.2. Either very large thin sheets in the micrometer range were created during the synthesis process or rice/rod like particles around 25 nm were formed. All materials were imaged using SEM and TEM for morphological analysis. The micrographs for all materials made in all four solvents at a 1:5, 1:10 and 1:15 molar ratio are shown in Figure 6.11, 6.12 and 6.13 respectively.

What is clear from the SEM analysis is that with water and toluene large sheets of CuO were made at all base concentrations, but TEM shows that the water produces a better packing of the nanocrystals as there is less transmission in the micrographs. The ethanol produced rice like rods at a 1:5 and 1:10 molar ratio, but at 1:15 more of a clumpy agglomeration with no clear morphology, yet still crystalline according to the SEAD pattern. The DMF produced small rod like morphologies at all three base concentrations as seen with TEM and SEM with the exception of the SEM at 1:10 where large macro shapes were formed.

Table 6.2. Copper Oxide Nanoparticles Experimental Conditions and Morphologies.

Molar Ratio M^{+n}: Base	Solvent type/water	Morphology (dimension/nm)
1:5	Water	Thin sheets (length 1498 ± 291; width 400±10)
	70% Ethanol	Thin sheets (length 145 ± 62) with rods like structures
	DMF	Rice like particles (28 ± 6)
	Toluene	Thin sheets (length 1079 ± 453; width 370±10)
1:10	Water	Thin sheets (length 820 +/- 334; width 312 +/- 93)
	70% Ethanol	Rods (length 123 +/- 42; width 28 +/- 14)
	DMF	Ribbons (length 5034 +/- 995; width 791 +/- 254)
	Toluene	Rods (length 252 +/- 58; width 63 +/- 17) with Sheets
1:15	Water	Thin Sheets (length 697 +/- 269; width 315 +/- 68)
	70% Ethanol	Irregular structures
	DMF	Rods (length 99 +/- 23; width 24 +/- 8)
	Toluene	Thin Sheets (length 678 +/- 213; width 253 +/- 81)

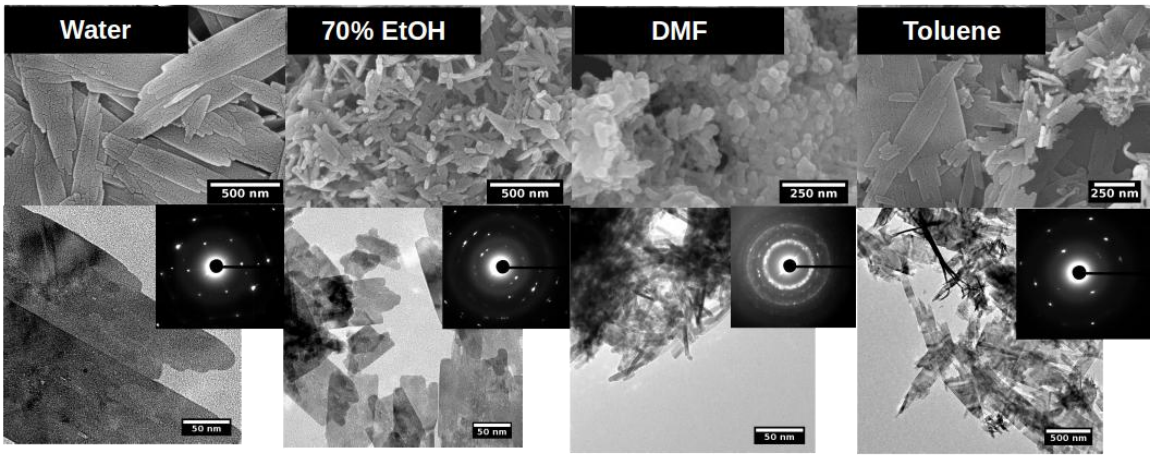

Figure 6.11. SEM and TEM Micrographs of Copper Oxide with a 1:5 Molar Ratio.

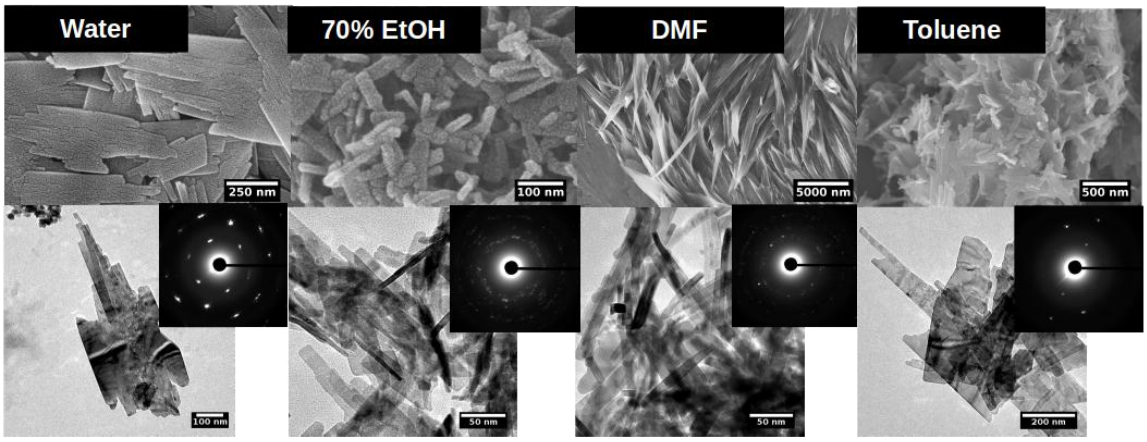

Figure 6.12. SEM and TEM Micrographs of Copper Oxide with a 1:10 Molar Ratio.

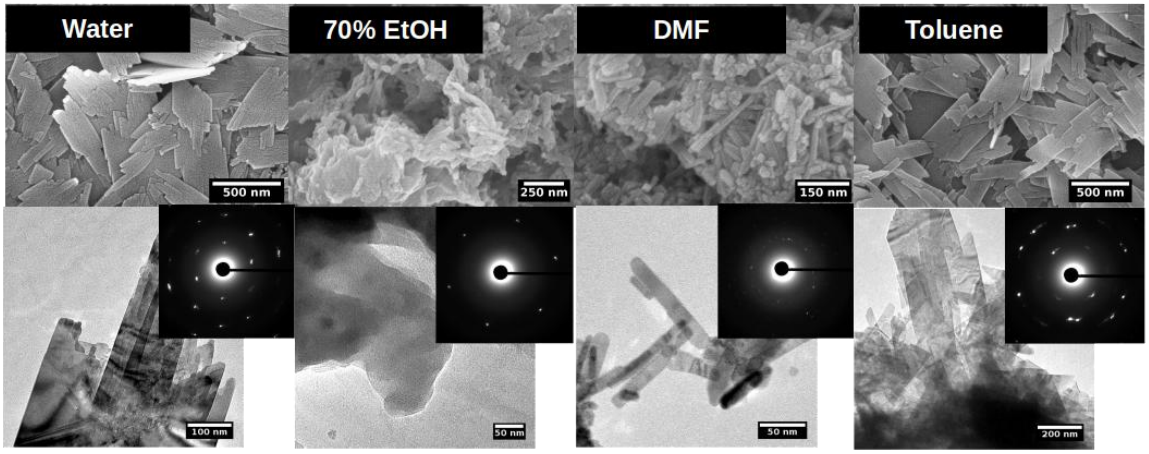

Figure 6.13. SEM and TEM Micrographs of Copper Oxide with a 1:15 Molar Ratio.

TEM diffraction was done on all these materials as well all showing a crystalline material. A further analysis using XRD shows a stinking similarity of the crystal pattern regardless of the solvent or the base concentration. Unlike Manganese Oxide, there is no one solvent that drives a different crystal packing along a unique crystal face. The XRD for all four solvents at1:5, 1:10 and 1:15 molar ratio are shown in Figure 6.14, 6.15 and 6.16 respectively. Using COD, a known crystal structure of Copper Oxide was found and

its theoretical XRD pattern was computed using VESTA. It can be seen in the XRD figures the overlay of that computational pattern. The identified crystal structure using this pattern overlay is CuO which is has a monoclinic space group. This structure can be accessed from COD using the ID number: 4105682. The intensity of experimental and the theoretical peaks match extraordinary well indicating that these materials all grow along the selected crystal face just as a bulk material would.

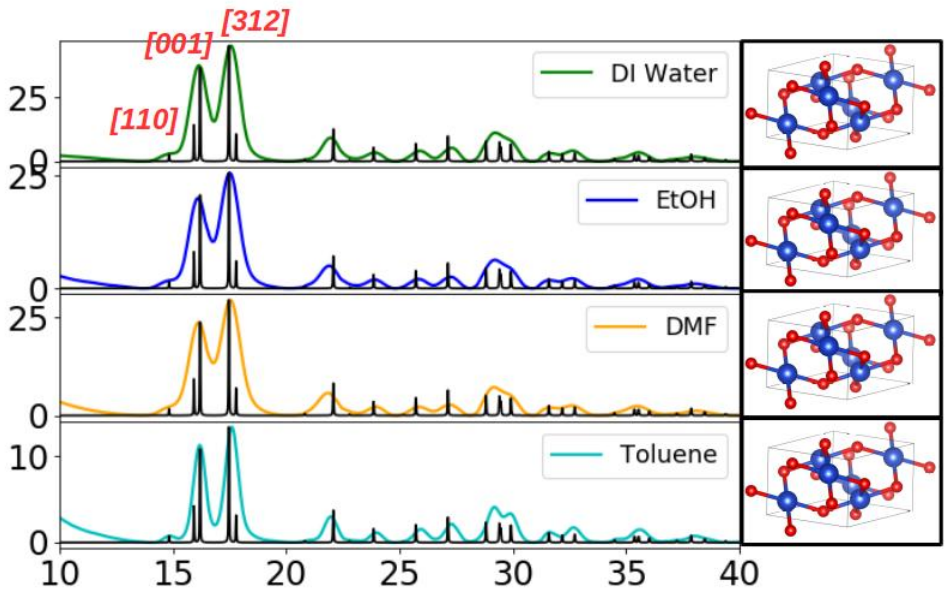

Figure 6.14. CuO XRD at a 1:5 Molar Ratio with Computational XRD Overlays and Crystal Unit Cell Rending Generated using VESTA. Crystal Structure COD ID: 4105682.

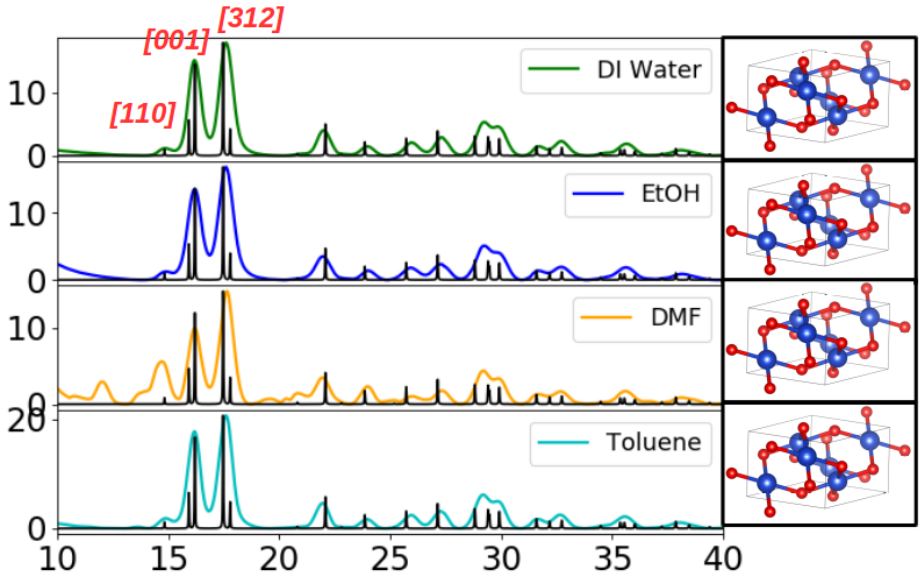

Figure 6.15. CuO XRD at a 1:10 Molar Ratio with Computational XRD Overlays and Crystal Unit Cell Rending Generated using VESTA. Crystal Structure COD ID: 4105682.

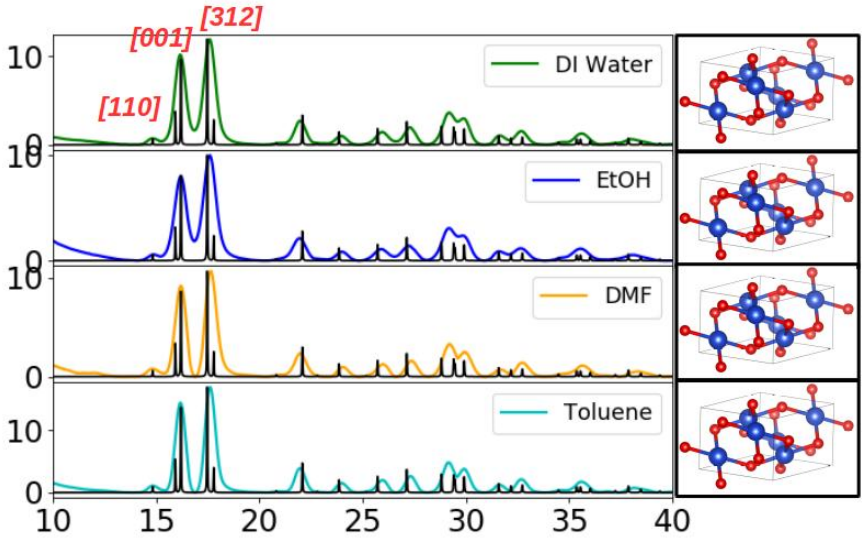

Figure 6.16. CuO XRD at a 1:15 Molar Ratio with Computational XRD Overlays and Crystal Unit Cell Rending Generated using VESTA. Crystal Structure COD ID: 4105682.

VI.4 Magnesium Hydroxide

The Magnesium based oxides made using the general synthesis method formed a hydroxide instead of an oxide nanoparticle. The identified stoichiometry of the material was $Mg(OH)_2$ with varying morphologies based on the solvent it was made in. The metal precursor used was Magnesium Chloride. Magnesium Hydroxide is used in a wide verity of applications such as flame-retardant, composite materials, paint, superconducting products and steel manufacturing[88–94]. The synthesis method used for these material is typically a hydrothermal reaction which requires high temperatures[88,91,95,96]. In literature one of the most common shapes of a Magnesium Hydroxide nanostructure is a hexagonal plate or plate like particle. This is quite similar to most of the particles made using the synthesis method described in chapter 5. While our method of producing Magnesium Hydroxide produced what appears to be a large set of morphologies, the most common one was that similar to a hexagonal plate. This morphology is corroborated in literature in a large range of journal articles[56,88,97–99]. A morphology reported in literature that was not created using our method is long rod/needle like structures. These were made using a wet chemical process where the resulting precipitant were the rods[95,100]. While it is shown in literature that Magnesium Hydroxide can be made using many different method, to the best of the authors knowledge this is the first time a sol-get method has been used to make $Mg(OH)_2$ hexagonal nanoplates.

Using the general synthesis method described in chapter 5, it is show that two distinct morphologies were created using the synthesis method: hexagonal plates and nanoparticles.The shape and morphology are shown in Table 6.3. Hexagonal nanoplates

were produced using water, DMF and toluene at all three molar ratios. Nanoparticles were produced using a water/ethanol mixture. All materials were imaged using SEM and TEM. The micrographs for all solvents at1:5, 1:10 and 1:15 molar ratio are shown in Figure 6.17, 6.18 and 6.19 respectively. It can be seen from these that average range of the plates range from 30 nm to 170 nm and the nanoparticles range from 20 nm to 70 nm.

Table 6.3. Magnesium Hydroxide Nanoparticles Experimental Conditions and Morphologies.

Molar Ratio M^{+n}: Base	Solvent type/water	Morphology (dimension/nm)
1:5	Water	Hexagonal plates (78 ± 39)
	70% Ethanol	Nanoparticles (48 ± 22)
	DMF	Hexagonal plates (53 ± 13)
	Toluene	Hexagonal plates (45 ± 15)
1:10	Water	Hexagonal plates (71 ± 25)
	70% Ethanol	Nanoparticles (44 ± 17)
	DMF	Hexagonal plates (136 ± 31)
	Toluene	Hexagonal plates (73 ± 49)
1:15	Water	Hexagonal plates (97 ± 24)
	70% Ethanol	Nanoparticles (53 ± 13)
	DMF	Hexagonal plates (69 ± 20)
	Toluene	Hexagonal plates (67 ± 26)

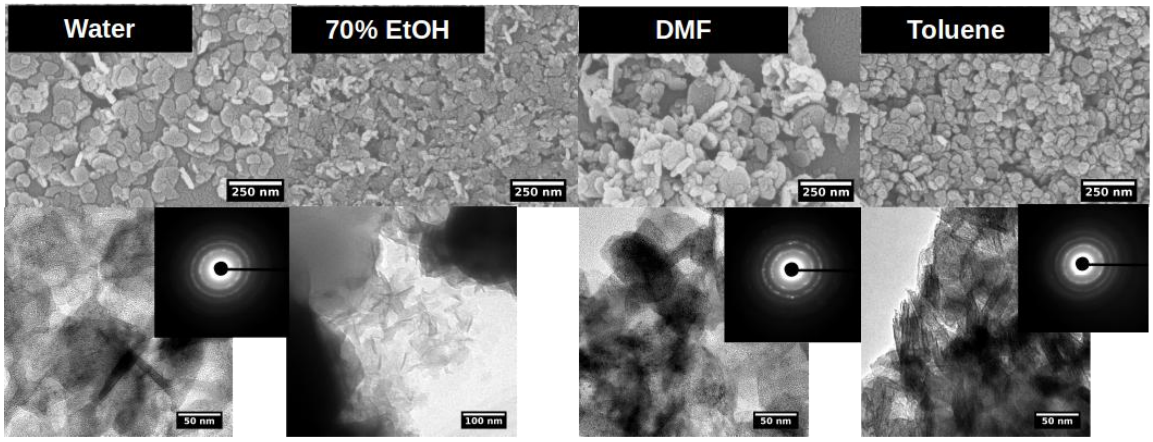

Figure 6.17. SEM and TEM Micrographs of Magnesium Hydroxide with a 1:5 Molar Ratio.

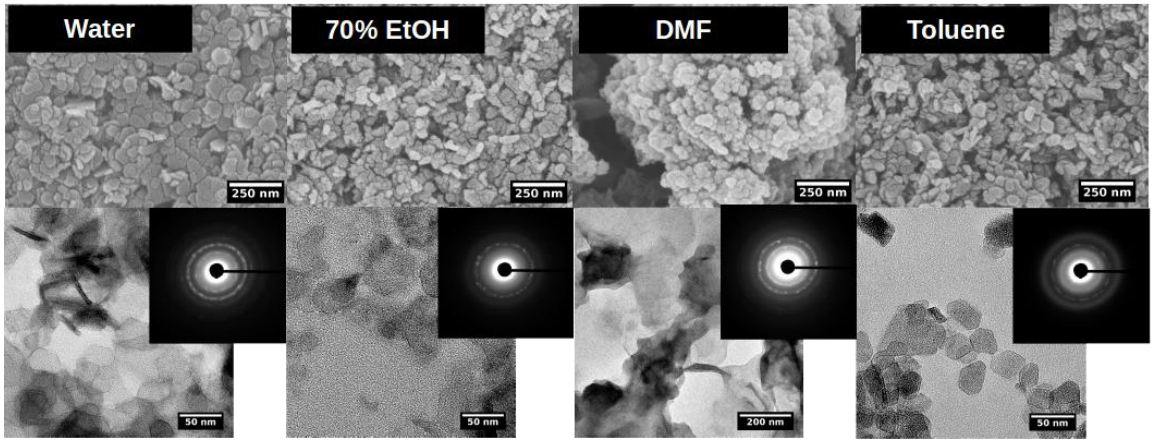

Figure 6.18. SEM and TEM Micrographs of Magnesium Hydroxide with a 1:10 Molar Ratio.

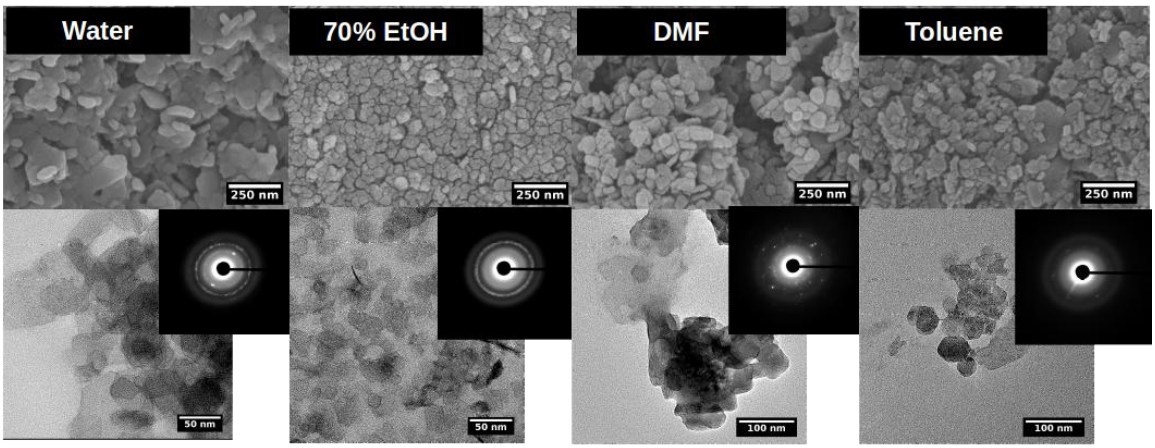

Figure 6.19. SEM and TEM Micrographs of Magnesium Hydroxide with a 1:15 Molar Ratio.

While the solvent controls the morphology of the nanoparticles, all of the nanomaterials have the same crystal structure. TEM SEAD diffraction shows that the particles are in fact crystalline and the micrographs show that they are solid, but still transparent. This indicates that while a crystal is growing, the nanocrystals are not perfectly aligned; the fact that these particles are also hydroxides means that the particles have more sheet like being held together by hydrogen bonding. All this is corroborated by XRD shown in for all four solvents ata 1:5, 1:10 and 1:15 molar ratio are shown in Figure 6.20, 6.21 and 6.22 respectively.

Using COD, a known crystal structure of Magnesium Hydroxide was found and its theoretical XRD pattern was computed using VESTA. It can be seen in the XRD figures the overlay of that computational pattern. The identified crystal structure using this pattern overlay is $Mg(OH)_2$ which is has a hexagonalspace group. This structure can be accessed from COD using the ID number: 1000054. The intensity of experimental and

the theoretical peaks match extraordinary well indicating that these materials all grow along the selected crystal face just as a bulk material would.

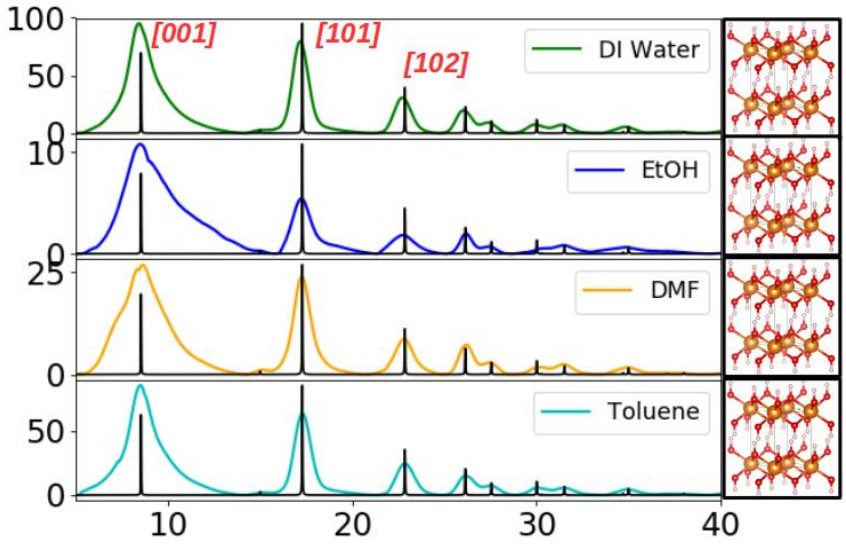

Figure 6.20. $Mg(OH)_2$ XRD at a 1:5 Molar Ratio with Computational XRD Overlays and Crystal Unit Cell Rending Generated using VESTA. Crystal Structure COD ID: 1000054.

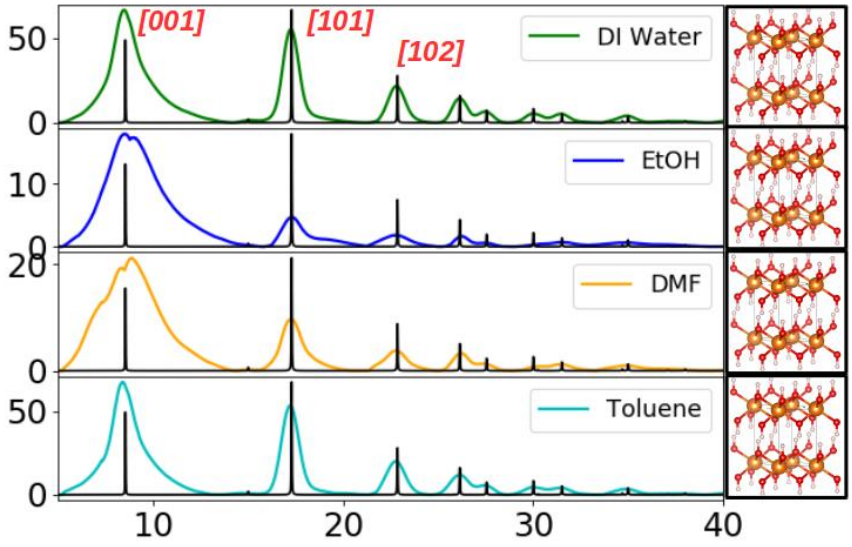

Figure 6.21. $Mg(OH)_2$ XRD at a 1:10 Molar Ratio with Computational XRD Overlays and Crystal Unit Cell Rending Generated using VESTA. Same Figure 6.21 COD ID.

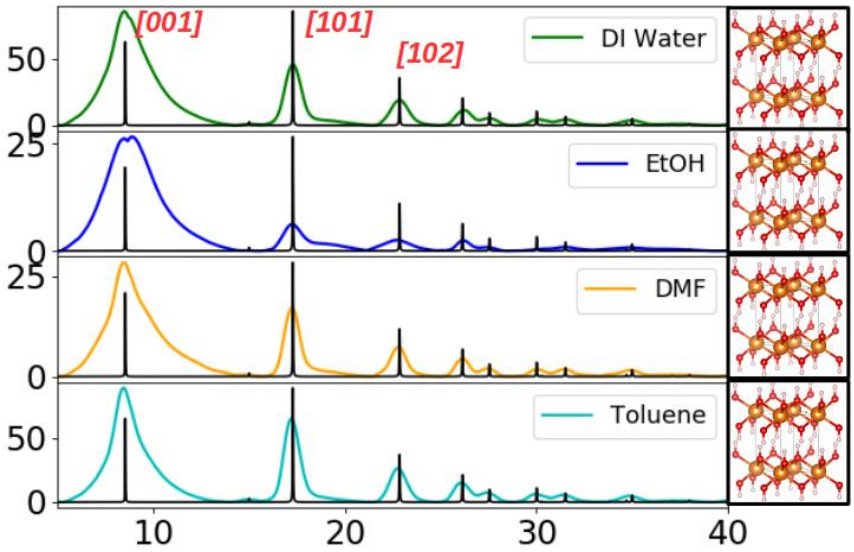

Figure 6.22 $Mg(OH)_2$ XRD at a 1:15 Molar Ratio with Computational XRD Overlays and Crystal Unit Cell Rending Generated using VESTA. Same Figure 6.21 COD ID.

VI.5 Chromium Oxide

The synthesis method described in chapter 5 was used to make Chromium Oxide nanoparticles. The resulting particles have a well defined morphologically but do not have a defined crystal structure. Chromium Oxide as a material has found uses as sensors, superconductors and absorbents[101]. Different methods have been shown in literature to make Chromium Oxide nanomaterials including, but not limited to: electrochemical[102], wet synthesis[103] and reduction[104]. These literature reports all showed nanoparticles being produced. The resulting particles using the synthesis method developed here and their sizes and shapes of each particle from each synthesis pathway are detailed in Table 6.4.

Table 6.4. Chromium Oxide Nanoparticles Experimental Conditions and Morphologies.

Molar Ratio M^{+n}: Base	Solvent type/water	Morphology (dimension/nm)
1:5	Water	Nanoparticles (54 +/- 17)
	70% Ethanol	Nanoparticles (27 +/- 8)
	DMF	Nanoparticles (33 +/- 12)
	Toluene	Nanoparticles (34 +/- 12)
1:10	Water	Nanoparticles (35 +/- 13)
	70% Ethanol	Nanoparticles (28 +/- 10)
	DMF	Nanoparticles (47 +/- 19)
	Toluene	Nanoparticles (43 +/- 12)
1:15	Water	Nanoparticles (57 +/- 32)
	70% Ethanol	Nanoparticles (48 +/- 14)
	DMF	Nanoparticles (38 +/- 23)
	Toluene	Nanoparticles (45 +/- 9)

In general, all the particles are the same size ranging between 33 nm to 57 nm. Every reaction produced nanoparticles. The morphology of the particles was examined using SEM and TEM. The micrographs for the 1:5 molar ratios for all solvents can be seen in Figure 5.5.The micrographs for all solvents at 1:5, 1:10 and 1:15 molar ratio are shown in Figure 6.23, 6.24 and 6.25 respectively.

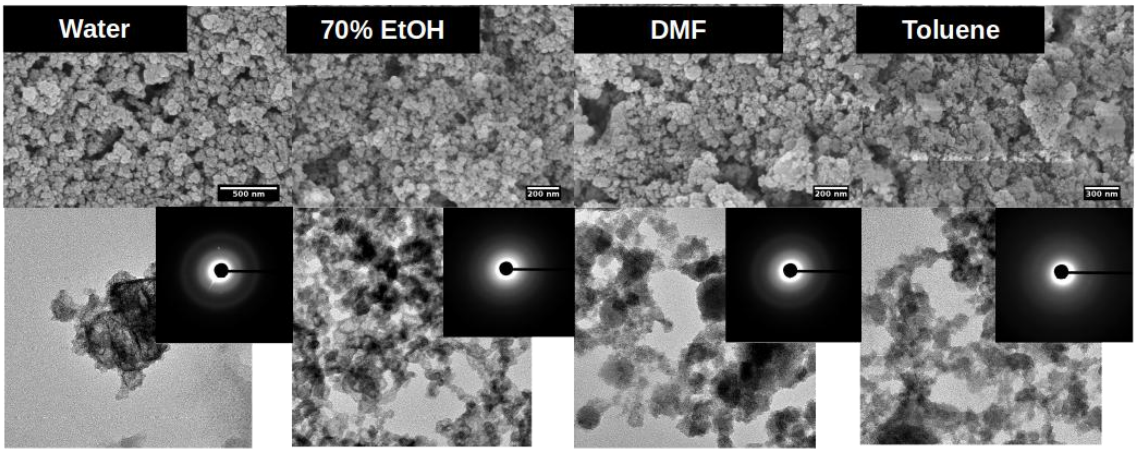

Figure 6.23. SEM and TEM Micrographs of Chromium Oxide with a 1:5 Molar Ratio.

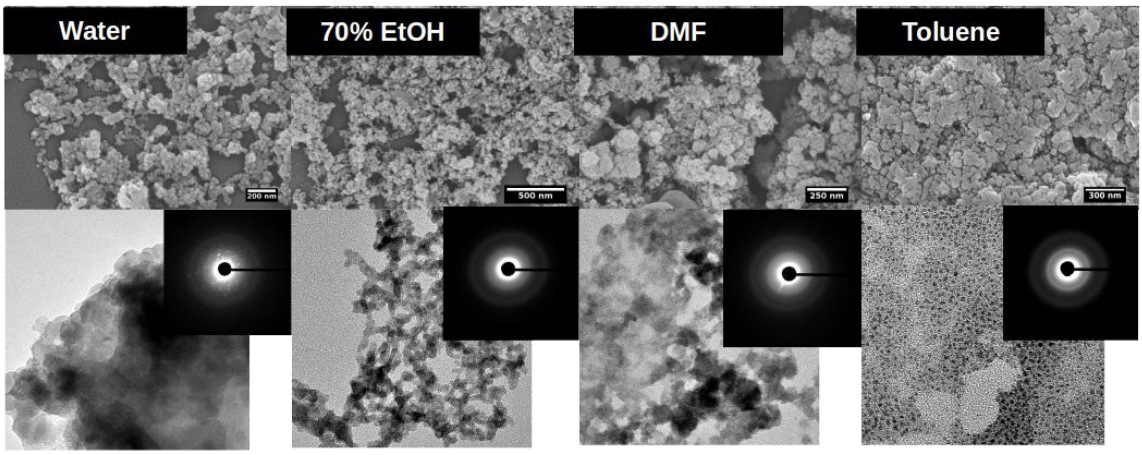

Figure 6.24. SEM and TEM Micrographs of Chromium Oxide with a 1:10 Molar Ratio.

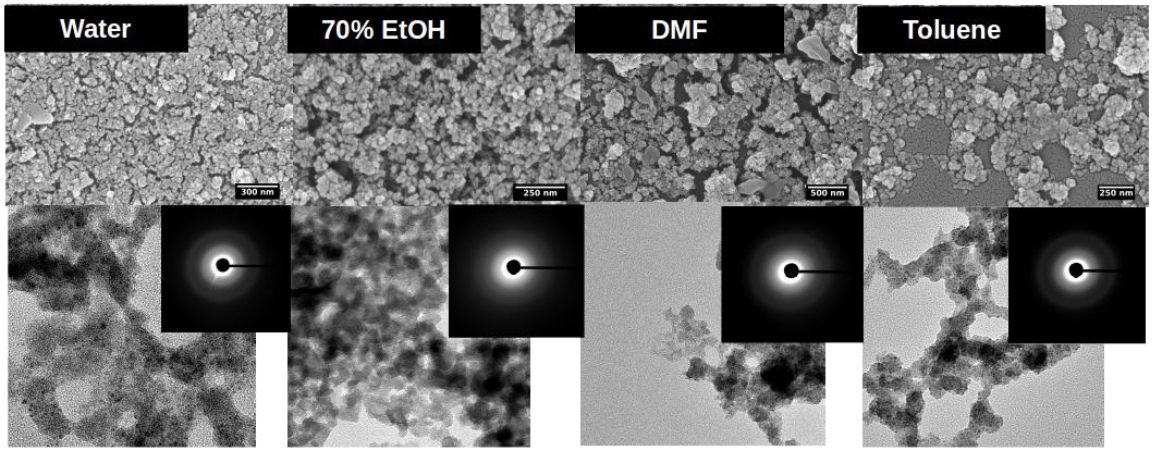

Figure 6.25. SEM and TEM Micrographs of Chromium Oxide with a 1:15 Molar Ratio.

The TEM clearly shows semi transparent particles indicative of nanocrystals not aligning along the crystal faces in a well ordered fashion. The TEM diffraction patterns clearly show some kind of crystal packing, but not well defined at all. This is corroborated using XRD at for all solvents and base concentrations at 1:5, 1:10 and 1:15 molar ratio as shown in Figure 6.26, 6.27 and 6.28 respectively.

All possible Chromium Oxide crystal structure in literature were attempted in an overlay on these XRD patterns like in the other metal oxides/hydroxides, but no suitable crystal structure was found to describe the atomic structure of this material. The peaks are very baud around the 10 degree mark indicating a very amorphous material, with no well defined crystal packing. This is true for all the XRD patterns for all molar ratios.

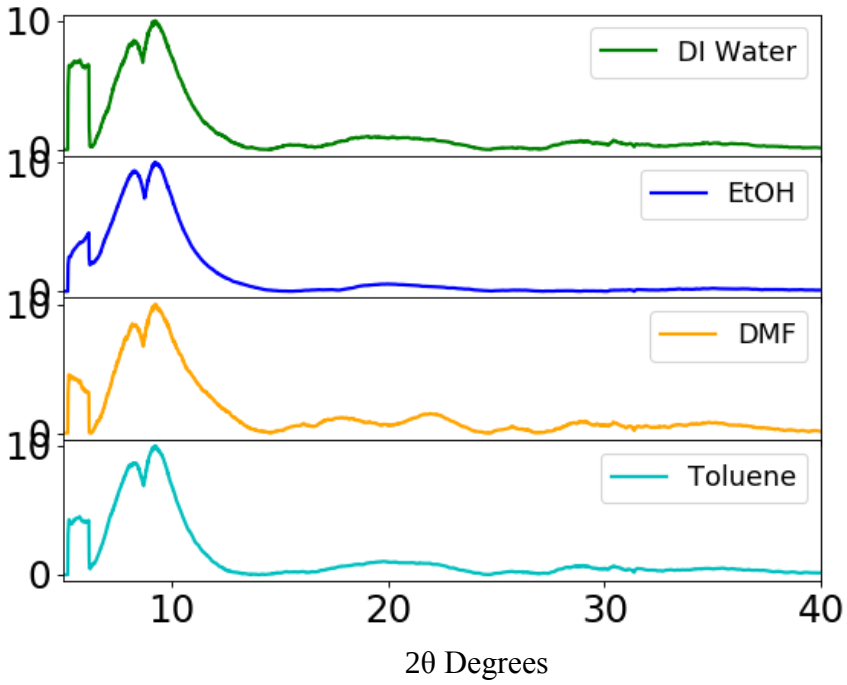

Figure 6.26. Chromium Oxide XRD of Particles with a 1:5 Molar Ratio.

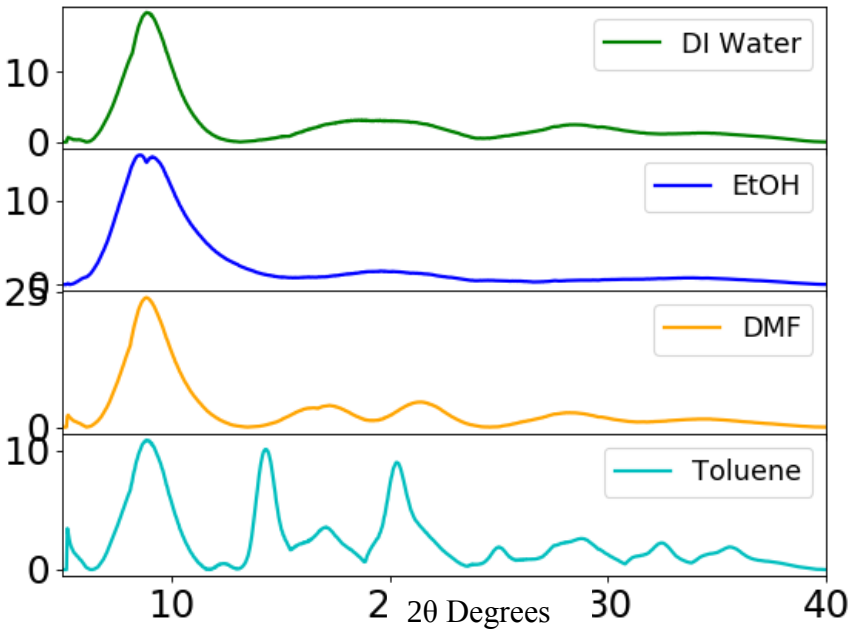

Figure 6.27. Chromium Oxide XRD of Particles with a 1:10 Molar Ratio.

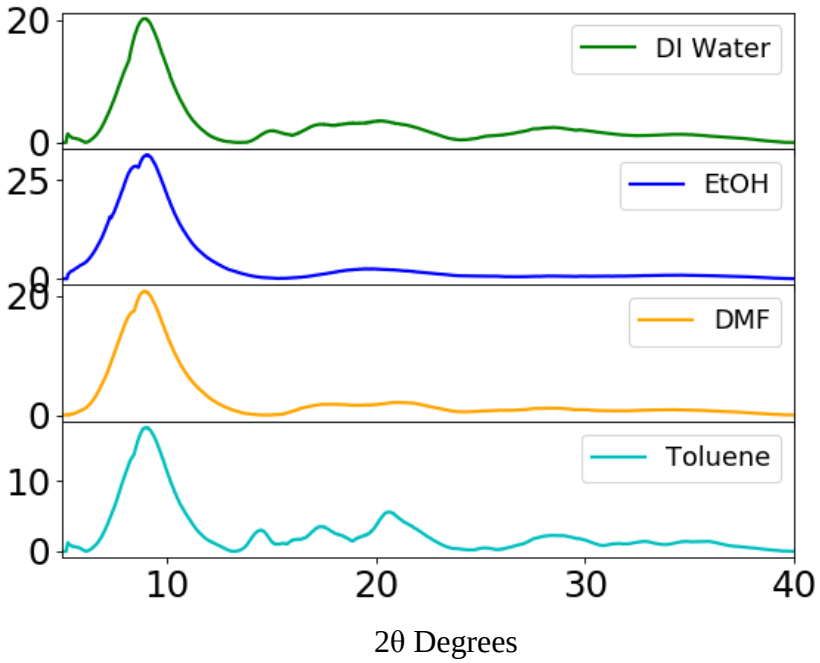

Figure 6.28. Chromium Oxide XRD of Particles with a 1:15 Molar Ratio.

VI.6 Strontium Oxide

The synthesis method described in chapter 5 was used to make Strontium Oxide materials, but not necessarily Nanomaterials all the time. The resulting materials all had well defined morphologies and structures, but the underlying crystal structure was not defined in any way. Strontium Oxide may help to design many different devices such as gas sensors, solar cells, semiconductors and electrodes for lithium ion batteries[105]. Various synthesis methods as well as morphologies have been indentified in literature; Athar showed that nanoparticles with a diameter of 200 nm could be formed using a wet chemical process[105]. Stankic showed that chemical vapor deposition could be used to make grain like Strontium Oxide structures with a diameter in the range of 100 nm[106] and Nemade shows that Strontium Oxide can be made into 0D-3D quantum dots using a one

pot chemical method[107]. The Strontium Oxide materials made using the method describe in chapter 5 create unique morphologies ranging from pecans to barbs and sheets. The size varies drasticallytoo as can be seen in Table 6.5.

Table 6.5. Strontium Oxide Nanostructures Experimental Conditions and Morphologies.

Molar Ratio M^{+n}: Base	Solvent type/water	Morphology (dimension/nm)
1:5	Water	Rods (6111 +/- 2225)
	70% Ethanol	Rods (2677 +/- 756)
	DMF	Pecans (1294 +/- 312)
	Toluene	Rods (300 +/- 126)
1:10	Water	Rods (1666 +/- 347)
	70% Ethanol	Rods (598 +/- 229)
	DMF	Nanorods (190 +/- 108)
	Toluene	Pecans (2580 +/- 935) and Rods (437 +/- 90)
1:15	Water	Sheets (759 +/- 412)
	70% Ethanol	Pecans (712 +/- 123) and Rods (178 +/- 97)
	DMF	Sheets (913 +/- 302)
	Toluene	Rods (800 +/- 114)

As can be seen, the smallest material is about 600 nm in length and ranges all the way up into the high micrometer range. There is no clear trend with the solvent or the molar ratios used in determining the morphology. The morphology of these materials was examined using SEM and TEM, the micrographs of for all four solvents at a 1:5, 1:10 and 1:15 molar ratio are shown in Figure 6.29, 6.30 and 6.31 respectively.

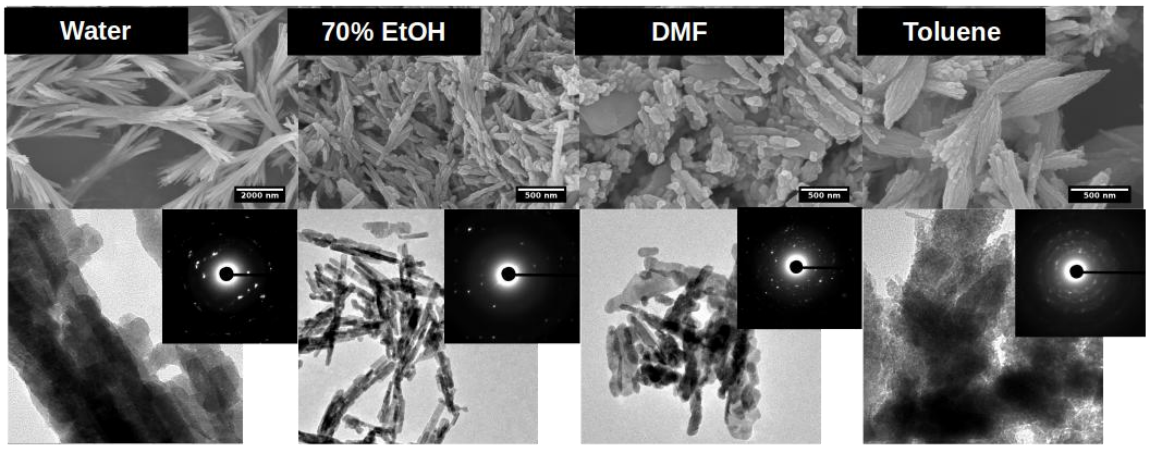

Figure 6.29. SEM and TEM Micrographs of Strontium Oxide with a 1:5 Molar Ratio.

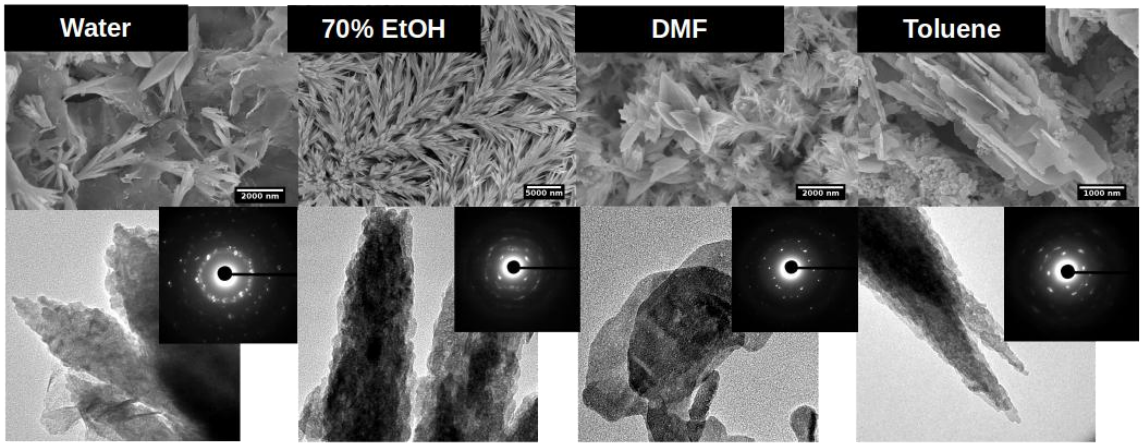

Figure 6.30. SEM and TEM Micrographs of Strontium Oxide with a 1:10 Base Ratio.

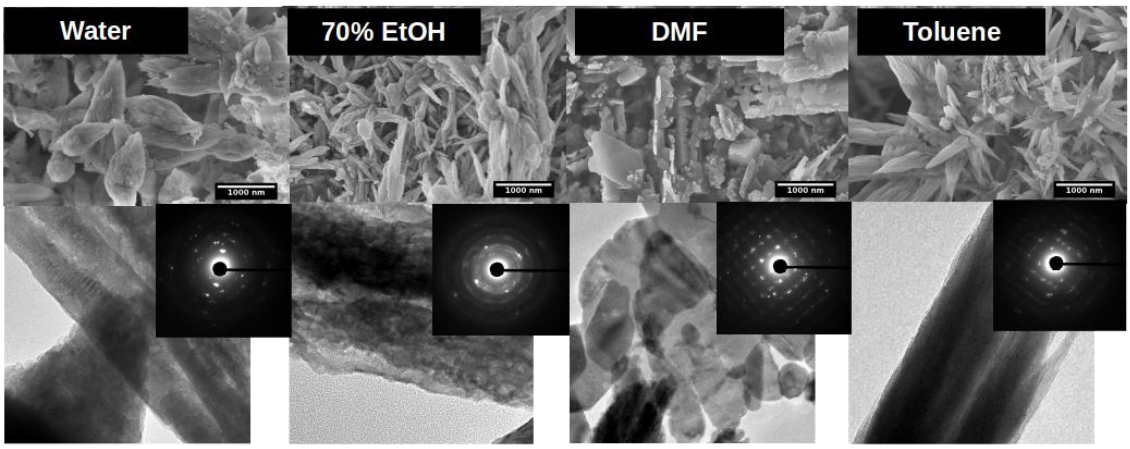

Figure 6.31. SEM and TEM Micrographs of Strontium Oxide with a 1:15 Base Ratio.

Looking more closely at the SEM and TEM, the materials made using water; ethanol and toluene all appear to be made from smaller rice like structures that clump into larger macro structures. It is not clear if this happens during sample preparation or if this is a natural process during the gelatin of the nanocrystals. The DMF seems to produce just the rice like nanocrystals that clump into the larger macro structures. In some cases like the 1:15 molar ratio made in DMF more plate like structures are made, the same with toluene at a 1:10 molar ratio. The driving mechanism behind the morphology is not clear in the least. It is clear though from the TEM diffraction using SEAD that there is a crystallinity underlying the structures. This is further examined using XRD whose diffraction pattern for all solvents at 1:5, 1:10 and 1:15 molar ratio are shown in Figure 6.32, 6.33 and 6.34 respectively.

All possible Strontium Oxide and Hydroxide crystal structure in literature were attempted in an overlay on these XRD patterns like in the other metal oxides/hydroxides,

but no suitable crystal structure was. There is a consistent pattern for all molar ratios past the 10 degree mark on the plot with the notable exception of ethanol at a 1:15 molar ratio.

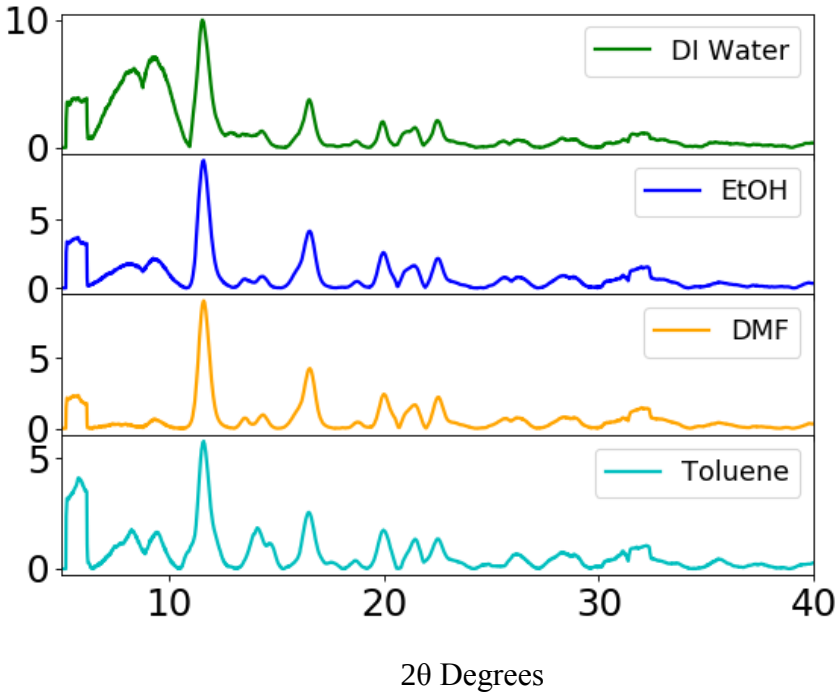

Figure 6.32. Strontium Oxide XRD of Particles with a 1:5 Molar Ratio.

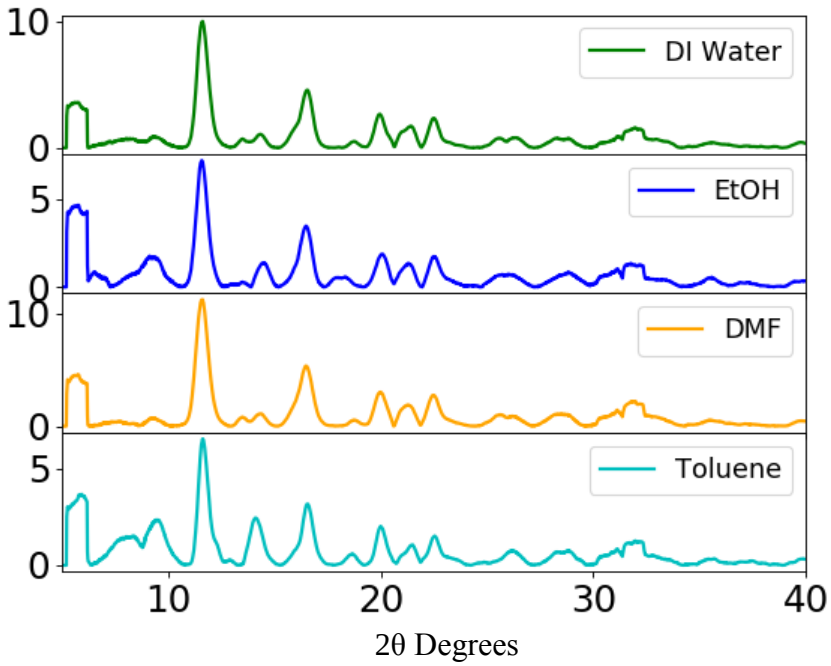

Figure 6.33. Strontium Oxide XRD of Particles with a 1:10 Molar Ratio.

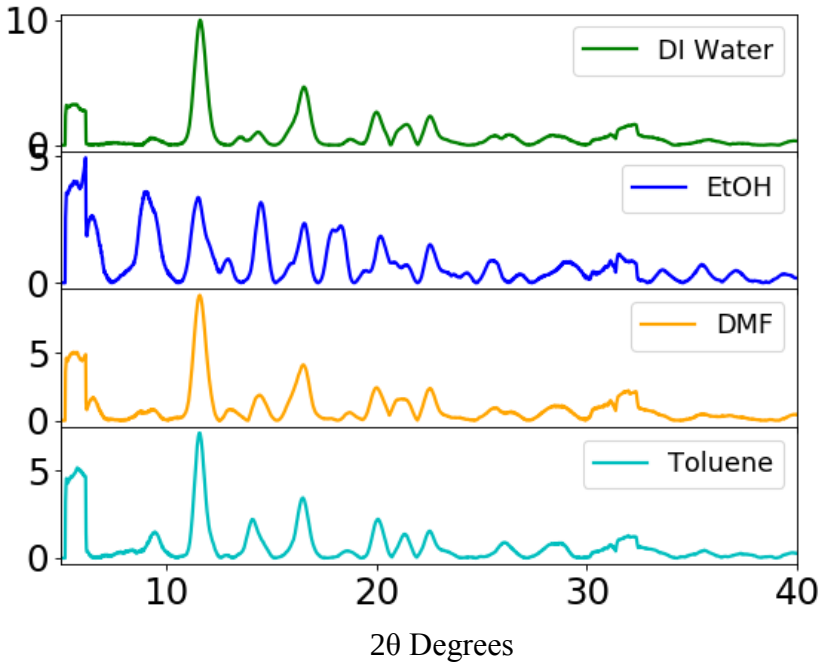

Figure 6.34. Strontium Oxide XRD of Particles with a 1:15 Molar Ratio.

CHAPTER VII

COMPUTATIONAL AND EXPERIMENTAL ANALYSIS OF THERMOELECTRIC PROPERTIES OF MANGANESE OXIDE

VII.1 Background of Manganese Oxide as a Thermoelectric Material

Manganese Oxide is not a very well studied material for thermoelectric applications. The nanoplates that were made using the sol-gel method have a high crystal packing with a known crystal structurewhich means the computational thermoelectric properties can be predicted. Knowing the crystal structure also enables its bulk version to be studied as well for comparison to the nanomaterial. The bulk form is purchased as a powder just as the nanomaterial is so that the same thermoelectric pellet testing procedure can be applied from chapter 5.

The reason that a bulk and nano material with the same crystal structure need to be examined is how thermal the properties of that material changes as it shrinks as well as the electrical properties. It is well established what happens to the thermal conductivity as the material is reduced in size[13], but how the electrical properties change is unknown; this is why the electrical conductivity and Seebeck coefficient are being examined for both the bulk and nano from of Manganese Oxide pressed into a pellet.

Manganese Oxide has shown a unique property based on the literature especially with the electrical properties relative to other thermoelectric materials; while it has

extensively been studied in the realm of synthesis only a hand full of articles have been published on its thermoelectric properties. Song reports that MnO_2 has a very high Seebeck coefficient measuring higher than 20,000 μV/K, which is much higher as an absolute magnitude than the Bi_2Te_3, -287 μV/K, which at the moment is industry standard. This high value was measured on Mn_2O nanoparticles that were purchased; these nanoparticles were pressed into a pellet and then heated to test their thermoelectric properties[108] similar to the procedure in chapter 5. A more traditional method of making thermoelectric bulk blocks was done by Metselaar. In his report a Manganese Oxide is purchased, ball milled and then pressed and sintered into a pellet; in contrast to Song's work this measurement is done on Mn_3O_4 instead of Mn_2O. The report on the thermoelectric performance of Mn_3O_4 shows similar results to Song, a very large Seebeck coefficient, but this report only examines the thermoelectric performance of this Oxide in the temperature range between 1100-1700 K because of its thermodynamic phase and stability[109]. Here the thermoelectric properties of Mn_3O_4 nanoplates pressed into a pellet is reported at a much lower temperature range from room temperature to 100 ^{0} C; this is the first time this has been reported to the authors knowledge.

Not only is the Seebeck coefficient being measured, but the electrical conductivity of both the bulk powder and nanopowder are measured. With the crystal structure of the nanoplates known, the process of predicting the theoretical thermoelectric properties was attempted using the methods developed in Chapter 5.

VII.2 Full Manganese Oxide Nanoparticle Analysis for Thermoelectric Characterization

The crystallinity of the nanoplates and the organic groups all inform the design of the thermoelectric characterization. Before testing the temperature dependent electrical conductivity and Seebeck coefficient the nanoplates are annealed under atmosphere at 500 ºC for 1 hour to remove all left over contaminate groups from synthesis and make the align more as a single crystal. After the plates are annealed they are poured into a 3D printed cylinder and two steel rods are inserted into each end and pressed using a hand press. This exerts approximately 500 MPa of pressure on the plates pressing it into a pellet. Heaters are attached to the steel rods to heat and anneal the pellet for 10 minutes while pressed at 100 ºC. This follows the procedure that is outlined in chapter 5. The electrical conductivity and Seebeck coefficient of the Manganese Oxide plates in an annealed pellet are shown in Figure 7.1 and 7.2 respectively.

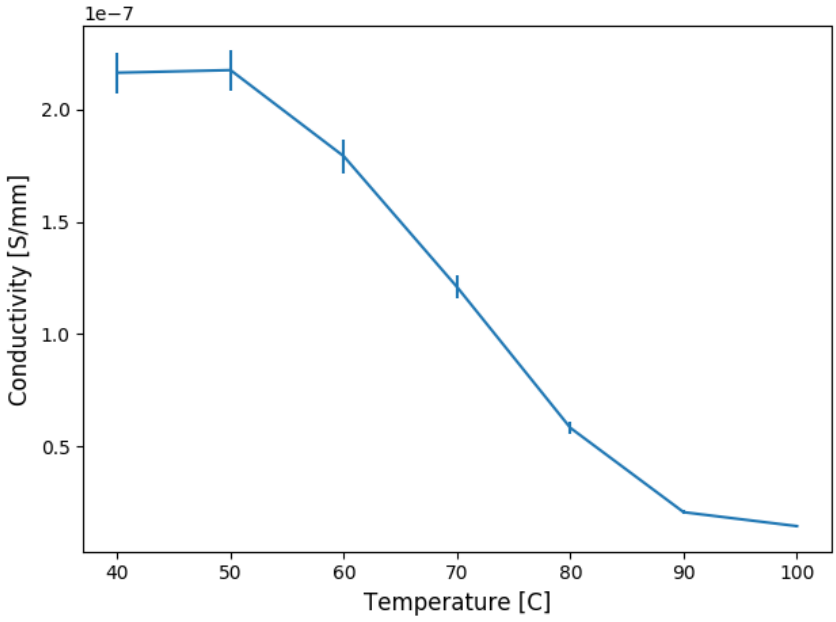

Figure 7.1. Electrical Conductivity of Mn_3O_4 Nanoplates Pressed as a Pellet.

The electrical conductivity of the pellet is extremely low in this case making this material basically an insulator. While the material is a poor conductor, it has an extremely large Seebeck coefficient. This is in line with what the literature states and what might be expected. The power factor on the other hand is dismal as is shown in Figure 7.3; this value was computed using Eq. 2.2.

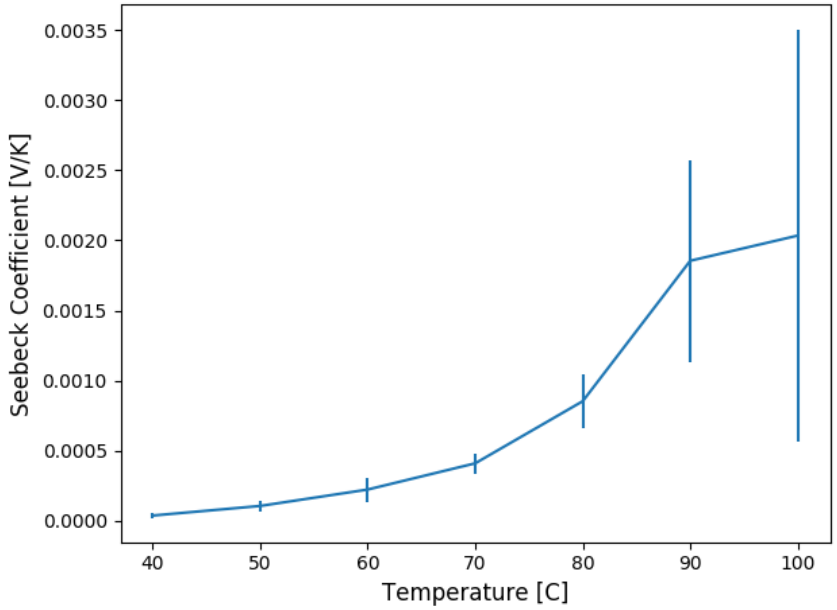

Figure 7.2. Seebeck Coefficient of Mn_3O_4 Nanoplates Pressed as a Pellet.

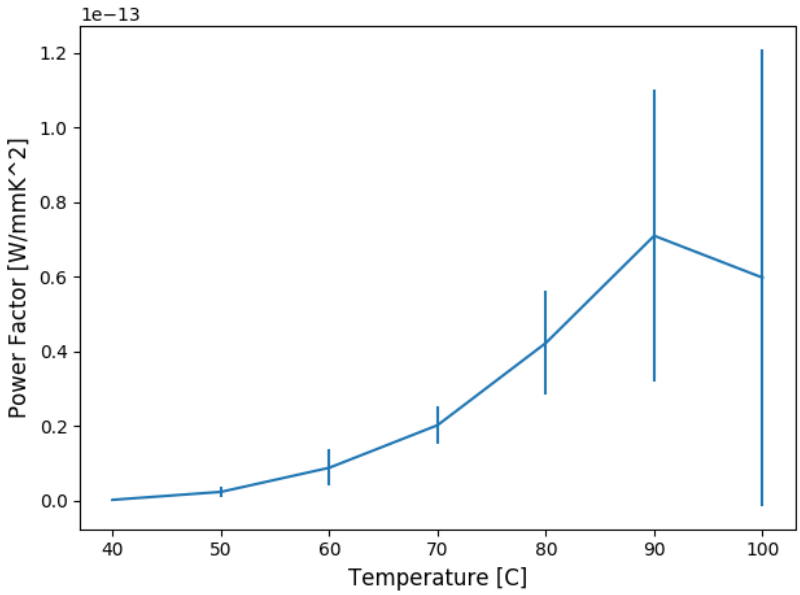

Figure 7.3. Power Factor of Mn_3O_4 Nanoplates Pressed as a Pellet.

This power factor is very low, about 10 orders of magnitude lower than other well accepted good thermoelectric materials. To validate that the nanoplates were still intact after thermal cycles for measuring the thermoelectric properties and survived the pressure SEM and XRD were done on the pellet to verify that the particles were intact. The SEM of the surface of the pellet is shown in Figure 7.4.

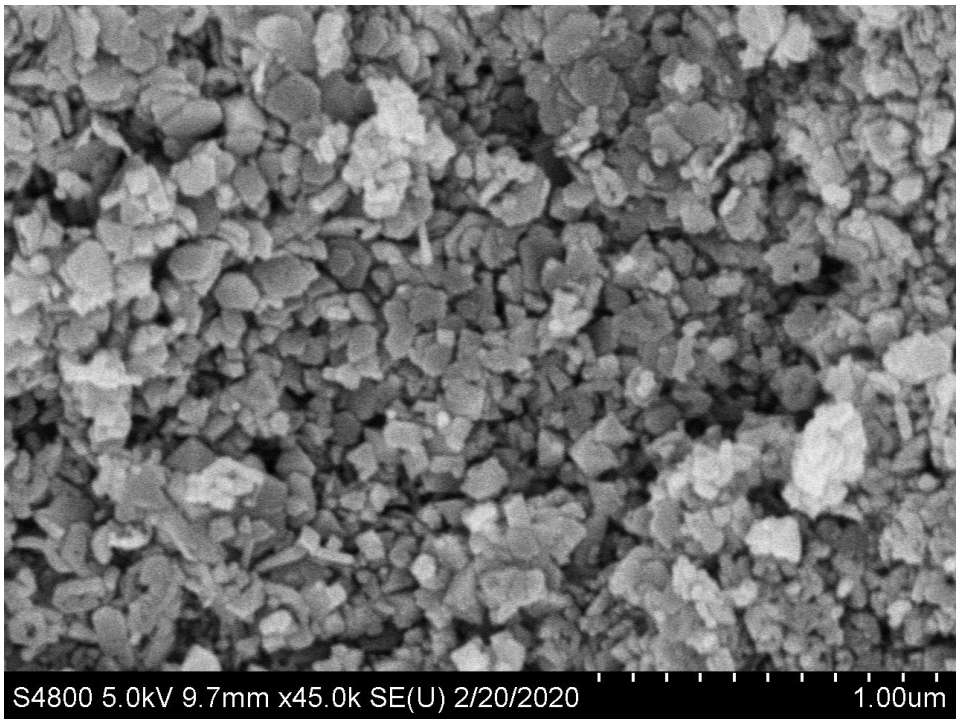

Figure 7.4. SEM of Surface of Pellet after Thermal Cycling and Pressing Particles.

It is clear from the SEM that the nanoplates are intact, but the morphology is not as well defined as the nanoplates after they are made using the sol-get method. The particles are measured from the image resulting in an average diameter of 105 +/- 23 nm. This is in contrast to the measured diameter of 130 +/- 40 nm after synthesis. The pellet after SEM imaging was scraped using a needle and the powder was suspended in water and solicited. A carbon coated TEM grid was dipped into the solution and left to dry and then imaged. The TEM and SEAD patterns are shown in Figure 7.5 and 7.6 respectively.

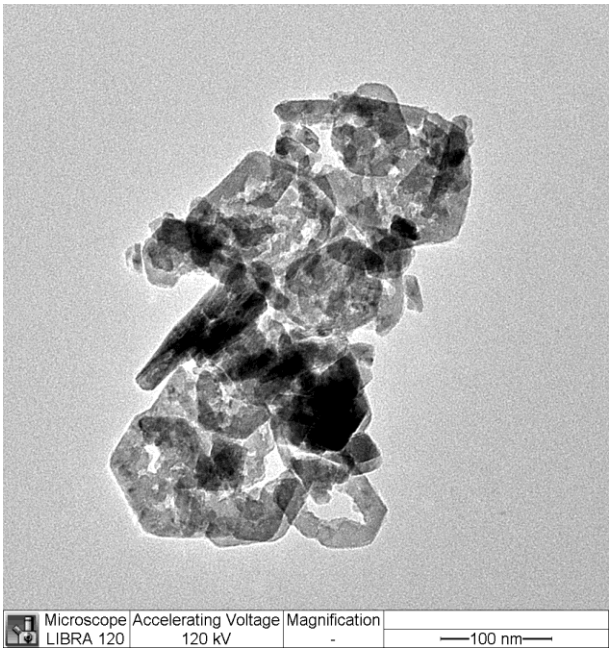

Figure 7.5. TEM of Nanoplates Scraped from the Surface of the Pellet after Thermoelectric Property Evaluation.

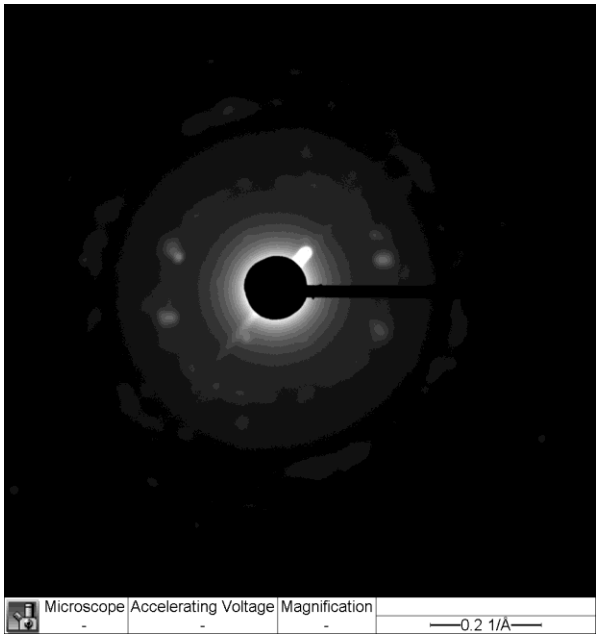

Figure 7.6. SEAD of Nanoplates Scraped from Surface of Pellet.

As can be seen from the TEM the nanoplates are not as in tact as the plates before the pellet production. SEAD shows that the plates still have a crystalline quality to them, but are slightly polycrystalline. The TEM shows clearly that the plates are fracturing and the morphology is not hexagonal as indicated to the SEM and well, just not as clear as the TEM. To verify the SEAD, XRD is done on the pressed powder from the pellet. The XRD is shown in Figure 7.7. The theoretical XRD from the identified crystal pattern is still a good match for the XRD pattern so the crystalline material is still intact. The peak intensities are not as aligned though as they were after the initial powder annealing. It is clear from this that the nanoplates do not stand up that well to the pressure and the temperature ranges that they are put through when during the thermal cycling of the pellet.

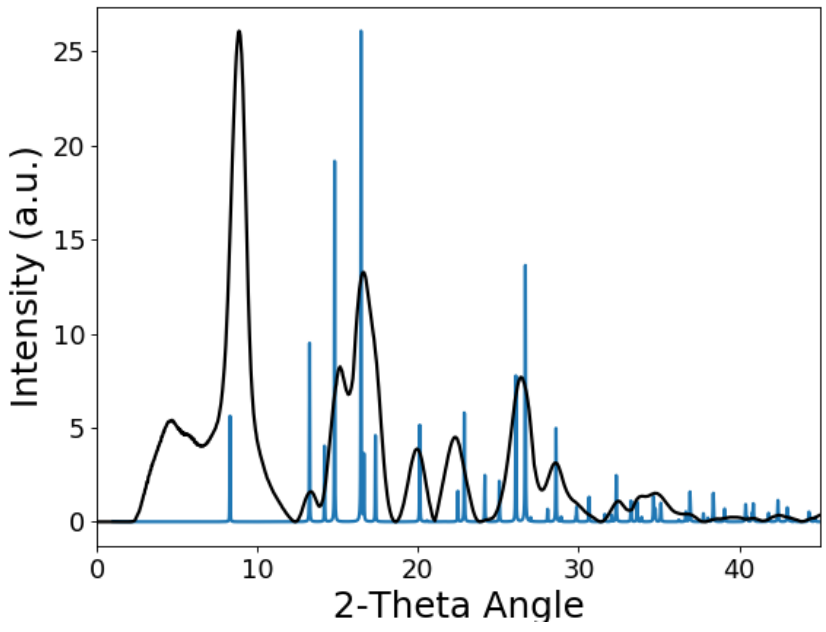

Figure 7.7. XRD of Pellet after Thermal Cycling and Pressing Particles.

VII.3 Characterization of Manganese (II,III) Oxide Bulk Powder

Mn_3O_4 powder was purchased from Sigma-Aldrich to correlate its TE properties with Mn_3O_4 nanoplates. The same procedure for creating a pellet and same conditions for measuring the thermoelectric properties were applied to the pellet made. The powder was not annealed; this was because the crystal structure was already correct and had the right peak intensities. The XRD of Mn_3O_4powder is shown in Figure 7.8.

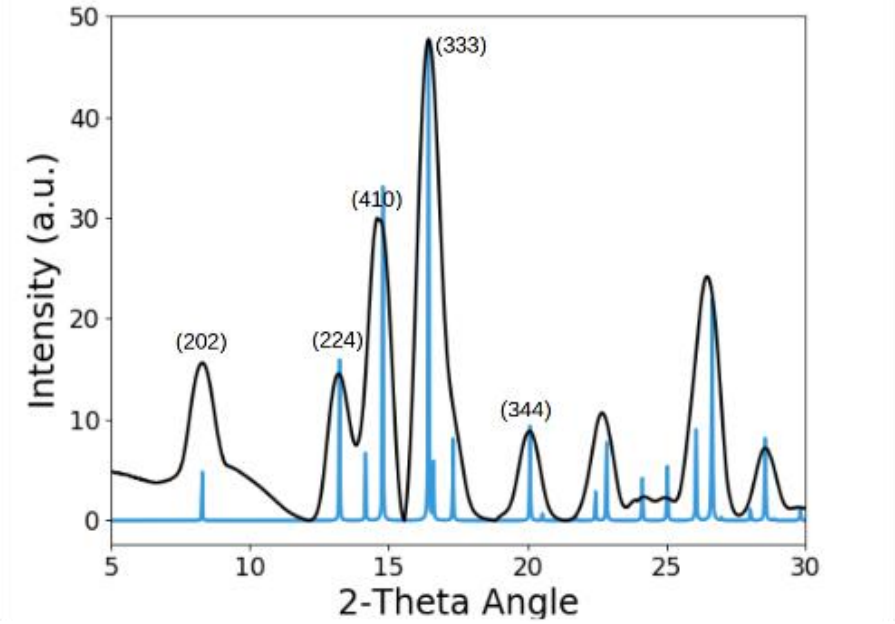

Figure 7.8. XRD of Manganese (II,III) Bulk Powder Overlaid with the Computational XRD Pattern for Mn_3O_4, COD ID: 1011262.

Because the correct crystal structure is already an attribute of the powder the pellet was pressed and the thermoelectric properties were measured. The electrical conductivity and Seebeck coefficient are shown in Figure 7.9 and 7.10 respectively.

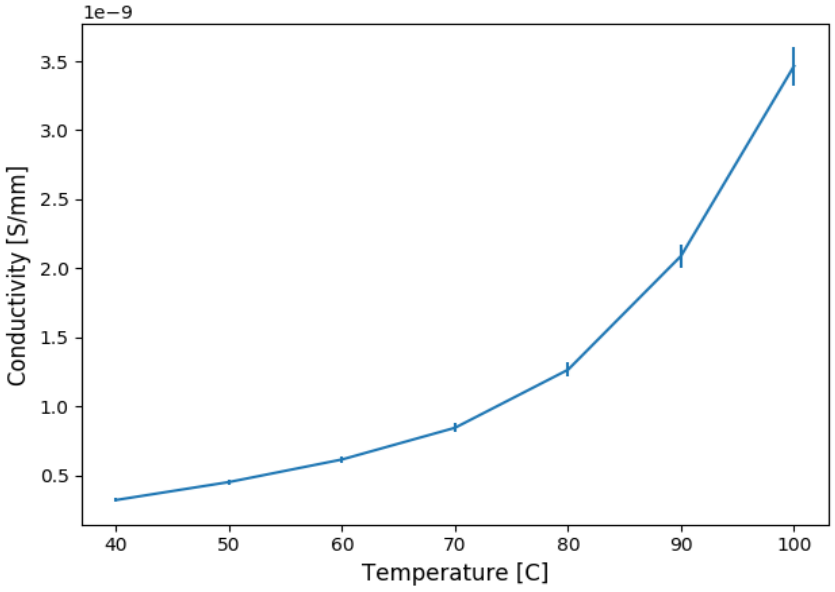

Figure 7.9. Electrical Conductivity of Manganese (II,III) Oxide Bulk Powder.

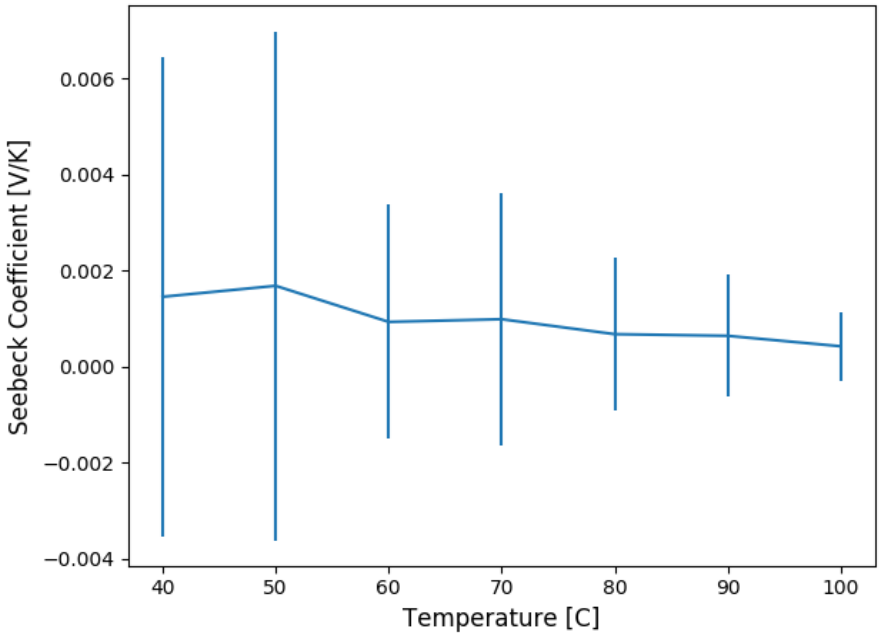

Figure 7.10. Seebeck Coefficient of Manganese (II,III) Oxide Bulk Powder.

The material is extremely insulting; the electrical conductivity is very low. The Seebeck coefficient is in the millivolt range as would be expected from the performance of the nanoparticles and literature. While the magnitude is correct, the error bars are so large that the value of the Seebeck coefficient cannot be determined with any certainty. This happens because of how insulating the material is. The source meter being used to measure the current induced by the Seebeck coefficient cannot be measured with high accuracy in this case leading to big jumps in current at some points. These current outliners even when trimmed out of the dataset still do not give an accurate reading of the current. After the thermal cycling the pellet did not remain intact after removing the pressure. This indicates a binder would be needed to make a proper pellet from the Manganese (II,III) oxide for testing. This might be one of the reasons for the highly insulating properties. Better equipment and sample preparationis needed for a material like this.

Because the Seebeck coefficient is indeterminate the power factor is not computed because it would not mean anything. If a comparison is done between the electrical properties of the nanoplate pellet and the bulk material pellet the conductivity is two orders of magnitude better for the nanoplates. This indicates that the electrical properties improved when the material was nanostructured. Also, the nanomaterial would also have a lower thermal conductivity due to frozen out phonon modes. Over all this shows that the nanomaterial is a better at conducting current, but no statement can be made about the power produced because of the Seebeck coefficient. While the conductivity is better from a relative perspective, both of these powders make a horrible

thermoelectric material; the performance metric is orders of magnitude lower then would be needed to even match current materials on the market, but this does show a that the method works.

VII.4 Computational Thermoelectric Properties for Mn_3O_4 Powder

Using XRD to match the computational crystal structure for both the nanoplates and the macro-scale powder Manganese Oxide, the computational crystal structure is known. The accepted structure is from the COD with the ID number: 1011262. The CIF files is rendered usingVESTA and is shown in Figure 7.11. The identified structure has a unit cell symmetry that is tetragonal with the unit cell lengths being a = b = 0.5762 nm and c = 0.9439 nm.

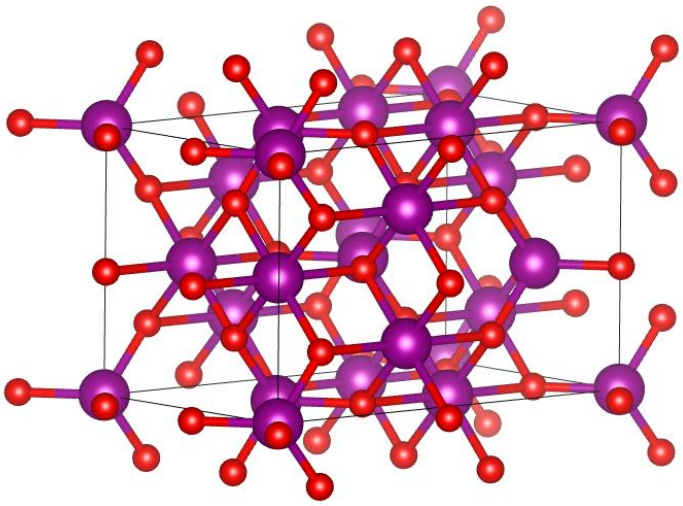

Figure 7.11. Mn_3O_4 Crystal Structure, COD ID: 1011262.

While many attempts were tried at computing the thermoelectric properties for this crystal structure using the method described in chapter 4, the properties were never able to be computed after months of attempts. Unlike the conclusions of the last few

sections where the nanomaterials did in fact improve performance, the fact that so much effort was put into computing the thermoelectric properties yielded null results shows that the hypothesis of rapidly predicting properties still needs work. The issues with this form of Manganese Oxide; there was always a band mismatch error during the computations before the thermoelectric properties could be computed. This is most likely due to an asymmetry in the unit cell, but no solution was ever found. After months of attempts nothing was produced, it was much faster going into the lab and collecting the data using experimental methods. It was shown that the band structure of Mn_3O_4 could be computed shown in Figure 7.12. While this does line up with other band structure on online databases, the band gap is very small only being 0.158 eV. For something this small it would be expected that the conductivity of the material would be high, not an insulator like the nanoplates and bulk powder pellets.

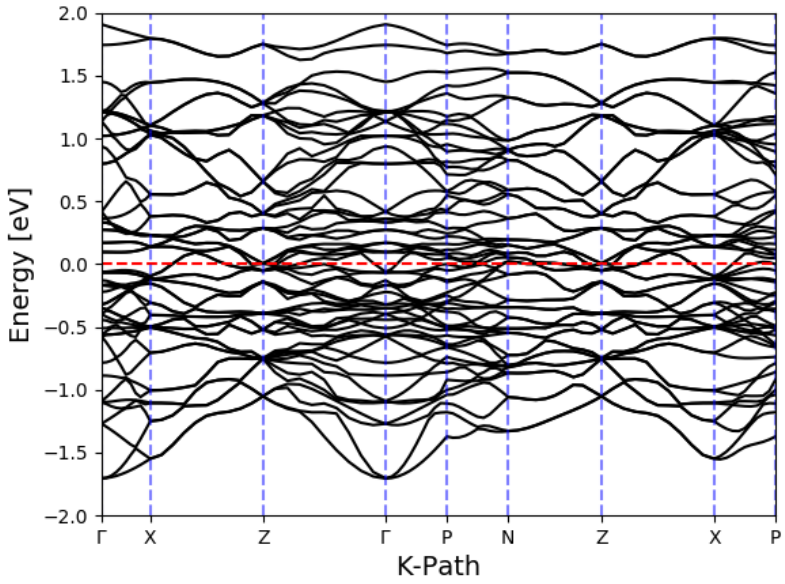

Figure 7.12. Band Structure of Mn_3O_4 Computed using Quantum ESPRESSO.

The issues are not with Density Functional Theory or Wannier functions or even the elements in this material. Another Manganese Oxide, MnO_2 was shown to work and that the thermoelectric properties could be predicted. The rendering of that unit cell is shown in Figure 7.13. The structure has a unit cell symmetry that is tetragonal with the unit cell lengths being a = b = 0.4388 nm and c = 0.2865 nm; the COD ID is 1514101.

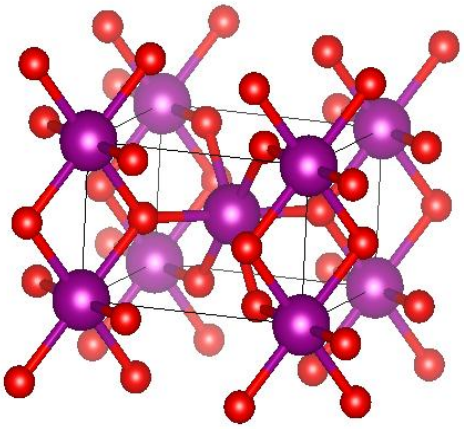

Figure 7.13. MnO_2 Crystal Structure, COD ID: 1514101.

The thermoelectric properties as well as the band structure for this material were computed. The electrical conductivity and Seebeck coefficient are shown in Figures 7.14 and 7.15 respectively.

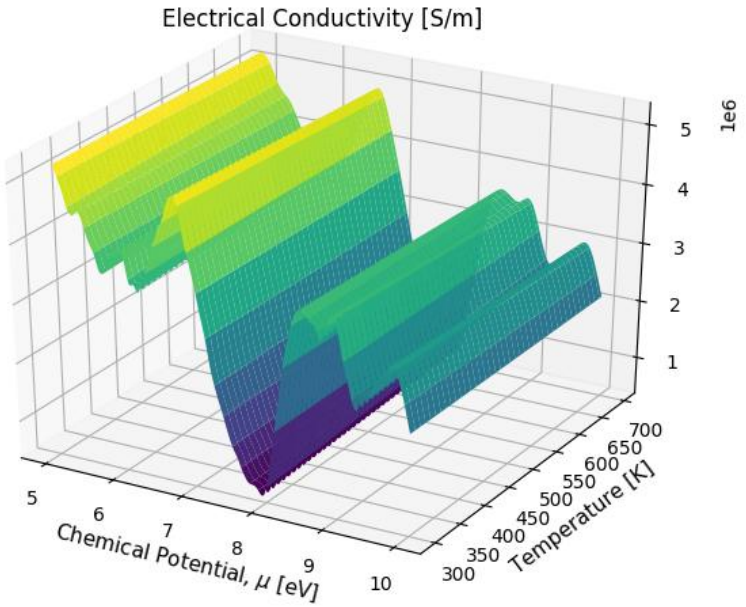

Figure 7.14. MnO_2 Computed Electrical Conductivity with Respect to Temperature and Chemical Potential.

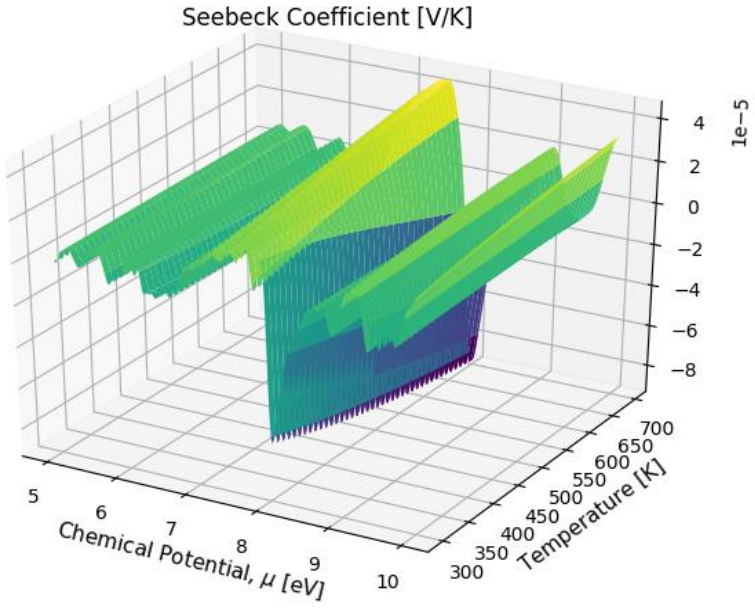

Figure 7.15. MnO_2 Computed Seebeck Coefficient with Respect to Temperature and Chemical Potential.

It is clear from the computations that the expected Seebeck coefficient is low, this is an issue when comparing the results to the literature where the Seebeck coefficient was in the microvolt range. This is not a very strong showing for the computational aspect. In some cases the computations resulted in a null solution where it could not be computed and in the other case the predicted value is not close to the literature value.

The power factor was computed from the Seebeck coefficient and the electrical conductivity as well as the band structure for MnO_2. Those are shown in Figure 7.16 and 7.17 respectively.

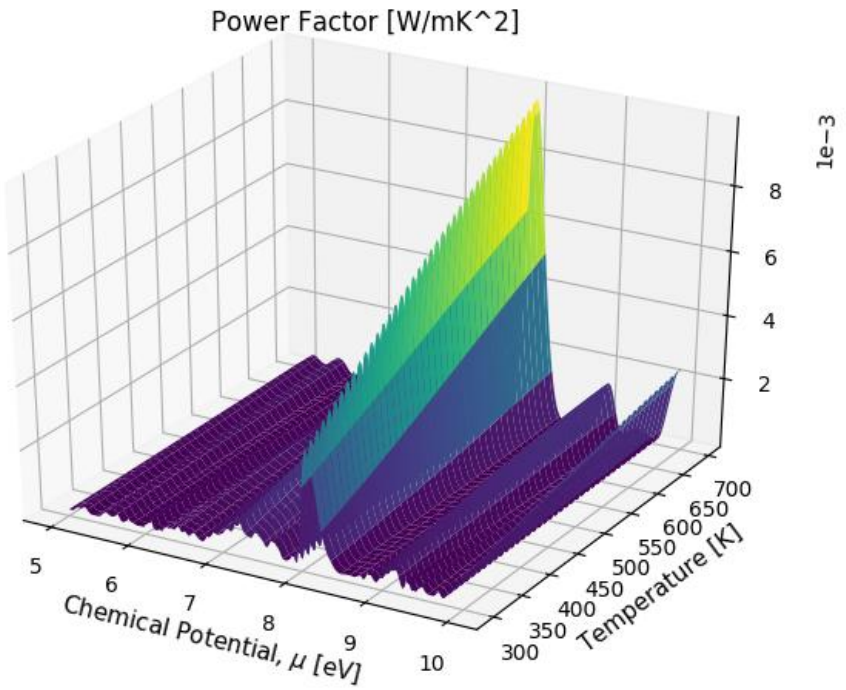

Figure 7.16. MnO_2 Computed Power Factor with Respect to Temperature and Chemical Potential.

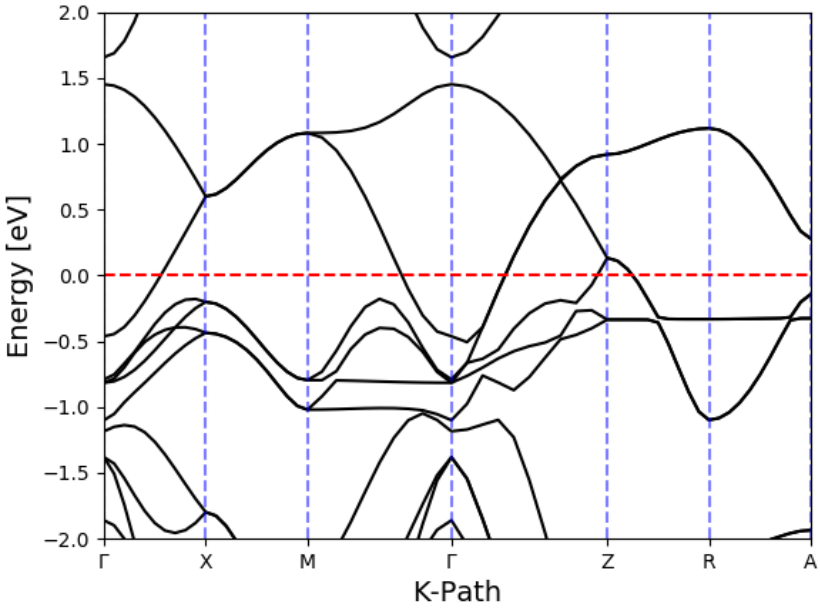

Figure 7.17. MnO_2 Computed Band Structure using Quantum ESPRESSO.

CHAPTER VIII

CONCLUSION

The recovery of industrial waste heat shows promise to increase overall efficiency if energy consumption in society. Thermoelectric generators (TEGs), if their current problems are addressed, are a technology poised to be of great use to convert waste heat to electricity. Current TEGs are made from rare, expensive elements and they operate at an efficiency low enough that they are currently not competitive in any way in the market albeit in niche applications. If current trends in research continue metal oxides have a promising future for thermoelectric applications, but much more work is needed to make sure they operate at a high enough efficiently.

The work done for this dissertation lays the initial ground work that can be used and improved upon to make TEGs. Metal oxides have shown promise in literature and a robust sol-gel method was developed here to make metal oxide nanomaterials that could be utilized in those thermoelectric devices. The applications for nanomaterials have been demonstrated in literature as a method of reducing the thermal conductivity of materials, which increases the overall thermal conversion efficiently of the thermoelectric materials. The sol-get methods shown here illustrate a way of making those nanomaterials in larger scale. A future direction that could be taken is to expand the sol-gel method to make multi metal oxides that would introduce new properties into the metal oxides that might

improve the thermal stability of the particles, make the electrical properties more appealing for thermoelectric applications and help tune the thermal conductivity.

The search for new thermoelectric materials was also bolstered with the establishment of a computational method to predict the thermoelectric properties of a single crystal material using periodic boundary conditions. This method uses existing software, but they have been put together in a way that can predict the electrical properties of a crystalline material. It has been documented now how to make this work and the method has been automated removing human error and speeding up predictions by running computations around the clock. Future versions of the software should expand on making sure that the properties of a nanomaterial can be predicted, not just macro-scale materials that utilize periodic boundary conditions on a unit cell for the computations. The software that was chosen was picked for this explicit reason; the properties of nanocrystals can be predicted by expanding the current framework that was developed here. The prediction of the thermoelectric properties of a nanocrystal will allow a study to be done to see if current DFT methods can predict the thermoelectric properties of nanostructures.

A method to make nanomaterials and a computational method for predicting the thermoelectric properties has been established. A method was also developed to measure the temperature dependent thermoelectric properties of the synthesized nanomaterials. This method, while it shows decent results for known materials, can be improved for future applications. The temperature range that properties can be measured at can be increased and the thermal stability of the pellets that are made for these measurements

can be improved. Any future pellets might also need to have a binder introduced into the powder matrix to improve the pellet stability.

All of these methodsculminate in a final thermoelectric analysis of manganese oxide. The thermoelectric properties of manganese oxide are measured on both nanoplates made using our sol-gel method and its macro-scale material that is purchased with a powder size in the micrometer range. The temperature dependent Seebeck coefficient and electrical conductivity of both the nanoplates and powder were measured. The crystal structure was determined for the manganese oxide using a structure based on literature; the stoichiometry of the manganese oxide is Mn_3O_4. The electrical conductivity of both materials were measured and the nanomaterial was more conductive then the purchased bulk powder. The method to measure the Seebeck coefficient measured a very large coefficient for the nanoplates, but the result was inconclusive for the bulk powder. This was due to the lower limits of the equipment being hit while measuring the Seebeck coefficient. The manganese oxide in general is not a good material at all for thermoelectric applications, so it is not necessarily surprising that the developed method did not work well. If another material was testing it might have yielded different results.

The final part of the comparison study was using the identified structure to compute the theoretical computational thermoelectric properties for bulk Mn_3O_4. After an enormous amount of time, it was concluded, most likely due to a symmetry issue, that the thermoelectric power factor for Mn_3O_4 could not be computed. The power factor for MnO_2 could be computed though showing that the computational methods could be applied to a manganese oxide, but not Mn_3O_4. In about every case, from the experimental

to the computational methods manganese oxide found the edge cases where most of the methods failed in the area of thermoelectric characterization. This would most likely not be an issue if another material was chosen to be tested.

With all these pieces put in place a framework to rapidly create new thermoelectric materials,it is clear that more work can be done. It was the hope of this dissertation to do the heavy lifting of getting this project off the ground and heading in the right direction. While some of it is not complete, there are clear paths forward on what needs improvement to make this method more complete in its entirety.

REFERENCES

(1) Forman, C.; Muritala, I. K.; Pardemann, R.; Meyer, B. Estimating the Global Waste Heat Potential. *Renewable and Sustainable Energy Reviews***2016**, *57*, 1568–1579. https://doi.org/10.1016/j.rser.2015.12.192.

(2) Snyder, G. J.; Toberer, E. S. Complex Thermoelectric Materials. *Nature Mater***2008**, *7* (2), 105–114. https://doi.org/10.1038/nmat2090.

(3) Thermoelectric Materials , Devices and Systems : Technology Assessment. Department of Energy February 13, 2015.

(4) He, J.; Tritt, T. M. Advances in Thermoelectric Materials Research: Looking Back and Moving Forward. *Science***2017**, *357* (6358), eaak9997. https://doi.org/10.1126/science.aak9997.

(5) Massey, K. Removing excess nuclear waste from Alaska https://www.sandia.gov/news/publications/labnews/articles/2015/16-10/rtg_removal.html.

(6) Matsubara, K. Development of a High Efficient Thermoelectric Stack for a Waste Exhaust Heat Recovery of Vehicles. In *Twenty-First International Conference on Thermoelectrics, 2002. Proceedings ICT '02.*; IEEE: Long Beach, CA, USA, 2002; pp 418–423. https://doi.org/10.1109/ICT.2002.1190350.

(7) DiSalvo, F. J. Thermoelectric Cooling and Power Generation. *Science***1999**, *285* (5428), 703–706. https://doi.org/10.1126/science.285.5428.703.

(8) Hicks, L. D.; Dresselhaus, M. S. Effect of Quantum-Well Structures on the Thermoelectric Figure of Merit. *Phys. Rev. B***1993**, *47* (19), 12727–12731. https://doi.org/10.1103/PhysRevB.47.12727.

(9) Kittel, C. *Introduction to Solid State Physics*, 8th ed.; Wiley: Hoboken, NJ, 2005.

(10) Zhou, Y.; Hu, M. Record Low Thermal Conductivity of Polycrystalline Si Nanowire: Breaking the Casimir Limit by Severe Suppression of Propagons. *Nano Lett.***2016**, *16* (10), 6178–6187. https://doi.org/10.1021/acs.nanolett.6b02450.

(11) Roduner, E. Size Matters: Why Nanomaterials Are Different. *Chem. Soc. Rev.***2006**, *35* (7), 583. https://doi.org/10.1039/b502142c.

(12) Tang, J.; Wang, H.-T.; Lee, D. H.; Fardy, M.; Huo, Z.; Russell, T. P.; Yang, P. Holey Silicon as an Efficient Thermoelectric Material. *Nano Lett.***2010**, *10* (10), 4279–4283. https://doi.org/10.1021/nl102931z.

(13) Wan, C.; Wang, Y.; Wang, N.; Norimatsu, W.; Kusunoki, M.; Koumoto, K. Development of Novel Thermoelectric Materials by Reduction of Lattice Thermal Conductivity. *Science and Technology of Advanced Materials***2010**, *11* (4), 044306. https://doi.org/10.1088/1468-6996/11/4/044306.

(14) Neophytou, N.; Kosina, H. Optimizing Thermoelectric Power Factor by Means of a Potential Barrier. *Journal of Applied Physics***2013**, *114* (4), 044315. https://doi.org/10.1063/1.4816792.

(15) Furmanchuk, A.; Saal, J. E.; Doak, J. W.; Olson, G. B.; Choudhary, A.; Agrawal, A. Prediction of Seebeck Coefficient for Compounds without Restriction to Fixed Stoichiometry: A Machine Learning Approach. *J. Comput. Chem.***2018**, *39* (4), 191–202. https://doi.org/10.1002/jcc.25067.
(16) Wei, J.; Liu, H. J.; Cheng, L.; Zhang, J.; Liang, J. H.; Jiang, P. H.; Fan, D. D.; Shi, J. Tuning the Carrier Concentration to Improve the Thermoelectric Performance of $CuInTe_2$ Compound. *AIP Advances***2015**, *5* (10), 107230. https://doi.org/10.1063/1.4935051.
(17) White, A. The Materials Genome Initiative: One Year On. *MRS Bull.***2012**, *37* (8), 715–716. https://doi.org/10.1557/mrs.2012.194.
(18) Jain, A.; Ong, S. P.; Hautier, G.; Chen, W.; Richards, W. D.; Dacek, S.; Cholia, S.; Gunter, D.; Skinner, D.; Ceder, G.; et al. Commentary: The Materials Project: A Materials Genome Approach to Accelerating Materials Innovation. *APL Materials***2013**, *1* (1), 011002. https://doi.org/10.1063/1.4812323.
(19) Nosengo, N. THE MATERIAL CODE Machine-Learning Techniques Could Revolutionize How Materials Science Is Done. *NATURE***2016**, *533*.
(20) Dughaish, Z. H. Lead Telluride as a Thermoelectric Material for Thermoelectric Power Generation. *Physica B: Condensed Matter***2002**, *322* (1–2), 205–223. https://doi.org/10.1016/S0921-4526(02)01187-0.
(21) Davis, K.; Yarbrough, R.; Froeschle, M.; White, J.; Rathnayake, H. Band Gap Engineered Zinc Oxide Nanostructures via a Sol–Gel Synthesis of Solvent Driven Shape-Controlled Crystal Growth. *RSC Adv.***2019**, *9* (26), 14638–14648. https://doi.org/10.1039/C9RA02091H.
(22) Lu, X.; Morelli, D. T.; Xia, Y.; Ozolins, V. Increasing the Thermoelectric Figure of Merit of Tetrahedrites by Co-Doping with Nickel and Zinc. *Chem. Mater.***2015**, *27* (2), 408–413. https://doi.org/10.1021/cm502570b.
(23) Lee, S.; Hippalgaonkar, K.; Yang, F.; Hong, J.; Ko, C.; Suh, J.; Liu, K.; Wang, K.; Urban, J. J.; Zhang, X.; et al. Anomalously Low Electronic Thermal Conductivity in Metallic Vanadium Dioxide. *Science***2017**, *355* (6323), 371–374. https://doi.org/10.1126/science.aag0410.
(24) Alphabet Energy Materials Advantage. Alphebet Energy.
(25) Liu, W.; Yin, K.; Zhang, Q.; Uher, C.; Tang, X. Eco-Friendly High-Performance Silicide Thermoelectric Materials. *National Science Review***2017**, *4* (4), 611–626. https://doi.org/10.1093/nsr/nwx011.
(26) Stiewe, C.; Bertini, L.; Toprak, M.; Christensen, M.; Platzek, D.; Williams, S.; Gatti, C.; Müller, E.; Iversen, B. B.; Muhammed, M.; et al. Nanostructured Co1−xNix(Sb1−yTey)3 Skutterudites: Theoretical Modeling, Synthesis and Thermoelectric Properties. *Journal of Applied Physics***2005**, *97* (4), 044317. https://doi.org/10.1063/1.1852072.
(27) USGS Minerals Information: Mineral Commodity Summaries. USGS 2018.
(28) Critical raw materials https://ec.europa.eu/growth/sectors/raw-materials/specific-interest/critical_en.

(29) Endangered Elements https://www.acs.org/content/acs/en/greenchemistry/research-innovation/endangered-elements.html.
(30) Ouyang, Y.; Xie, Y.; Zhang, Z.; Peng, Q.; Chen, Y. New Record of High ZT Found in Hybrid Transition-Metal-Dichalcogenides. *arXiv:1612.05344 [cond-mat, physics:physics]* **2016**.
(31) Tewari, G. C.; Tripathi, T. S.; Rastogi, A. K. Thermoelectric Properties of Layer-Antiferromagnet CuCrS2. *Journal of Elec Materi* **2010**, *39* (8), 1133–1139. https://doi.org/10.1007/s11664-010-1185-5.
(32) Allen, P. B.; Feldman, J. L.; Fabian, J.; Wooten, F. Diffusons, Locons and Propagons: Character of Atomie Yibrations in Amorphous Si. *Philosophical Magazine B* **1999**, *79* (11–12), 1715–1731. https://doi.org/10.1080/13642819908223054.
(33) Tadano, T.; Gohda, Y.; Tsuneyuki, S. Anharmonic Force Constants Extracted from First-Principles Molecular Dynamics: Applications to Heat Transfer Simulations. *J. Phys.: Condens. Matter* **2014**, *26* (22), 225402. https://doi.org/10.1088/0953-8984/26/22/225402.
(34) Bardi, U. *Extracted: How the Quest for Mineral Wealth Is Plundering the Planet: A Report to the Club of Rome*; Chelsea Green Publishing: White River Junction, Vermont, 2014.
(35) Jain, A.; Shin, Y.; Persson, K. A. Computational Predictions of Energy Materials Using Density Functional Theory. *Nat Rev Mater* **2016**, *1* (1), 15004. https://doi.org/10.1038/natrevmats.2015.4.
(36) Barnes, W. L. Particle Plasmons: Why Shape Matters. *American Journal of Physics* **2016**, *84* (8), 593–601. https://doi.org/10.1119/1.4948402.
(37) Singh, M.; Goyal, M.; Devlal, K. Size and Shape Effects on the Band Gap of Semiconductor Compound Nanomaterials. *Journal of Taibah University for Science* **2018**, *12* (4), 470–475. https://doi.org/10.1080/16583655.2018.1473946.
(38) Giannozzi, P.; Baroni, S.; Bonini, N.; Calandra, M.; Car, R.; Cavazzoni, C.; Ceresoli, D.; Chiarotti, G. L.; Cococcioni, M.; Dabo, I.; et al. QUANTUM ESPRESSO: A Modular and Open-Source Software Project for Quantum Simulations of Materials. *J. Phys.: Condens. Matter* **2009**, *21* (39), 395502. https://doi.org/10.1088/0953-8984/21/39/395502.
(39) Mostofi, A. A.; Yates, J. R.; Lee, Y.-S.; Souza, I.; Vanderbilt, D.; Marzari, N. Wannier90: A Tool for Obtaining Maximally-Localised Wannier Functions. *Computer Physics Communications* **2008**, *178* (9), 685–699. https://doi.org/10.1016/j.cpc.2007.11.016.
(40) Setyawan, W.; Curtarolo, S. High-Throughput Electronic Band Structure Calculations: Challenges and Tools. *Computational Materials Science* **2010**, *49* (2), 299–312. https://doi.org/10.1016/j.commatsci.2010.05.010.
(41) Vogel, D.; Krüger, P.; Pollmann, J. Self-Interaction and Relaxation-Corrected Pseudopotentials for II-VI Semiconductors. *Phys. Rev. B* **1996**, *54* (8), 5495–5511. https://doi.org/10.1103/PhysRevB.54.5495.

(42) LaLonde, A. D.; Pei, Y.; Wang, H.; Jeffrey Snyder, G. Lead Telluride Alloy Thermoelectrics. *Materials Today***2011**, *14* (11), 526–532. https://doi.org/10.1016/S1369-7021(11)70278-4.
(43) Pizzi, G.; Volja, D.; Kozinsky, B.; Fornari, M.; Marzari, N. BoltzWann: A Code for the Evaluation of Thermoelectric and Electronic Transport Properties with a Maximally-Localized Wannier Functions Basis. *Computer Physics Communications***2014**, *185* (1), 422–429. https://doi.org/10.1016/j.cpc.2013.09.015.
(44) Rhyee, J.-S.; Kim, J. Chemical Potential Tuning and Enhancement of Thermoelectric Properties in Indium Selenides. *Materials***2015**, *8* (3), 1283–1324. https://doi.org/10.3390/ma8031283.
(45) *CRC Handbook of Thermoelectrics*; Rowe, D. M., Ed.; CRC Press: Boca Raton, FL, 1995.
(46) Fernández-García, M.; Rodriguez, J. A. Metal Oxide Nanoparticles. In *Encyclopedia of Inorganic and Bioinorganic Chemistry*; Scott, R. A., Ed.; John Wiley & Sons, Ltd: Chichester, UK, 2011; p eibc0331. https://doi.org/10.1002/9781119951438.eibc0331.
(47) *Handbook of Heterogeneous Catalysis*; Ertl, G., Knözinger, H., Weitkamp, J., Eds.; VCH: Weinheim, 1997.
(48) McDevitt, N. T.; Baun, W. L. Infrared Absorption Study of Metal Oxides in the Low Frequency Region (700-240 Cm−1). *Spectrochimica Acta***1964**, *20* (5), 799–808. https://doi.org/10.1016/0371-1951(64)80079-5.
(49) Sui, R.; Charpentier, P. Synthesis of Metal Oxide Nanostructures by Direct Sol–Gel Chemistry in Supercritical Fluids. *Chem. Rev.***2012**, *112* (6), 3057–3082. https://doi.org/10.1021/cr2000465.
(50) Walia, S.; Balendhran, S.; Nili, H.; Zhuiykov, S.; Rosengarten, G.; Wang, Q. H.; Bhaskaran, M.; Sriram, S.; Strano, M. S.; Kalantar-zadeh, K. Transition Metal Oxides – Thermoelectric Properties. *Progress in Materials Science***2013**, *58* (8), 1443–1489. https://doi.org/10.1016/j.pmatsci.2013.06.003.
(51) Zhang, Z.; Liu, J.; Gu, J.; Su, L.; Cheng, L. An Overview of Metal Oxide Materials as Electrocatalysts and Supports for Polymer Electrolyte Fuel Cells. *Energy Environ. Sci.***2014**, *7* (8), 2535–2558. https://doi.org/10.1039/C3EE43886D.
(52) Liu, Z.; Sui, X.; Kang, K.; Qin, S. Logarithmic Size-Dependent Melting Temperature of Nanoparticles. *J. Phys. Chem. C***2015**, *119* (21), 11929–11933. https://doi.org/10.1021/acs.jpcc.5b01188.
(53) Hench, L. L.; West, J. K. The Sol-Gel Process. *Chem. Rev.***1990**, *90* (1), 33–72. https://doi.org/10.1021/cr00099a003.
(54) Roy, R. Ceramics by the Solution-Sol-Gel Route. *Science***1987**, *238* (4834), 1664–1669. https://doi.org/10.1126/science.238.4834.1664.
(55) Baccile, N.; Babonneau, F.; Thomas, B.; Coradin, T. Introducing Ecodesign in Silica Sol–Gel Materials. *J. Mater. Chem.***2009**, *19* (45), 8537. https://doi.org/10.1039/b911123a.
(56) Niederberger, M. Nonaqueous Sol–Gel Routes to Metal Oxide Nanoparticles. *Acc. Chem. Res.***2007**, *40* (9), 793–800. https://doi.org/10.1021/ar600035e.

(57) Zha, J.; Roggendorf, H. Sol-Gel Science, the Physics and Chemistry of Sol-Gel Processing, Ed. by C. J. Brinker and G. W. Scherer, Academic Press, Boston 1990, Xiv, 908 Pp., Bound?ISBN 0-12-134970-5. *Adv. Mater.***1991**, *3* (10), 522–522. https://doi.org/10.1002/adma.19910031025.
(58) *The Sol-Gel Handbook: Synthesis, Characterization, and Applications*; Levy, D., Zayat, M., Eds.; Wiley-VCH: Weinheim, 2015.
(59) Arnal, P.; Corriu, R. J. P.; Leclercq, D.; Mutin, P. H.; Vioux, A. A Solution Chemistry Study of Nonhydrolytic Sol−Gel Routes to Titania. *Chem. Mater.***1997**, *9* (3), 694–698. https://doi.org/10.1021/cm960337t.
(60) Andrianainarivelo, M.; Corriu, R. J. P.; Leclercq, D.; Mutin, P. H.; Vioux, A. Non-Hydrolytic Sol–Gel Process: Zirconium Titanate Gels. *J. Mater. Chem.***1997**, *7* (2), 279–284. https://doi.org/10.1039/a605168e.
(61) Arnal, P.; Corriu, R. J. P.; Leclercq, D.; Mutin, P. H.; Vioux, A. Preparation of Transition Metal Oxides By A Nonhydrolytic Sol-Gel Process. *MRS Proc.***1994**, *346*, 339. https://doi.org/10.1557/PROC-346-339.
(62) Corriu, R. J. P.; Leclercq, D. Solution Chemistry for the Elaboration of Solids. *Comments on Inorganic Chemistry***1997**, *19* (4), 245–262. https://doi.org/10.1080/02603599708032739.
(63) Hay, J. N.; Raval, H. M. Preparation of Inorganic Oxides via a Non-Hydrolytic Sol-Gel Route. *Journal of Sol-Gel Science and Technology***1998**, *13* (1/3), 109–112. https://doi.org/10.1023/A:1008615708489.
(64) Stobbe, E. R.; de Boer, B. A.; Geus, J. W. The Reduction and Oxidation Behaviour of Manganese Oxides. *Catalysis Today***1999**, *47* (1–4), 161–167. https://doi.org/10.1016/S0920-5861(98)00296-X.
(65) Baldi, M.; Finocchio, E.; Milella, F.; Busca, G. Catalytic Combustion of C3 Hydrocarbons and Oxygenates over Mn3O4. *Applied Catalysis B: Environmental***1998**, *16* (1), 43–51. https://doi.org/10.1016/S0926-3373(97)00061-1.
(66) Sánchez, L.; Farcy, J.; Pereira-Ramos, J.-P.; Hernán, L.; Morales, J.; Tirado, J. L. Low-Temperature Mixed Spinel Oxides as Lithium Insertion Compounds. *J. Mater. Chem.***1996**, *6* (1), 37–39. https://doi.org/10.1039/JM9960600037.
(67) Thackeray, M. M.; David, W. I. F.; Bruce, P. G.; Goodenough, J. B. Lithium Insertion into Manganese Spinels. *Materials Research Bulletin***1983**, *18* (4), 461–472. https://doi.org/10.1016/0025-5408(83)90138-1.
(68) Chang, Y. Q.; Xu, X. Y.; Luo, X. H.; Chen, C. P.; Yu, D. P. Synthesis and Characterization of Mn3O4 Nanoparticles. *Journal of Crystal Growth***2004**, *264* (1–3), 232–236. https://doi.org/10.1016/j.jcrysgro.2003.11.117.
(69) Lei, S.; Tang, K.; Fang, Z.; Zheng, H. Ultrasonic-Assisted Synthesis of Colloidal Mn3O4 Nanoparticles at Normal Temperature and Pressure. *Crystal Growth & Design***2006**, *6* (8), 1757–1760. https://doi.org/10.1021/cg050402o.
(70) Vázquez-Olmos, A.; Redón, R.; Rodríguez-Gattorno, G.; Esther Mata-Zamora, M.; Morales-Leal, F.; Fernández-Osorio, A. L.; Saniger, J. M. One-Step Synthesis of

Mn3O4 Nanoparticles: Structural and Magnetic Study. *Journal of Colloid and Interface Science***2005**, *291* (1), 175–180. https://doi.org/10.1016/j.jcis.2005.05.005.
(71) Ozkaya, T.; Baykal, A.; Kavas, H.; Köseoğlu, Y.; Toprak, M. S. A Novel Synthetic Route to Mn3O4 Nanoparticles and Their Magnetic Evaluation. *Physica B: Condensed Matter***2008**, *403* (19–20), 3760–3764. https://doi.org/10.1016/j.physb.2008.07.002.
(72) Du, J.; Gao, Y.; Chai, L.; Zou, G.; Li, Y.; Qian, Y. Hausmannite Mn3O4 Nanorods: Synthesis, Characterization and Magnetic Properties. *Nanotechnology***2006**, *17* (19), 4923–4928. https://doi.org/10.1088/0957-4484/17/19/024.
(73) Ren, T.-Z.; Yuan, Z.-Y.; Hu, W.; Zou, X. Single Crystal Manganese Oxide Hexagonal Plates with Regulated Mesoporous Structures. *Microporous and Mesoporous Materials***2008**, *112* (1–3), 467–473. https://doi.org/10.1016/j.micromeso.2007.10.025.
(74) Thermogravimetric Analysis (TGA) A Beginner's Guide.
(75) Liu, X.; Cui, S.; Sun, Z.; Du, P. Copper Oxide Nanomaterials Synthesized from Simple Copper Salts as Active Catalysts for Electrocatalytic Water Oxidation. *Electrochimica Acta***2015**, *160*, 202–208. https://doi.org/10.1016/j.electacta.2015.01.123.
(76) Du, G. H.; Van Tendeloo, G. Cu(OH)2 Nanowires, CuO Nanowires and CuO Nanobelts. *Chemical Physics Letters***2004**, *393* (1–3), 64–69. https://doi.org/10.1016/j.cplett.2004.06.017.
(77) Huang, L. S.; Yang, S. G.; Li, T.; Gu, B. X.; Du, Y. W.; Lu, Y. N.; Shi, S. Z. Preparation of Large-Scale Cupric Oxide Nanowires by Thermal Evaporation Method. *Journal of Crystal Growth***2004**, *260* (1–2), 130–135. https://doi.org/10.1016/j.jcrysgro.2003.08.012.
(78) Mageshwari, K.; Sathyamoorthy, R. Flower-Shaped CuO Nanostructures: Synthesis, Characterization and Antimicrobial Activity. *Journal of Materials Science & Technology***2013**, *29* (10), 909–914. https://doi.org/10.1016/j.jmst.2013.04.020.
(79) Dubal, D. P.; Gund, G. S.; Lokhande, C. D.; Holze, R. CuO Cauliflowers for Supercapacitor Application: Novel Potentiodynamic Deposition. *Materials Research Bulletin***2013**, *48* (2), 923–928. https://doi.org/10.1016/j.materresbull.2012.11.081.
(80) Xiang, J. Y.; Tu, J. P.; Zhang, L.; Zhou, Y.; Wang, X. L.; Shi, S. J. Self-Assembled Synthesis of Hierarchical Nanostructured CuO with Various Morphologies and Their Application as Anodes for Lithium Ion Batteries. *Journal of Power Sources***2010**, *195* (1), 313–319. https://doi.org/10.1016/j.jpowsour.2009.07.022.
(81) Jisen, W.; Jinkai, Y.; Jinquan, S.; Ying, B. Synthesis of Copper Oxide Nanomaterials and the Growth Mechanism of Copper Oxide Nanorods. *Materials & Design***2004**, *25* (7), 625–629. https://doi.org/10.1016/j.matdes.2004.03.004.
(82) Cao, M.; Hu, C.; Wang, Y.; Guo, Y.; Guo, C.; Wang, E. A Controllable Synthetic Route to Cu, Cu2O, and CuO Nanotubes and NanorodsElectronic Supplementary Information (ESI) Available: EDS Patterns of Nanotubes and SEM Images of

Nanorods. See Http://Www.Rsc.Org/Suppdata/Cc/B3/B304505f/. *Chem. Commun.***2003**, No. 15, 1884. https://doi.org/10.1039/b304505f.
(83) Yao, W.-T.; Yu, S.-H.; Zhou, Y.; Jiang, J.; Wu, Q.-S.; Zhang, L.; Jiang, J. Formation of Uniform CuO Nanorods by Spontaneous Aggregation: Selective Synthesis of CuO, Cu_2O, and Cu Nanoparticles by a Solid−Liquid Phase Arc Discharge Process. *J. Phys. Chem. B***2005**, *109* (29), 14011–14016. https://doi.org/10.1021/jp0517605.
(84) Topnani, N.; Kushwaha, S.; Athar, T. Wet Synthesis of Copper Oxide Nanopowder. *International Journal of Green Nanotechnology: Materials Science & Engineering***2010**, *1* (2), M67–M73. https://doi.org/10.1080/19430840903430220.
(85) Kayani, Z. N.; Umer, M.; Riaz, S.; Naseem, S. Characterization of Copper Oxide Nanoparticles Fabricated by the Sol–Gel Method. *Journal of Elec Materi***2015**, *44* (10), 3704–3709. https://doi.org/10.1007/s11664-015-3867-5.
(86) Yin, M.; Wu, C.-K.; Lou, Y.; Burda, C.; Koberstein, J. T.; Zhu, Y.; O'Brien, S. Copper Oxide Nanocrystals. *J. Am. Chem. Soc.***2005**, *127* (26), 9506–9511. https://doi.org/10.1021/ja050006u.
(87) Ananth, A.; Dharaneedharan, S.; Heo, M.-S.; Mok, Y. S. Copper Oxide Nanomaterials: Synthesis, Characterization and Structure-Specific Antibacterial Performance. *Chemical Engineering Journal***2015**, *262*, 179–188. https://doi.org/10.1016/j.cej.2014.09.083.
(88) Henrist, C.; Mathieu, J.-P.; Vogels, C.; Rulmont, A.; Cloots, R. Morphological Study of Magnesium Hydroxide Nanoparticles Precipitated in Dilute Aqueous Solution. *Journal of Crystal Growth***2003**, *249* (1–2), 321–330. https://doi.org/10.1016/S0022-0248(02)02068-7.
(89) MacLagan, E. Constraints on Emplacement and Timing of the Steen River Impact Structure, Alberta, Canada. **2018**. https://doi.org/10.7939/R3M61C553.
(90) Ding, Y.; Zhang, G.; Wu, H.; Hai, B.; Wang, L.; Qian, Y. Nanoscale Magnesium Hydroxide and Magnesium Oxide Powders: Control over Size, Shape, and Structure via Hydrothermal Synthesis. *Chem. Mater.***2001**, *13* (2), 435–440. https://doi.org/10.1021/cm000607e.
(91) Utamapanya, S.; Klabunde, K. J.; Schlup, J. R. Nanoscale Metal Oxide Particles/Clusters as Chemical Reagents. Synthesis and Properties of Ultrahigh Surface Area Magnesium Hydroxide and Magnesium Oxide. *Chem. Mater.***1991**, *3* (1), 175–181. https://doi.org/10.1021/cm00013a036.
(92) Durin-France, A.; Ferry, L.; Lopez Cuesta, J.-M.; Crespy, A. Magnesium Hydroxide/Zinc Borate/Talc Compositions as Flame- retardants in EVA Copolymer. **2000**, *49*.
(93) Richards, R.; Mulukutla, R. S.; Mishakov, I.; Chesnokov, V.; Volodin, A.; Zaikovski, V.; Sun, N.; Klabunde, K. J. Nanocrystalline Ultra High Surface Area Magnesium Oxide as a Selective Base Catalyst. *Scripta Materialia***2001**, *44* (8–9), 1663–1666. https://doi.org/10.1016/S1359-6462(01)00877-6.

(94) Choudary, B. M.; Mulukutla, R. S.; Klabunde, K. J. Benzylation of Aromatic Compounds with Different Crystallites of MgO. *J. Am. Chem. Soc.***2003**, *125* (8), 2020–2021. https://doi.org/10.1021/ja0211757.
(95) Yu, J. C.; Xu, A.; Zhang, L.; Song, R.; Wu, L. Synthesis and Characterization of Porous Magnesium Hydroxide and Oxide Nanoplates. *J. Phys. Chem. B***2004**, *108* (1), 64–70. https://doi.org/10.1021/jp035340w.
(96) Li, Y.; Sui, M.; Ding, Y.; Zhang, G.; Zhuang, J.; Wang, C. Preparation of Mg(OH)2 Nanorods. **2000**.
(97) Lv, J.; Qiu, L.; Qu, B. Controlled Growth of Three Morphological Structures of Magnesium Hydroxide Nanoparticles by Wet Precipitation Method. *Journal of Crystal Growth***2004**, *267* (3–4), 676–684. https://doi.org/10.1016/j.jcrysgro.2004.04.034.
(98) An, D.; Wang, L.; Zheng, Y.; Guan, S.; Gao, X.; Tian, Y.; Zhang, H.; Wang, Z.; Liu, Y. In Situ Preparation and Surface Modification of Magnesium Hydroxide Nanoparticles. *Colloids and Surfaces A: Physicochemical and Engineering Aspects***2009**, *348* (1–3), 9–13. https://doi.org/10.1016/j.colsurfa.2009.06.004.
(99) Chen, D.; Zhu, L.; Zhang, H.; Xu, K.; Chen, M. Magnesium Hydroxide Nanoparticles with Controlled Morphologies via Wet Coprecipitation. *Materials Chemistry and Physics***2008**, *109* (2–3), 224–229. https://doi.org/10.1016/j.matchemphys.2007.11.014.
(100) Giorgi, R.; Bozzi, C.; Dei, L.; Gabbiani, C.; Ninham, B. W.; Baglioni, P. Nanoparticles of Mg(OH)2: Synthesis and Application to Paper Conservation. *Langmuir***2005**, *21* (18), 8495–8501. https://doi.org/10.1021/la050564m.
(101) Jaswal, V. S.; Arora, A. K.; Kinger, M.; Gupta, V. D.; Singh, J. Synthesis and Characterization of Chromium Oxide Nanoparticles. *Orient. J. Chem.***2014**, *30* (2), 559–566. https://doi.org/10.13005/ojc/300220.
(102) Rakesh; Ananda, S.; Gowda, N. M. M. Synthesis of Chromium(III) Oxide Nanoparticles by Electrochemical Method and Mukia Maderaspatana Plant Extract, Characterization, KMnO₄Decomposition and Antibacterial Study. *MRC***2013**, *02* (04), 127–135. https://doi.org/10.4236/mrc.2013.24018.
(103) Gibot, P.; Vidal, L. Original Synthesis of Chromium (III) Oxide Nanoparticles. *Journal of the European Ceramic Society***2010**, *30* (4), 911–915. https://doi.org/10.1016/j.jeurceramsoc.2009.09.019.
(104) El-Sheikh, S. M.; Mohamed, R. M.; Fouad, O. A. Synthesis and Structure Screening of Nanostructured Chromium Oxide Powders. *Journal of Alloys and Compounds***2009**, *482* (1–2), 302–307. https://doi.org/10.1016/j.jallcom.2009.04.011.
(105) Athar, T. Synthesis and Characterization of Strontium Oxide Nanoparticles via Wet Process. *mater focus***2013**, *2* (6), 450–453. https://doi.org/10.1166/mat.2013.1121.

(106) Stankic, S.; Bernardi, J.; Diwald, O.; Knözinger, E. Photoexcitation of Local Surface Structures on Strontium Oxide Grains. *J. Phys. Chem. C***2007**, *111* (22), 8069–8074. https://doi.org/10.1021/jp070538s.
(107) Nemade, K. R.; Waghuley, S. A. UV–VIS Spectroscopic Study of One Pot Synthesized Strontium Oxide Quantum Dots. *Results in Physics***2013**, *3*, 52–54. https://doi.org/10.1016/j.rinp.2013.03.001.
(108) Hedden, M.; Francis, N.; Haraldsen, J. T.; Ahmed, T.; Constantin, C. Thermoelectric Properties of Nano-Meso-Micro β-MnO2 Powders as a Function of Electrical Resistance. *Nanoscale Res Lett***2015**, *10* (1), 292. https://doi.org/10.1186/s11671-015-1000-6.
(109) Metselaar, R.; Van Tol, R. E. J.; Piercy, P. The Electrical Conductivity and Thermoelectric Power of Mn3O4 at High Temperatures. *Journal of Solid State Chemistry***1981**, *38* (3), 335–341. https://doi.org/10.1016/0022-4596(81)90064-5.

APPENDIX A

COMPUTATIONAL INPUT SCRIPTS FOR MANGANESE OXIDE

A.1: Manganese Dioxide Quantum ESPRESSO SCF Input

```
&CONTROL
  calculation = 'scf',
pseudo_dir = './pseudo',
restart_mode='from_scratch',
  prefix = 'MnO2_tetragonal_catalogNum_2105790',
wf_collect=.true.
  verbosity='high'
/
&SYSTEM
ibrav = 0,
nat = 6,
ntyp = 2,
ecutwfc = 100,
  occupations='smearing',
  smearing='gauss',
  degauss=0.10,
/
&ELECTRONS
conv_thr = 1.0e-6,
/
CELL_PARAMETERS angstrom
4.3983 0.0000 0.0000
0.0000 4.3983 0.0000
0.0000 0.0000 2.8730

ATOMIC_SPECIES
Mn   54.94   Mn.pbe-mt_fhi.UPF
O   16.0   O.pbe-kjpaw.UPF

ATOMIC_POSITIONS crystal
Mn 0.0 0.0 0.0
Mn 0.5 0.5 0.5
O 0.305149716936 0.305149716936 0.0
O 0.694850283064 0.694850283064 0.0
O 0.194850283064 0.805149716936 0.5
O 0.805149716936 0.194850283064 0.5
K_POINTS {automatic}
8 8 8 0 0 0
```

A.2: Manganese Dioxide Quantum ESPRESSO NSCF Input

```
&CONTROL
  calculation = 'nscf',
pseudo_dir = './pseudo',
restart_mode='from_scratch',
  prefix = 'MnO2_tetragonal_catalogNum_2105790',
wf_collect=.true.
/
&SYSTEM
ibrav = 0,
nat = 6,
ntyp = 2,
ecutwfc = 100,
nosym=.true.
  occupations='smearing',
  smearing='gauss',
  degauss=0.10,
/
&ELECTRONS
conv_thr = 1.0e-6,
/
&IONS
/
CELL_PARAMETERS angstrom
4.3983 0.0000 0.0000
0.0000 4.3983 0.0000
0.0000 0.0000 2.8730

ATOMIC_SPECIES
Mn   54.94   Mn.pbe-mt_fhi.UPF
O   16.0   O.pbe-kjpaw.UPF

ATOMIC_POSITIONS crystal
Mn 0.0 0.0 0.0
Mn 0.5 0.5 0.5
O 0.305149716936 0.305149716936 0.0
O 0.694850283064 0.694850283064 0.0
O 0.194850283064 0.805149716936 0.5
O 0.805149716936 0.194850283064 0.5

K_POINTS crystal
343
0.00000000  0.00000000  0.00000000  2.915452e-03
```

0.00000000 0.00000000 0.14285714 2.915452e-03
0.00000000 0.00000000 0.28571429 2.915452e-03
0.00000000 0.00000000 0.42857143 2.915452e-03
0.00000000 0.00000000 0.57142857 2.915452e-03
0.00000000 0.00000000 0.71428571 2.915452e-03
0.00000000 0.00000000 0.85714286 2.915452e-03
0.00000000 0.14285714 0.00000000 2.915452e-03
0.00000000 0.14285714 0.14285714 2.915452e-03
0.00000000 0.14285714 0.28571429 2.915452e-03
0.00000000 0.14285714 0.42857143 2.915452e-03
0.00000000 0.14285714 0.57142857 2.915452e-03
0.00000000 0.14285714 0.71428571 2.915452e-03
0.00000000 0.14285714 0.85714286 2.915452e-03
0.00000000 0.28571429 0.00000000 2.915452e-03
0.00000000 0.28571429 0.14285714 2.915452e-03
0.00000000 0.28571429 0.28571429 2.915452e-03
0.00000000 0.28571429 0.42857143 2.915452e-03
…

Truncated K-mesh for appendix, the complete mesh is much larger

A.3: Manganese Dioxide Wannier90 WIN Input

```
!!! -- Begin of BoltzWann input -- !!!
boltzwann                 = true
boltz_calc_also_dos       = true
boltz_dos_energy_step     = 0.01
smr_type                  = gauss
boltz_dos_adpt_smr        = false
boltz_dos_smr_fixed_en_width = 0.0167
kmesh                     = 40
boltz_mu_min              = 5.
boltz_mu_max              = 10.
boltz_mu_step             = 0.02
boltz_temp_min            = 300.
boltz_temp_max            = 700.
boltz_temp_step           = 5
boltz_relax_time          = 10.
!!! --- End of BoltzWann input --- !!!

#restart          = plot
#bands_plot       = true
#bands_plot_format = xmgr
wannier_plot = true

num_bands        = 23
num_wann         = 23
dis_win_max      = 18.35d0
dis_froz_max     = 15.35d0
dis_num_iter     = 120
dis_mix_ratio    = 1.d0
kmesh_tol        = 0.0001

num_iter         = 500
num_print_cycles  = 50

begin unit_cell_cart
4.3983 0.0000 0.0000
0.0000 4.3983 0.0000
0.0000 0.0000 2.8730
end unit_cell_cart

begin atoms_cart
Mn 0.0 0.0 0.0
Mn 0.5 0.5 0.5
```

O 0.305149716936 0.305149716936 0.0
O 0.694850283064 0.694850283064 0.0
O 0.194850283064 0.805149716936 0.5
O 0.805149716936 0.194850283064 0.5
End atoms_cart

begin projections
random
end projections

begin kpoint_path
G 0.0000 0.0000 0.0000 X 0.0000 0.5000 0.0000
X 0.0000 0.5000 0.0000 M 0.5000 0.5000 0.0000
M 0.5000 0.5000 0.0000 G 0.0000 0.0000 0.0000
G 0.0000 0.0000 0.0000 Z 0.0000 0.0000 0.5000
Z 0.0000 0.0000 0.5000 R 0.0000 0.5000 0.5000
R 0.0000 0.5000 0.5000 A 0.5000 0.5000 0.5000
A 0.5000 0.5000 0.5000 Z 0.0000 0.0000 0.5000
end kpoint_path

mp_grid = 7 7 7

begin kpoints
0.00000000 0.00000000 0.00000000
0.00000000 0.00000000 0.14285714
0.00000000 0.00000000 0.28571429
0.00000000 0.00000000 0.42857143
0.00000000 0.00000000 0.57142857
0.00000000 0.00000000 0.71428571
0.00000000 0.00000000 0.85714286
0.00000000 0.14285714 0.00000000
0.00000000 0.14285714 0.14285714
0.00000000 0.14285714 0.28571429
0.00000000 0.14285714 0.42857143
0.00000000 0.14285714 0.57142857
0.00000000 0.14285714 0.71428571
0.00000000 0.14285714 0.85714286
0.00000000 0.28571429 0.00000000
0.00000000 0.28571429 0.14285714
0.00000000 0.28571429 0.28571429
…

Truncated K-mesh for appendix, the complete mesh is much larger

A.4: Manganese Dioxide pw2wannier90 Input

```
&inputpp
outdir = './'
prefix = 'MnO2_tetragonal_catalogNum_2105790'
seedname = 'MnO2_tetragonal_catalogNum_2105790'
spin_component = 'none'
write_mmn = .true.
write_amn = .true.
write_unk = .false.
/
```

A.5 Manganese Dioxide Quantum ESPRESSO Band Input

```
&CONTROL
  calculation = 'bands',
pseudo_dir = './pseudo',
restart_mode='from_scratch',
  prefix = 'MnO2_tetragonal_catalogNum_2105790',
wf_collect=.true.
/

&SYSTEM
ibrav = 0,
nat = 6,
ntyp = 2,
ecutwfc = 100,
nosym=.true.
  occupations='smearing',
  smearing='gauss',
  degauss=0.10,
/

&ELECTRONS
conv_thr = 1.0e-6,
/
&IONS
/

CELL_PARAMETERS angstrom
4.3983 0.0000 0.0000
0.0000 4.3983 0.0000
0.0000 0.0000 2.8730

ATOMIC_SPECIES
Mn   54.94   Mn.pbe-mt_fhi.UPF
O   16.0   O.pbe-kjpaw.UPF

ATOMIC_POSITIONS crystal
Mn 0.0 0.0 0.0
Mn 0.5 0.5 0.5
O 0.305149716936 0.305149716936 0.0
O 0.694850283064 0.694850283064 0.0
O 0.194850283064 0.805149716936 0.5
O 0.805149716936 0.194850283064 0.5
```

```
K_POINTS crystal_b
7
0.0000 0.0000 0.0000 10
0.0000 0.5000 0.0000 10
0.5000 0.5000 0.0000 10
0.0000 0.0000 0.0000 10
0.0000 0.0000 0.5000 10
0.0000 0.5000 0.5000 10
0.5000 0.5000 0.5000 10
```

A.6 Manganese Dioxide Quantum ESPRESSO Bands Input

```
MnO2 bands input
&bands
prefix = 'MnO2_tetragonal_catalogNum_2105790'
outdir = './'
filband = 'MnO2_tetragonal_catalogNum_2105790.dat'
lsym=.true.
/
```